Understanding seismic properties of fault zones

Thesis submitted in accordance with the requirements of
the University of Liverpool for the degree of Doctor in Philosophy
by

Christina Monica Kelly

February 2014

Abstract

Fault zone properties at depth are often inferred from seismic properties such as seismic velocities and attenuation. An understanding of how fault zone properties and processes influence seismic measurements is required for successful interpretations to be made. As fault zones are heavily fractured and often fluid-rich areas, a knowledge of the influences of cracking and fluid content on seismic measurements is needed. This will allow better interpretation of fault zone properties and how they may change at the time of an earthquake.

Research presented in this thesis is concentrated on two regions of strike-slip faulting: the Parkfield area of the San Andreas fault and the exhumed Carboneras fault zone region of SE Spain. Well-preserved exhumed faults allow observation of fault structure at seismogenic depths. The structure of the exhumed Carboneras fault has previously been suggested as an analogue for the Parkfield area at depth.

Laboratory measurements can help us to determine what processes occur at seismogenic depths in active faults. They can also aid in interpretation of seismic studies. In this thesis laboratory and seismic studies are brought together in order to gain a greater understanding of fault zone seismic properties at depth and how to interpret them.

In order to characterise the properties of the Carboneras fault, laboratory experiments of velocities through fault gouge and fault zone rocks are performed. The influences of fracture damage and local geological fabric on velocities are investigated. Gouge velocities are measured to be less than those of the mica schist rock through which the fault cuts. Velocity changes due to variations in crack damage in cyclic loading experiments are less than 5% of the original rock velocity. Strong velocity anisotropy is observed in the mica schist, with velocities of the order of 30% less when measured perpendicular to the strong foliation present in the rock. The consequences in terms of seismically imaging the fault zone are discussed. The effects of this strong velocity anisotropy need to be considered for specific source-receiver geometries and the local geological fabric in the locations of seismic experiments.

Surface wave tomography and ambient noise analysis of the Carboneras fault zone region shows that faults are imaged as low velocity features at depth. Results suggest that velocities are reduced by approximately 10% at depths close to 3 km. The strong

anisotropy observed in laboratory experiments of mica schist may also have implications for seismic imaging of this region as this rock crops out widely. This is discussed in terms of a potentially strong crustal component to shear-wave splitting observations in the region.

In the second part of the thesis, temporal changes in seismic attenuation at the time of the 2004 M6.0 Parkfield earthquake are investigated. Seismic attenuation can give indications of fracture damage and healing. Spectral ratios between earthquakes within repeating clusters are calculated. A sharp increase in attenuation is observed immediately after the earthquake, which then decays over the next 2 years. The post-seismic decay is fit by a logarithmic function. The timescale of the decay is found to be similar to that in GPS data and ambient seismic noise velocities following the 2004 M6.0 Parkfield earthquake. The amplitude of the attenuation change corresponds to a decrease of approximately 10% in Q_P at the time of the earthquake. The greatest changes are recorded to the northeast of the fault trace, consistent with preferential damage in the extensional quadrant behind a north-westerly propagating rupture tip. Our analysis suggests that significant changes in seismic attenuation and hence fracture dilatancy during co-seismic rupture are limited to depths of less than about 5 km.

Contents

Acknowledgements

Chapter 1

Motivation and thesis structure

1.1 Motivation

Determination of the structural, mechanical and hydrological properties of fault zones is an important step towards understanding earthquake processes. How fault zone properties evolve temporally over an earthquake cycle is another key issue to understand. Methods of determining fault zone properties at depth include drilling, laboratory measurements, geophysical methods and field mapping of exhumed faults.

Recent and ongoing fault zone drilling projects include the San Andreas Fault Observatory at Depth (SAFOD), Taiwan Chelungpu Fault Drilling (TCDP), Gulf of Corinth Rift Laboratory (CRL) and the Deep Fault Drilling Project (DFDP) of the Alpine Fault, New Zealand. Such projects can help to constrain fault structure at depth. They also allow long-term in-situ monitoring of properties such as pore fluid pressure and state of stress within a fault zone. Furthermore, samples gained from drilling can be used in laboratory experiments to determine physical properties such as frictional strength and permeability of fault zone rocks. However, this type of project presents only a one-dimensional view of the fault from just one point of observation.

Field mapping can help to extend this information laterally. Mapping of exhumed faults allows investigation of fault zone structure at depth. However, for any particular fault, field mapping is constrained to the one slice through the fault, which is exposed at the surface today. Field mapping can also be affected by issues such as patchy exposure, weathering and overprinting of primary structures during exhumation. Laboratory analysis of samples from surface exposures of fault rocks may also be affected by these issues. In order to minimise these concerns, field studies have concentrated on recently exhumed traces of young but extinct fault zones that are exposed in arid climates (e.g. *Caine et al.* (1996); *Miller* (1996); *Foxford et al.* (1998); *Faulkner et al.* (2003)).

Geophysical methods can help to extend our understanding of fault properties into a more complete picture. Geophysical studies of fault zones include inversions of gravity or electromagnetic data, and seismic methods including velocity and attenuation tomography, guided wave studies and studies on precisely-relocated earthquakes.

Inversions of gravity or electromagnetic data are generally regional studies with a resolution on the order of a kilometre. Gravity data can give an indication of the volume of rock that has been fractured and damaged close to a fault (e.g. *Stierman* (1984); *Wang et al.* (1986)). Electromagnetic data can provide an image of variations in resistivity (or conductivity) that may be interpreted in terms of fluid pressures, presence of clay minerals and deposited conductive minerals, which can give indications of the presence of damaged fault zone rocks (e.g. *Eberhart-Philips and Michael* (1993); *Mackie et al.* (1997); *Unsworth et al.* (1999)).

Tomographic studies can image the area around a fault zone. Both velocity and attenuation tomography has been performed in fault zone regions (e.g. *Rietbrock* (2001); *Thurber et al.* (2006); *Bennington et al.* (2008)). Surface wave tomography from ambient noise may be implemented in areas of low natural seismicity (e.g. *Nicolson et al.* (2012)). Tomography may give indications of the extent of fracturing and damage and areas of high fluid pressure. However, resolution may not be good enough to image narrow structures such as faults. Also, body waves tend to avoid low velocity media and so may not sample along a fault structure. An improvement in the imaging resolution may be obtained by adding travel-time information of phases that spend much of their travel path along the fault zone structure. *Ben-Zion et al.* (1992) developed a joint travel-time tomography of body waves and fault zone head waves that propagate along material interfaces in the fault zone structure.

Another seismic method of investigating fault zone properties is modelling of fault zone guided waves. The region around a fault can act as a wave-guide (e.g. *Li and Leary* (1990); *Li et al.* (1994)). The properties of the waves trapped within a wave-guide (including amplitudes and frequency contents) are strongly dependent on the fault zone geometry and physical properties and may therefore reveal detailed information on fault structure (e.g. *Li and Vidale* (1996)). Fault zone trapped waves have been observed along several segments of the San Andreas fault (*Li et al.*, 1990, 1997b) and San Jacinto faults (*Li et al.*, 1997a) and in the rupture zones of the 1992 Landers, California (*Li et al.*, 1994) and 1995 Kobe, Japan earthquakes (*Li et al.*, 1998a).

Seismic methods can also help us to understand how the properties of a fault zone evolve over time. Temporal changes in seismic properties are often determined from clusters of repeating earthquakes. Such clusters can be determined from precise relocations of earthquakes (*Nadeau et al.*, 1994, 1995). Changes in velocity and attenuation have previously been reported from analysis of repeating earthquakes (e.g. *Schaff and Beroza* (2004); *Chun et al.* (2004); *Kelly et al.* (2013)). Such changes can be interpreted in terms of changes in crack density and fluid saturation.

Geophysical methods have varying degrees of resolution. There are often important trade-offs and uncertainties to consider with geophysical methods. When considering seismic studies, it is important to realise the various influences on the seismic proper-

ties in order for successful interpretations to be made. Fault zones are areas of intense fracturing and often inferred to be fluid-rich. Therefore, these are key aspects to understand.

This thesis focuses on understanding seismic properties of fault zones. The influences of cracking and fluid content on seismic properties are discussed in detail in Chapter 2. A range of studies are then presented, including laboratory investigations, ambient noise analysis and research on temporal changes in attenuation at the time of an earthquake.

1.2   Study areas: Parkfield, California and Carboneras, SE Spain

In this thesis, studies are concentrated on two fault zone areas: the Parkfield area of the San Andreas fault and the Carboneras fault zone region in SE Spain.

The Parkfield area of the San Andreas fault marks the transition between the creeping section of the fault to the North and the locked section to the South. Earthquakes of M6.0 have occurred on this segment of the fault in 1881, 1901, 1922, 1934, 1966 and most recently in 2004 (*Bakun and Lindh*, 1985; *Bakun et al.*, 2005). This area has been heavily instrumented since 1985 in anticipation of this most recent M6.0 earthquake, including instrumentation for the SAFOD project. Major aims of this extensive instrumentation have been to monitor temporal changes at the time of an earthquake and to look for precursory earthquake signals.

The Carboneras fault zone is a large left-lateral strike-slip fault in SE Spain. This fault has been exhumed from depths of $1.5-4$ km. It has been suggested to provide an analogue for the structure of the Parkfield area at depth, based on comparisons of field observations from the Carboneras region with seismic observations at Parkfield (*Faulkner et al.*, 2003).

Seismic observations in the Parkfield area suggest a fault zone width of approximately 2 km (*Thurber et al.*, 1997; *Michelini and McEvilly*, 1991; *Eberhart-Philips and Michael*, 1993), linking fault strands at depth (*Li et al.*, 1997b) and small bodies of high velocity material (*Michael and Eberhart-Philips*, 1991). Field observations from the Carboneras fault indicate a fault zone width of $1 - 1.5$ km, anastomosing strands of fault gouge within fractured protolith and bodies of dolomite containing localised fault planes (*Faulkner et al.*, 2003).

The studies presented from the Carboneras region form part of a larger project involved in determining the structure of the Carboneras fault zone and surrounding region from field mapping, laboratory experiments and seismic studies. As part of this larger project, a 24-station seismometer network, described in Chapter 5, was deployed for one year (Feb 2010-Feb 2011). As well as the ambient noise (Chapter 5) and laboratory studies (Chapter 4) presented in this thesis, this project has included analysis

of fault zone guided waves, receiver functions, local tomography, further laboratory investigations and field mapping. These studies have been carried out by a number of researchers from the University of Liverpool, University of Manchester and GFZ Potsdam.

1.3 Thesis structure

This thesis consists of an introductory literature review followed by two main sections in which the research carried out is presented. The introductory literature review discusses the influences of fractures and fluids on seismic properties. These are key issues to understand in terms of the seismic properties of fault zones. The application of these concepts to fault zone settings is also considered within this chapter.

Section one focuses on the long-term (static) seismic properties of fault zones and includes studies from the Carboneras fault zone region. The geological history of the Internal Betics of SE Spain is introduced in Chapter 3. Faulting and current-day seismicity in the region is also discussed. Laboratory measurements of velocities through fault gouge and fault zone rocks are presented in Chapter 4. The influences of cracking and geological fabric on seismic properties of this fault zone are considered. The results are discussed in terms of the consequences for other ongoing seismic studies in the region. In Chapter 5 a surface wave tomography study of the Carboneras fault zone region using ambient noise is presented. Results are discussed in terms of faulting in the region.

Section two focuses on temporal changes in fault zones and research from the Parkfield area of the San Andreas fault is presented. In Chapter 6, changes in cracking and fluid flow at the time of an earthquake are discussed, along with the effects on seismic properties. A study of temporal changes in seismic attenuation at the time of the most recent (2004) M6.0 earthquake in Parkfield is presented in Chapter 7.

Finally, overall conclusions are discussed along with potential areas for further research. References for all chapters are consolidated at the end of the thesis.

Chapter 2

Influences on seismic properties in fault zones: fractures and fluids

In order to interpret seismic studies accurately, an understanding of the influences on seismic properties must be developed. Fault zones are heavily fractured and often fluid-rich. Therefore, when considering seismic studies of fault zone areas, the influences of cracking and fluid content are key aspects to understand. Knowledge of how these parameters affect seismic properties will in turn allow us to use seismic studies in order to determine better the fracturing and fluid content of fault zones. Observations that contribute significantly to our understanding of the influences of cracking and fluid content on seismic velocity and attenuation are discussed below.

2.1 Seismic velocity

P wave velocity is given by

$$V_P = \sqrt{\frac{K + \frac{4}{3}G}{\rho}} = \sqrt{\frac{\lambda + 2G}{\rho}} \tag{2.1}$$

and S wave velocity is given by

$$V_S = \sqrt{\frac{G}{\rho}} \tag{2.2}$$

where K is the bulk modulus and G is the shear modulus. λ and μ are the Lamé parameters ($K = \lambda + \frac{2}{3}G$), which together with the density ρ specify completely the elastic parameters of a linear isotropic solid . The bulk and shear moduli describe the response of a material to uniform pressure and shear strain respectively. When cracks and/or fluids are introduced into a medium the effect is to alter these moduli as well as the effective density of the medium, which in turn will change the P and S wave velocities.
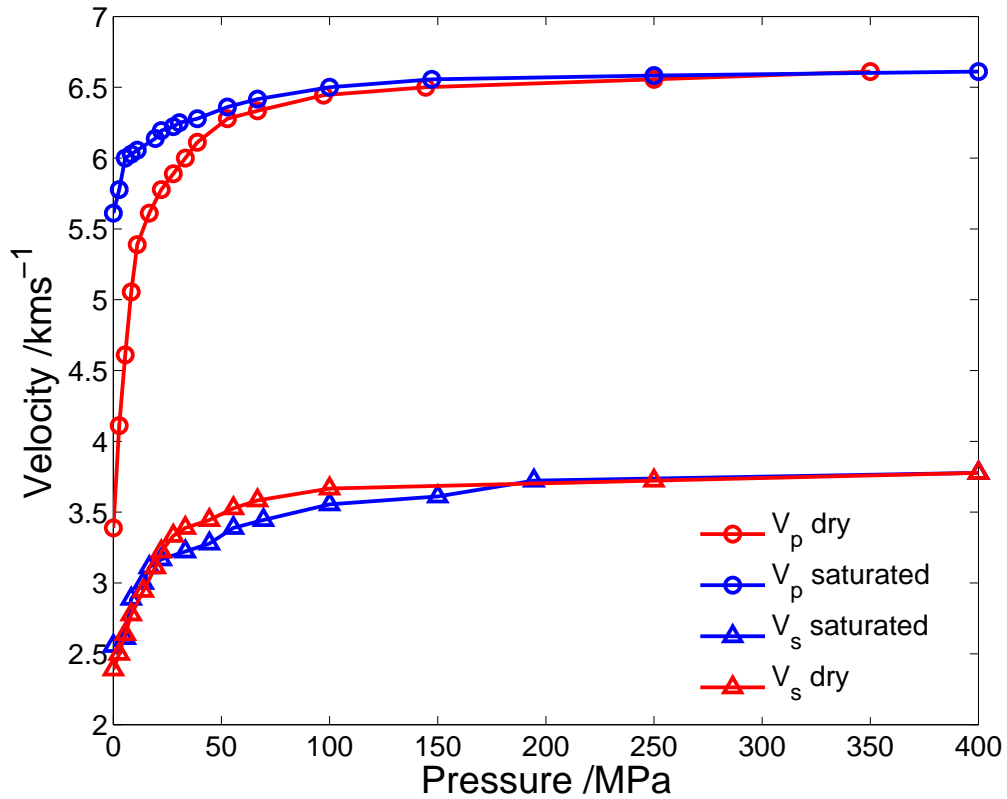
Figure 2.1: The influence of confining pressure on P and S velocities for dry (red) and saturated (blue) granite. Increased pressure results in crack closure, which increases the wave velocity. Saturation significantly alters the P wave velocity at low pressures, but has little effect on the S wave velocity. Data are laboratory-measured velocities through granite by *Nur and Simmons* (1969).

2.1.1 Velocity variations due to cracks

A measurable reduction in velocity of a medium due to the presence of cracks and fractures is expected theoretically (*O'Connell and Budiansky*, 1974) and observed in laboratory (e.g. *Birch* (1960, 1961); *Kitamura et al.* (2010)) and field experiments (e.g. *Moos and Zoback* (1983)).

In laboratory experiments, both P wave (*Birch*, 1960) and S wave (*Birch and Bancroft*, 1938) velocities are observed to increase significantly with increasing pressure (see figure 2.1). At low confining pressures, relatively large changes of velocity are observed. This is interpreted as closure and collapse of cracks and pores. At higher pressures, the elastic wave velocities increase more slowly. At these pressures, the changes are interpreted as being due to intrinsic effects of the rock i.e. to the compressibility of its constituent materials (e.g. *Birch* (1960); *Kern* (1978, 1990); *Adams and Williamson* (1923)). Such changes in the elastic properties of rocks with increasing pressure have long been noted (*Adams and Williamson*, 1923). *Birch* (1960, 1961) presents mea-
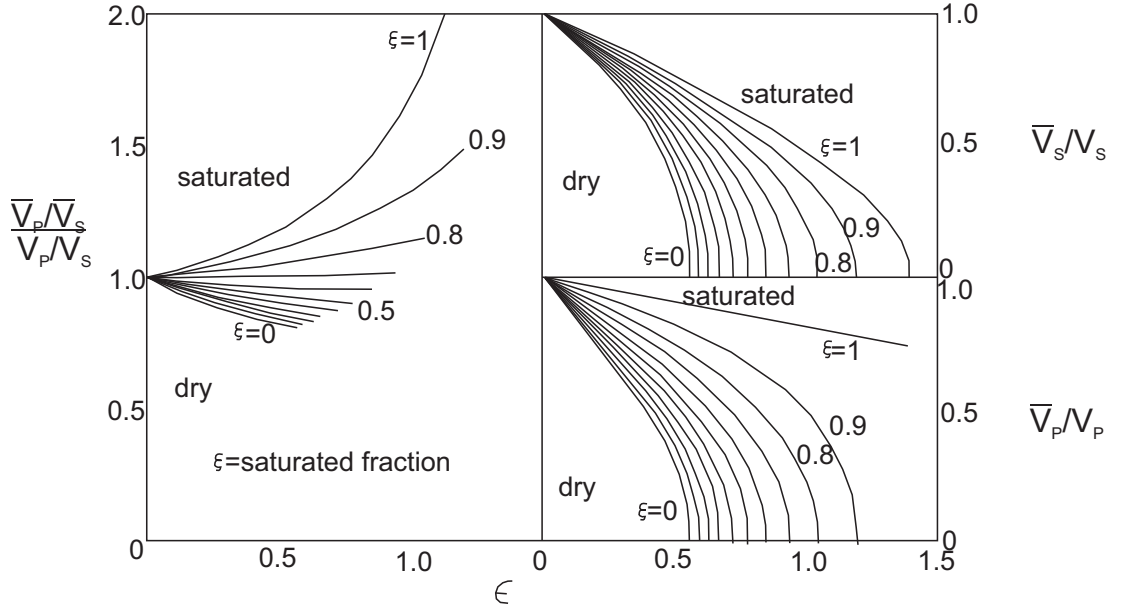
Figure 2.2: Changes in V_P, V_S and V_P/V_S according to the model of *O'Connell and Budiansky* (1974) due to the introduction of cracks for a range of saturation fractions ξ and crack density parameters ϵ. Introduction of dry or saturated cracks lowers both V_P and V_S. Introduction of dry cracks lowers V_P/V_S, but introduction of saturated cracks increases V_P/V_S. Figure redrawn from *O'Connell and Budiansky* (1974).

surements of compressional wave velocities for a large number of rocks that exhibit these effects, and discusses the influences of cracks and porosity.

In field experiments, larger changes in velocity may be observed than are expected from laboratory experiments due to an extra signal from macroscopic fractures, which are not normally sampled in laboratory experiments (*Moos and Zoback*, 1983; *Stierman and Kovach*, 1979). As well as a reduction in velocity due to the macro-fractures themselves, chemical alteration of the rock and an increased level of micro-fracturing may occur in the vicinity of macro-fractures, and these conditions may also contribute to reductions in the P and S wave velocity to some degree.

O'Connell and Budiansky (1974) modelled the effects of cracks on elastic properties by calculating the energy of individual cracks. According to the model, the changes in V_P, V_S and V_P/V_S are given by:

$$\frac{\bar{V}_s}{V_s} = \left(\frac{\bar{G}}{G} \right)^{1/2} \tag{2.3}$$

$$\frac{\bar{V}_p}{V_p} = \left(\frac{(1-\bar{\nu})(1+\nu)\bar{K}}{(1+\bar{\nu})(1-\nu)K} \right)^{1/2} \tag{2.4}$$

$$\frac{\bar{V}_p/\bar{V}_s}{V_p/V_s} = \left(\frac{(1-\bar{\nu})(1-2\nu)}{(1-2\nu)(1-\nu)} \right)^{1/2} \tag{2.5}$$

7

where, for dry circular cracks the change in moduli are given by:

$$\frac{\bar{K}}{K} = 1 - \frac{16}{9} \left(\frac{1 - \nu^2}{1 - 2\nu} \right) \epsilon \qquad (2.6)$$

and

$$\frac{\bar{G}}{G} = 1 - \frac{32}{45} \left(\frac{(1 - \bar{\nu})(5 - \nu)}{2 - \bar{\nu}} \right) \epsilon \qquad (2.7)$$

where ν is the Poisson's ratio, ϵ is the crack density parameter and a bar over a symbol represents that it is an effective property of the cracked material rather than the uncracked material. For circular cracks, ϵ is given by $\epsilon = Na^3$, where N is the number of cracks per unit volume and a is the crack radius. The effective Poisson ratio $\bar{\nu}$ is related to the crack density parameter ϵ by

$$\bar{\nu} = \nu(1 - \frac{16}{9}\epsilon) \qquad (2.8)$$

Results for elliptical cracks are essentially the same as for circular cracks, as long as the crack density is characterised by $\epsilon = 2NA^2/P\pi$, where A is the area of cracks and P is the perimeter of cracks (*O'Connell and Budiansky*, 1974). This model predicts that the introduction of dry cracks into a medium will cause a decrease in both P and S wave velocities (see figure 2.2). However, the P wave velocity initially decreases about 40% more rapidly than the S wave velocity. Therefore, a decrease in V_P/V_S is also observed when dry cracks are introduced into a medium (see figure 2.2). The effect of dry and saturated cracks (discussed below) on V_P, V_S and V_P/V_S according to this model are summarised in figure 2.2. *O'Connell and Budiansky* (1974) compare predictions of this theory with the laboratory data of *Nur and Simmons* (1969), with generally good agreement.

Shear Wave Splitting

In fault zones there may be a preferred fracture orientation related to the stress field. If there is a preferred fracture orientation within a material, then it will be anisotropic and variations in the wave velocity with direction of propagation will be observed. Waves travelling perpendicular to fractures will travel slower than those travelling parallel to the fractures (*Crampin*, 1978, 1984a,b; *Hudson*, 1981). If a shear wave is incident at an angle to an anisotropic fabric, then it will split into two shear waves, travelling in perpendicular fast and slow polarisations (see figure 2.3). The orientations of the polarisations provide information about the anisotropic symmetry and the stress direction. The time-delays between the split shear waves provide information about the average crack density along the raypaths. There is, however, a trade-off between the thickness of an anisotropic layer and the degree of anisotropy e.g. a thin, heavily anisotropic layer may produce the same time delay as a thicker, less anisotropic layer. Anisotropy and subsequent shear wave splitting may also be caused by crystal alignments, lithological alignments and regular layers (e.g. strata).

8
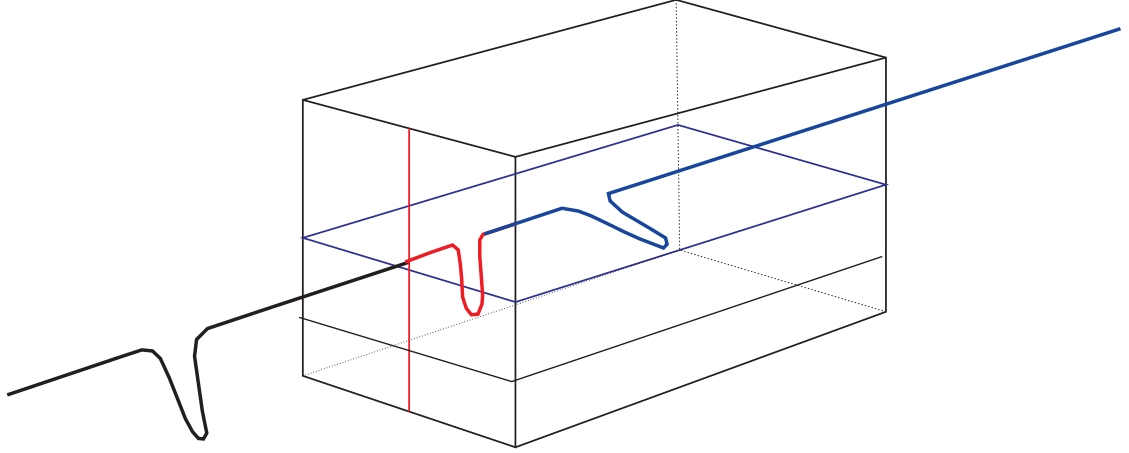
Figure 2.3: Schematic diagram illustrating the phenomenon of shear wave splitting. If a shear wave is incident on an anisotropic fabric then it will split into two shear waves travelling with perpendicular fast (blue) and slow (red) polarisations.

2.1.2 Velocity variations due to fluids

The presence of pore fluids in permeable rocks is common in the earth. It is therefore an important environmental factor to be considered in in-situ seismic investigations. Observations from field and laboratory experiments show that the presence of pore fluids has a strong effect on the velocities at which elastic waves will propagate.

For a rock with porosity ϕ saturated with a fluid of density ρ_f and bulk modulus K_f (shear modulus is zero for a fluid), *Wyllie et al.* (1956) approximated the travel time of a wave as the volume-weighted average of travel times through a layer of solid rock and a layer of pore fluid. This leads to the Wyllie time-average:

$$\frac{1}{V_P} = \frac{\phi}{V_{Pf}} + \frac{1-\phi}{V_{Pm}} \qquad (2.9)$$

where V_{Pf} and V_{Pm} are the P-wave velocities through the fluid and rock matrix respectively and V_P is the approximation to the P-wave velocity through the fluid-saturated rock. From equation 2.1, $V_{Pf} = \sqrt{(\frac{K_f}{\rho_f})}$ and $V_{Pm} = \sqrt{\frac{K+\frac{4}{3}G}{\rho}}$. This model, however, usually underestimates wave speeds.

A more sophisticated way of addressing this is to consider effective moduli of a fluid-saturated rock. Addition of pore fluid will not increase the shear stiffness, but the effective bulk modulus (K_{eff}) will change as described by the Gassmann equation:

$$K_{eff} = \frac{\phi(\frac{1}{K_f} - \frac{1}{K_m}) + (\frac{1}{K_d} - \frac{1}{K_m})}{\phi\frac{(\frac{1}{K_f} - \frac{1}{K_m})}{K_d} + \frac{(\frac{1}{K_d} - \frac{1}{K_m})}{K_m}} \qquad (2.10)$$

where K_m is the bulk modulus of the matrix and K_d is the effective bulk modulus under drained (dry) conditions. The effective density is the volume weighted average

of the matrix and fluid densities i.e.

$$\rho_{eff} = (1 - \phi)\rho_m + \phi\rho_f. \tag{2.11}$$

The wave speeds through the fluid-saturated rock are then given by

$$V_P = \sqrt{\frac{(K_{eff} + \frac{4}{3}G_{eff})}{\rho_{eff}}} \tag{2.12}$$

and

$$V_S = \sqrt{\frac{G_{eff}}{\rho_{eff}}} \tag{2.13}$$

where the effective shear modulus, G_{eff}, will be equal to the effective modulus under drained (dry) conditions (G_d). Saturating the pore fluid space with fluid will increase the density and leave the shear modulus unchanged, resulting in slightly lower shear wave velocity. The increase in bulk modulus with saturation usually has a much greater effect than the increase in density (equation 2.12). Therefore V_P increases when a rock becomes saturated. According to the calculations of *O'Connell and Budiansky* (1974), as described above, saturating previously dry cracks results in an increase in V_S, in contrast to the calculations above. However, in both cases the change in V_S is small relative to the increase in V_P, and therefore an increase in V_P/V_S is observed. The effect of different crack densities and different saturation levels on V_P and V_S from the calculations of *O'Connell and Budiansky* (1974), as described in the previous section, are summarised in figure 2.2.

As with the introduction of dry cracks into a medium, saturated cracks will decrease the seismic wave velocities (compared to an uncracked medium). However, with the introduction of saturated cracks, the V_P/V_S ratio will increase, in contrast to the introduction of dry cracks when the V_P/V_S ratio decreases (*O'Connell and Budiansky*, 1974). Saturating previously dry cracks or pores (i.e. at zero pore pressure) will increase the P wave velocity at ambient pressure (*Nur and Simmons*, 1969). The effect of this is to diminish the change in P wave velocity with changing confining pressure or crack density (see figure 2.1). Saturation has little effect, however, on the shear wave velocity. Therefore, at low pressures V_P/V_S will increase when previously dry cracks are saturated.

If at constant confining pressure a pore fluid pressure is induced, the effect may instead be to decrease the seismic velocities. It has been shown theoretically that seismic velocities in fluid-saturated solids are a function of the effective pressure,

$$P_{eff} = P_c - nP_p, \tag{2.14}$$

where P_{eff} is the effective pressure, P_c is confining pressure, P_p is pore pressure and in general, $n \leq 1$. (*Brandt*, 1955; *Biot*, 1956a,b; *Christensen*, 1984). By considering bulk

10

volumetric strain, it has been shown that $n = (1 - \frac{K}{K_i})$, where K is the bulk modulus of the porous solid and K_i is the intrinsic bulk modulus (*Skempton*, 1961). However, alternative values of n are found when considering elastic properties other than the bulk volumetric strain (*Robin*, 1973). For example, by considering the variation in pore volume, $n = (1 - \frac{\rho K}{(K_i - K)})$. It is noted that when $K << K_i$ both forms reduce to $n \approx 1$. If the pore pressure is kept equal to the confining pressure (i.e. low effective pressure), then only slight changes in velocity will be observed over a range of confining pressures (*Adams and Williamson*, 1923). The configuration of pores and cracks in this case remain effectively unchanged from the initial unstressed condition.

The properties of the particular pore fluid are also observed to affect the measured elastic wave velocities. *Kitamura et al.* (2006) compare velocities measured in dry conditions with those when water and argon gas act as pore fluids. For the same effective pressure the highest velocities are seen in dry conditions and the lowest velocities when argon gas is used as the pore fluid. A decrease in wave velocity with increasing temperature is also observed. Variation of seismic velocities with pore fluid viscosity has been investigated experimentally (*Nur and Simmons*, 1969; *Nur*, 1971; *Khalatbari et al.*, 1991). Both P wave and S wave velocities increase significantly with increasing viscosity. The relative change of the S wave velocity with viscosity is much larger than the relative change in the P wave velocity. These observations are in agreement with theory by *Walsh* (1969).

2.2   Seismic Attenuation

Attenuation is a measure of energy loss in a medium. The degree of attenuation will therefore affect the amplitude and shape of a waveform. The energy in an attenuated wave can be defined as:

$$b(x) = b_0 exp^{-\alpha x} \tag{2.15}$$

where b_0 is the energy at distance $x = 0$, b is the energy at distance x, and α is the attenuation coefficient (the inverse of the distance over which the amplitude will decay by $1/e \approx 0.37$). α along with the inverse of the quality factor Q and the logarithmic decrement δ are common measures of attenuation, and are related to each other and the energy loss in the system via:

$$\frac{1}{Q} = \frac{\Delta E}{2\pi E} = \frac{2\alpha\lambda}{2\pi} = \frac{2\alpha c}{\omega} = \frac{\delta}{\pi} \tag{2.16}$$

where ΔE is the energy loss per cycle, E as the peak energy, ω is the angular frequency, c is the wave velocity and λ is the wavelength, with $\lambda = 2\pi c/\omega$ (e.g. *Knopoff and MacDonald* (1958)). Although these measures contain the same information, α essentially measures the energy loss per distance travelled by the wave, whereas Q^{-1} and δ measure the energy loss per wave cycle. We choose to discuss attenuation in

terms of Q and Q^{-1}. Highly attenuating material results in a rapid loss of energy and will have a low quality factor. Conversely, a material with a high quality factor will allow a wave to travel for longer, or retain more of its energy. Typically, Q values are in the range of 10-100 for porous rocks such as sandstones and limestones and 100-1000 for igneous and metamorphic rocks (*Bradley and Fort*, 1966).

Seismic wave attenuation consists of intrinsic attenuation (i.e. absorption of energy through conversion to heat) and extrinsic attenuation (energy loss due to geometric spreading, scattering and reflection). Both intrinsic and extrinsic attenuation will cause amplitude reduction, but intrinsic attenuation also causes pulse broadening and phase delay (*Zhang and Ulrych*, 2002). Extrinsic attenuation is affected by layering and heterogeneities in a medium, which cause energy loss due to reflection and scattering respectively (*O'Doherty and Anstay*, 1971; *Sato and Fehler*, 1998). Intrinsic attenuation is affected by properties such as permeability, porosity and fluid content of a medium. The energy is irreversibly converted to heat. Potential mechanisms for this kind of attenuation include frictional movement and fluid flow which are discussed in more detail below. It is usually assumed that the attenuation arising from different mechanisms, as quantified by Q^{-1}, is additive.

Q and Q^{-1} can be measured using either time-domain (e.g. rise time) or frequency domain (e.g. spectral ratios) methods. Over large frequency ranges Q may be frequency dependent. However, in the seismic frequency range $(10-200 \text{ Hz})$ Q is assumed to be frequency independent (e.g. *Adams and Abercrombie* (1998); *Rietbrock* (2001)). The presence of cracks and fluids are known to have a strong effect on attenuation. The influence of each is discussed below, with reference to potential mechanisms.

2.2.1 Attenuation variations due to cracks

Attenuation is observed to decrease (Q increases) with increasing confining pressure for both P and S waves (e.g. *Gardner et al.* (1964); *Gordon and Davis* (1968); *Toksöz et al.* (1979)). The rate of decrease is high at low pressures and levels off at higher pressures (see figure 2.4). Also, attenuation values in individual crystals are generally much lower than in a rock (*Peselnick and Zietz*, 1959). These observations are usually interpreted as a decrease in attenuation (increase in Q) when cracks close.

Inhomogeneities such as cracks and pores can influence scattering, a mechanism for extrinsic attenuation. When an elastic wave impinges on an inhomogeneity, some of the energy is scattered in directions other than the propagation direction of the wave, decreasing its amplitude (*Sato and Fehler*, 1998). *Yamakawa* (1962) calculated the scattering from isolated spherical pores of radius a and found that

$$Q^{-1} = g\phi(\omega a/c)^3 \tag{2.17}$$

where ϕ is the porosity, c is the wave velocity and g is a dimensionless parameter of order 1 whose precise value depends on the moduli and densities of the rock and pore
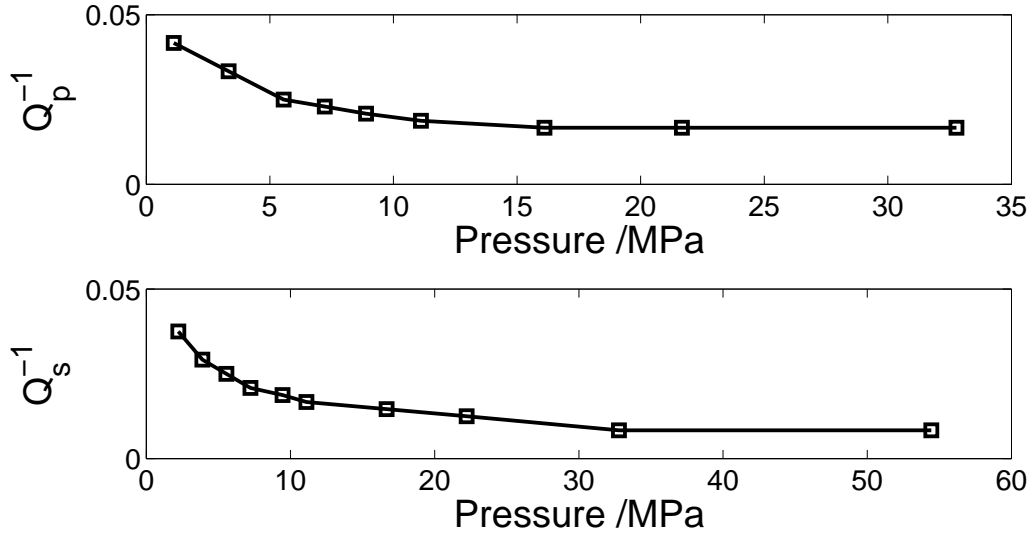
Figure 2.4: Increasing confining pressure causes a decrease in both P and S wave attenuation as cracks close. Data shown are laboratory measurements through sandstone by *Spencer* (1979).

fluid. Other pore shapes lead to the same general form, but with different values of g and with a being the characteristic dimension (e.g. crack length). Scattering effects due to pores will only be important at ultrasonic frequencies. Large fractures may cause scattering effects at seismic frequencies (*Taira et al.*, 2008). Scattering may also occur off large clusters of small cracks.

Frictional dissipation due to relative motions at grain boundaries and across crack surfaces, may be an important mechanism for intrinsic attenuation related to cracks (*Johnston et al.*, 1979; *Toksöz et al.*, 1979). *Walsh* (1966) formulated the problem by approximating the cracks as ellipsoids in plane strain. For a random orientation of cracks, the Q values for compressional and shear waves were computed using the friction coefficient μ, effective Poisson's ratio $\bar{\nu}$ and rock moduli as parameters. The resulting expressions for P and S-waves in an infinite medium have the following form:

$$Q_p^{-1} = \frac{\bar{E}(1-\bar{\nu})l^3 N F(\mu, \bar{\nu})}{E(1-2\bar{\nu})V_0} \tag{2.18}$$

and

$$Q_S^{-1} = \frac{\bar{E}l^3 N F(\mu)}{E(1-2\bar{\nu})V_0} \tag{2.19}$$

where $\bar{E}$ and E are the effective and matrix Young's moduli respectively, N is the number of cracks with a half-length l in a volume V_0 and $F(\mu)$ and $F(\mu, \bar{(\nu)})$ are functions of μ and $\bar{(\nu)}$. Only cracks of certain orientations, determined by μ and $\bar{\nu}$ will contribute to the attenuation. There will be no frictional sliding along faces of open cracks, and the small stresses associated with seismic waves will be insufficient to cause

13

sliding on crack faces that are tightly closed. *Savage* (1969) argued that there are unlikely to be a sufficient number of barely closed cracks to yield appreciable values of Q^{-1}. *Mavko* (1979) considered a tapered crack, a portion of whose two faces will always be in contact, and for typical parameter values found $Q^{-1} \approx \epsilon/a$ where ϵ is the incremental strain associated with the wave and a is some appropriate mean value of the initial crack aspect ratio.

In the same way as an anisotropic material may cause variations in the wave velocity with propagation direction, such anisotropy might also be observed in attenuation measurements. Waves travelling in different propagation directions through a material with a preferred fracture orientation may experience different amounts of attenuation (*Crampin*, 1981; *Liu et al.*, 2005). Q is found to be more sensitive to crack parameters than the wave velocity (e.g. *Xu and King* (1990)). *Crampin* (1981) shows that aligned cracks induce a much greater anisotropy in wave attenuation than in velocity. This implies that wave attenuation is much more sensitive to stress-induced cracks than velocity is. Attenuation due to friction on thin cracks and grain boundaries is thought to be the dominant mechanism for attenuation in the Earth's crust.

2.2.2 Attenuation variations due to fluids

Pore fluids are observed experimentally to have a very strong effect on attenuation in rocks (e.g. *Winkler and Nur* (1982); *Toksöz et al.* (1979)). At low degrees of saturation, P wave attenuation increases significantly with saturation. However, at between 60 and 90% saturation P wave attenuation reaches a maximum (see figure 2.5). As saturation increases beyond this point, P wave attenuation decreases (see figure 2.5). P wave attenuation is observed to be greater at full saturation than in dry conditions (*Toksöz et al.*, 1979). Shear wave attenuation also increases significantly with degree of saturation, but continues to increase until complete saturation (see figure 2.5). At full saturation, shear wave attenuation is greater than P wave attenuation (*Toksöz et al.*, 1979; *Spencer*, 1979; *Winkler and Nur*, 1982).

The ratio of Q_P/Q_S is sensitive to the degree of saturation. $Q_p/Q_s < 1$ indicates partial saturation or dry conditions, while $Q_p/Q_s > 1$ indicates complete or near-complete saturation (*Winkler and Nur*, 1982). Higher confining pressure will reduce the effect of fluid saturation, as the permeability will decrease due to crack closure (*Gardner et al.*, 1964). As with changes in seismic velocity, it is the effective pressure that is important (see equation 2.11). This must be taken into account if pore fluids are present under pore fluid pressure.

The properties of the saturating fluid will also have an effect. For example, *Toksöz et al.* (1979) found that a greater reduction in Q was observed with a rock saturated with brine than saturated with methane, with the dry rock as a reference. The effect of pore fluid viscosity on seismic attenuation has been investigated experimentally (*Nur and*
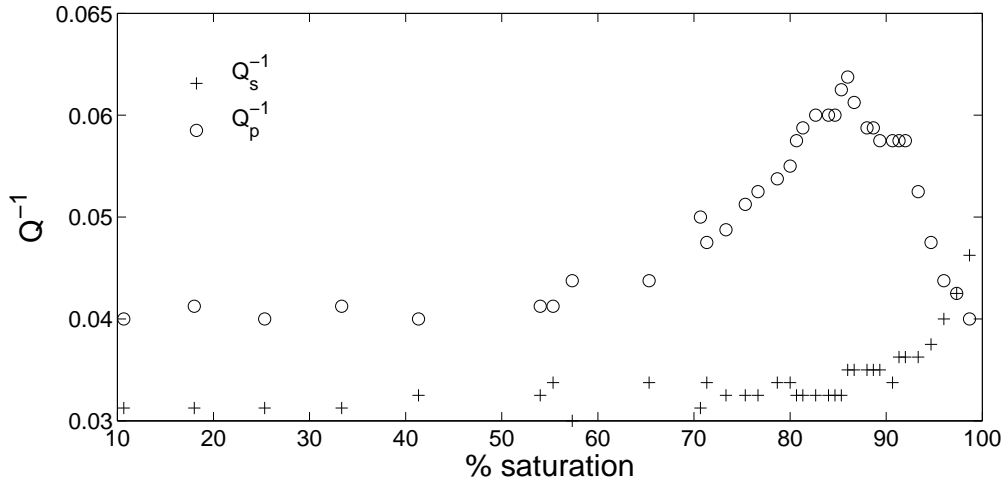
Figure 2.5: The effect of saturation level on P and S wave attenuation is shown. Increasing saturation causes an increase in S wave attenuation, until a maximum attenuation is reached at full saturation. For P waves, attenuation first increases with increased saturation. P wave attenuation then reaches a maximum level, and begins to decrease as it approaches full saturation. Data by *Murphy* (1982) using Massilon sandstone.

Simmons, 1969; *Nur*, 1971). Results show a broad peak in P and S wave attenuation at medium pore fluid viscosities. The effect on S wave attenuation is greater than the effect on P wave attenuation.

Many authors have discussed potential mechanisms to explain these patterns in attenuation with saturation level. Mechanisms through which the level of fluid saturation may contribute to attenuation include frictional changes due to wetting on grain boundaries (*Winkler and Nur*, 1979; *Johnston et al.*, 1979), and fluid flow mechanisms (e.g. *Mavko and Nur* (1975); *O'Connell and Budiansky* (1977), see figure 2.6). Adding a small amount of water to a rock will wet the internal surfaces. This may lubricate these surfaces and enhance frictional sliding (*Winkler and Nur*, 1979). Addition of more water may have slight further effects on the frictional energy loss, but will also enhance energy losses due to fluid flow. Fluid flow may be within or between cracks (*Mavko and Nur*, 1975), or between areas with different levels of saturation (e.g. *White* (1975)). Fluid flow may, for example, be induced between two adjacent, connected cracks due to the volume change caused by the stress wave (*Mavko and Nur*, 1975; *O'Connell and Budiansky*, 1977). This is commonly known as squirt flow, and although thought to be unimportant at ultrasonic frequencies, may be significant at sonic or seismic frequencies. This squirt flow is local and is not necessarily aligned with the direction of wave propagation. Instead it occurs locally in directions determined by the geometry of the crack and pore intersections.

Inertial flow is thought to be more important at ultrasonic frequencies. This is caused by relative motion between the rock frame and the saturating fluid as seismic

15
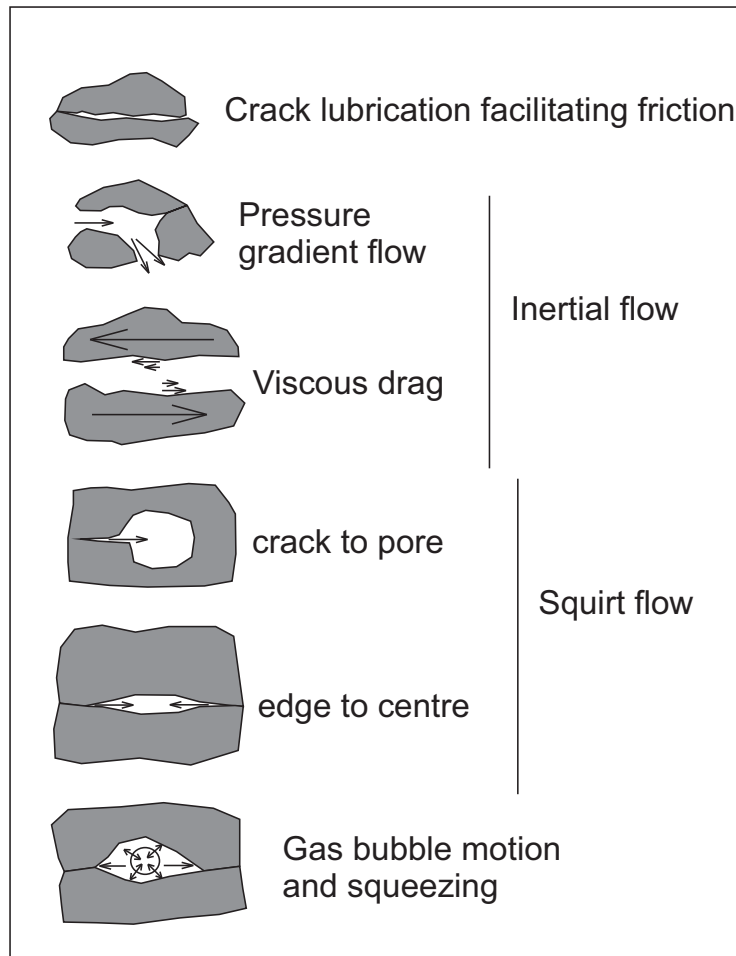
Figure 2.6: Schematic diagram illustrating mechanisms through which pore fluid is thought to contribute to attenuation. Figure adapted from *Johnston et al.* (1979).

waves propagate (*Biot*, 1956a,b, 1962a,b). Mechanisms for this type of energy loss include viscous drag and pressure gradient flow. Viscous drag by pore walls causes shear stresses within the pore fluid, which decay exponentially away from the pore wall with a viscous skin depth that decreases with increasing frequency (see figure 2.6). Pressure gradients may also occur within or between pores as the wave passes. This will induce fluid flow and attenuation of the wave (e.g. *Mavko and Nur* (1979)).

In many cases, rocks in the crust are partially saturated by two or more fluids (e.g. air and water, oil and brine, gas and oil). Where gas bubbles are present, bubble compressibility and movement may also contribute to attenuation. Fluid flow mechanisms may also be enhanced. Thus in partially saturated rocks, the attenuation may be greater than in the fully saturated case. The patchy saturation model attempts to model heterogeneous rock bodies saturated with two or more immiscible fluids. In this model, seismic wave attenuation is explained by wave-induced fluid flow between patches. These potential mechanisms through which the presence of fluids may influence attenuation are summarised in figure 2.6.

2.3 Seismic properties of fault zones

Fault zones are fluid-rich and highly fractured areas. As such, they are regions of low seismic velocity (e.g. *Cochran et al.* (2009)) and high seismic attenuation (e.g. *Rietbrock* (2001); *Blakeslee et al.* (1989)).

Fault gouge is observed to have a lower velocity than its protolith (e.g. *Wang et al.* (1978) and see chapter 4). The fault core is therefore expected to have the lowest velocities. The surrounding fractured damage zone is also expected to have reduced velocities.

It has been shown that the low velocity region around a fault can act as a wave-guide (e.g. *Li and Leary* (1990); *Li et al.* (1994)). Waves trapped within this low velocity wave-guide arrive after the direct body waves as a large amplitude, low frequency, dispersive wave train. These dispersive waves are produced by constructive interference of critically reflected waves inside the low velocity zone (*Peng et al.*, 2003). At Landers and Parkfield, California, the slow trapped waves travel at a velocity 30-40% less than the velocity of the surrounding rock. These wave-guides are observed to be less than 250 m wide and are also zones of high attenuation (e.g. *Li et al.* (1994, 2004); *Peng et al.* (2003)). The wave-guide width may represent the thickness of the fault gouge, or the area of most intense fracturing (*Li et al.*, 1994, 2006). The nature of the trapped waves (including amplitudes and frequency contents) are strongly dependent on the fault-zone geometry and physical properties and may therefore reveal detailed information on fault structure (e.g. *Li and Vidale* (1996)). However, there are many trade-offs to consider. Waveguide width, velocity contrast and attenuation all trade off against each other (*Ben-Zion*, 1998).

17

If the stress field surrounding a fault zone has resulted in fracturing with a preferred orientation, then shear wave splitting may also be observed due to the anisotropy (e.g. *Evans* (1984); *Peng and Ben-Zion* (2004)). Foliation, bedding, or aligned minerals are other possible causes of anisotropy (*Aster and Shearer*, 1992). More than one mechanism may contribute to anisotropy within a region. Where shear wave splitting is observed in fault zones, fast directions are determined to be between the orientation of the regional maximum compressive stress and fault parallel, and may change as the strike of the fault changes (e.g. *Cochran* (2003); *Peng and Ben-Zion* (2004); *Liu et al.* (2004)). In Chi-Chi, Taiwan and Hector Mine, California the anisotropic area around the fault zones is observed to be of the order of one kilometre wide (*Cochran*, 2003; *Peng and Ben-Zion*, 2004) and is often inferred to extend no more than a few kilometres in depth (e.g. *Peacock et al.* (1988); *Savage et al.* (1989, 1990); *Munson et al.* (1995)). The area of observed anisotropy is therefore of greater lateral extent than the area of reduced velocity that acts as a wave-guide. The anisotropic region most likely represents the area of most extensive damage near the fault (i.e. the fault damage zone).

Attenuation anisotropy is also observed, with the slower shear wave experiencing higher attenuation (*Liu et al.*, 2005; *Aster and Shearer*, 1991). This may also be caused by aligned micro-cracks, as commonly inferred for velocity anisotropy. Anisotropic attenuation has been observed in laboratory measurements on rock samples containing aligned cracks (*Thomsen*, 1995). Attenuation anisotropy may be partially responsible for lack of the distinct arrivals for slow shear waves, when fast shear waves give clear arrivals (*Aster and Shearer*, 1991).

In this thesis the effects of fractures, geological fabric and fluids on seismic properties of fault zones are investigated. Studies ranging from laboratory experiments to seismological field investigations allow different scales to be considered and compared. In laboratory investigation, separation of the effects of fracturing and geological fabric on seismic properties is addressed. When investigating temporal changes in fault zones both fracturing and fluid conditions are expected to change. The influences of these mechanisms and how they may interact are discussed.

Part I

The Carboneras Fault, SE Spain

Chapter 3

Introduction to the Carboneras Fault zone area of SE Spain

3.1 The Betic-Rif Orogen

The geology of SE Spain is dominated by the Betic Cordilleras, a mountain range that extends from Alicante to Gibraltar. These mountains form the northern arm of the Gibraltar Arc mountain belt, which surrounds the Alboran Sea, with the Rif Mountains in northern Morocco representing the southern arm (see figure 3.1). This region represents part of the diffuse plate boundary between Africa and Iberia, and is the most westerly extent of the Alpine orogeny. The mechanics and evolution of this plate boundary have attracted much attention.

Rocks of the Betic-Rif orogen are divided into External Zones, Internal zones and intermediate Flysch zones (see figures 3.1, 3.2). In the Betic Cordillera, the External Zone consists of Mesozoic and Tertiary sedimentary rocks which were deposited in shelf (Prebetics) and basin (Subbetics) environments of the Iberian margin. The intermediate Flysch Zone consists mainly of Early Cretaceous to Early Miocene deep marine clastic deposits (*Wildi*, 1983). The Internal Zone, located farther South, consists of mountain ranges of metamorphosed Palaeozoic and Mesozoic rocks separated by intermontane basins. These metamorphic rocks have been affected by Palaeogene-early Miocene deformation and regional metamorphism. A large system of faults, referred to as the Trans-Alboran shear zone, cut across the eastern Betics (*de Larouzière et al.*, 1988). The faults within this system mostly trend NE-SW, with major faults including the NE-SW trending Crevillente, Alhama de Murcia and Carboneras faults and the N-S trending Palomares fault (see figure 3.2). The Carboneras fault, with an onshore extent of 40 km, and an offshore continuation of 100 km is possibly the longest structure in the area.

In this chapter the geology of the Internal Betics is introduced, through which this system of faults cut. The seismicity of the region and the main faults in the Trans-Alboran shear zone are also discussed.
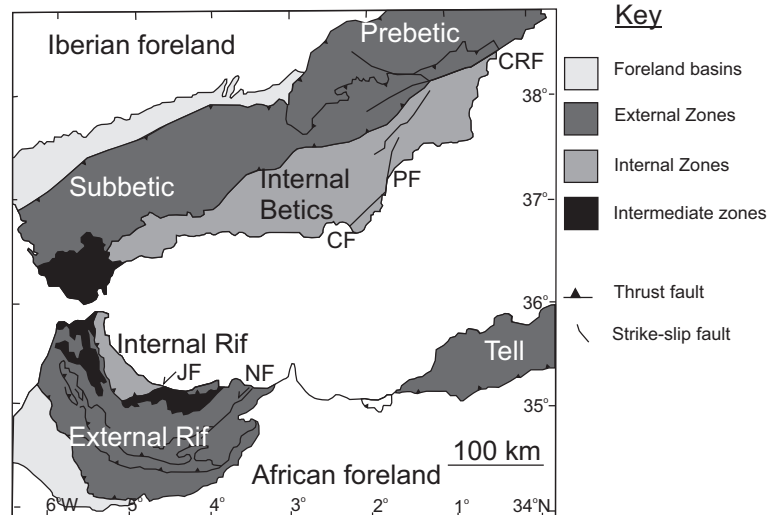
Figure 3.1: Map showing the Internal, External and Intermediate zones of the Betic-Rif orogen. Labelled are the Crevillente Fault (CRF), Palomares Fault (PF), Carboneras Fault (CF), Jebha Fault (JF) and Nekor Fault (NF).

3.2 Geology of the Internal Betic Zone

The Internal Zone of the Betics consists of mountain ranges of metamorphic basement rocks, separated by intermontane basins as well as volcanic rock representing two separate volcanic episodes. The region has been affected by a mixture of compressional and extensional tectonics, which has caused uplift of basement rocks and development of sedimentary basins. The area has been strongly affected by faulting and folding, which remains active today.

3.2.1 Metamorphic Rocks of the Internal Betic Zone

The crustal rocks of the Internal Betic Zone are classically grouped into three major tectonic complexes. In structurally-ascending order these rock units are the Nevado Filabride complex, the Alpujarride complex and the Malaguide complex (*Egeler and Simon*, 1969; *Torres-Roldán*, 1979). The Nevado Filabride complex consists of low-grade metamorphic mica schists and quartzites, and medium-grade metamorphic schists, quartzites, marbles, amphibolites and gneisses (*Egeler*, 1963). Rocks of the Alpujarride complex lie structurally above the Nevado-Filabride complex. These include low-grade metamorphic carbonate rocks (*Kozur et al.*, 1974), phyllites and quartzites (*Egeler and Simon*, 1969) and locally they contain black, medium-grade metamorphic schists (*Vissers*, 1981; *Platt et al.*, 1983). The highest unit, the Malaguide complex, is comparatively thin and mostly eroded away. It consists of non-metamorphic to very low-grade metamorphic carbonate rocks, sandstones, shales and conglomerates (*Soediono*, 1971; *Makel and Rondeel*, 1979).

During the early Miocene (25-20 Ma), the Internal Zones were thrust onto the Flysch

21
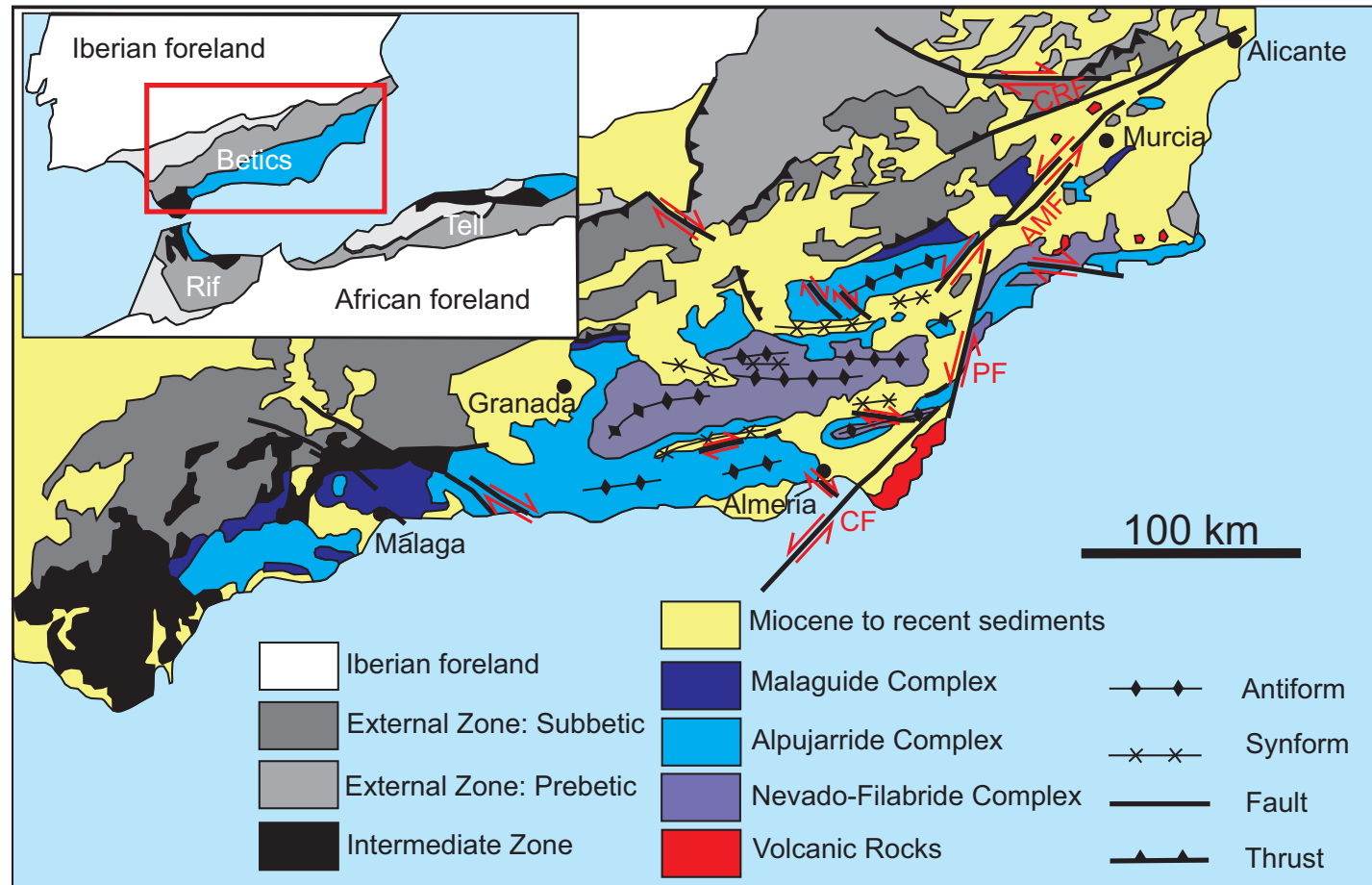
Figure 3.2: Geology of the Internal Zone of the Betic Cordilleras. A number of major faults cut across this area. Labelled are the Palomares Fault (PF), Carboneras Fault (CF), Crevillente Fault (CRF) and Alhama de Murcia Fault (AMF).

zones (e.g. *Lonergan and Mange-Rajetsky* (1994); *Allerton et al.* (1993)). The Alboran domain and adjacent Internal zones underwent considerable extension at the same time (e.g. *Frizon de Lamotte* (1987); *García-Dueñas et al.* (1988); *Platt and Vissers* (1989). Rocks of significantly different metamorphic grade are structurally juxtaposed along major extensional shear zones (e.g. the Alpujarride/Malaguide contact) (*Platt and Vissers*, 1989; *Lonergan and Platt*, 1995; *Aldaya et al.*, 1991). In the basement rocks near Carboneras, these generally low-angle extensional tectonic contacts are often marked by low grade fault rocks. Exhumation and rapid cooling of metamorphic rocks related to this episode occurred from earliest Miocene times to 15 Ma (*Platt and Vissers*, 1989; *Zeck et al.*, 1992; *Zeck*, 1996; *Platt and Whitehouse*, 1999; *Vissers*, 2012). Extension is also evident in crustal thickness variations across the region. The crustal thickness varies from 40 km in the Internal /External Zone boundary in the Betics to about 15 km thickness in the centre of the Alboran Sea (*Banda and Ansorge*, 1980; *Torne and Banda*, 1992). Seismic reflection profiles which traverse the Alboran Sea also show evidence of large-scale normal faulting (*Watts et al.*, 1993; *Comas et al.*, 1992; *Mauffret et al.*, 1992).

The mechanism which caused this episode of coeval compression and extension has been widely investigated (e.g. *Frizon de Lamotte* (1987); *García-Dueñas et al.* (1988); *Platt and Vissers* (1989); *Banks and Warburton* (1991); *Favre et al.* (1991); *García-Dueñas et al.* (1992); *Comas et al.* (1992); *Lonergan and Mange-Rajetsky* (1994); *Jabaloy et al.* (1993); *Watts et al.* (1993); *Platzman et al.* (1993)). Shortening occurred as the result of continued convergence between Africa and Iberia. Two main geodynamic models have been proposed to explain the coeval extension:

1. Slab rollback i.e. back-arc extension due to westward rollback of an eastward-subducting slab at the same time as shortening due to continued convergence of Africa and Iberia.

2. Delamination of lithosphere i.e. initial thickening of the lithosphere during collision, causing a convective (Rayleigh-Taylor) instability to develop. This part of the lithosphere is then removed by convection or delamination, causing rapid uplift and extensional collapse of previously thickened crust.

3.2.2 Volcanic Activity

Volcanism has both accompanied and postdated the extensional episode. Calc-alkaline, potassic, and basaltic volcanism is scattered across the eastern sector of Alboran Sea and Betic Rif systems (*Bellon*, 1981; *Hernández and Bellon*, 1985; *Hernández et al.*, 1987). Relatively large amounts of volcanism are also inferred offshore from both magnetic data and dredging (*Hernández et al.*, 1987).

The earliest volcanic rocks are mostly calc-alkaline and in Spain are restricted to the Cabo de Gata area. The dates obtained for this volcanic suite range from 15-7 Ma,

whereas in the Rif-Tell mountains, dates range from 13-8 Ma (*Bellon*, 1981; *Hernández et al.*, 1987).

A second broad suite of dominantly potassium-enriched rocks with a wide variety of compositions (shoshonitic to lamproitic) were erupted in Spain between 8-5 Ma and in North Africa between 9-4 Ma. The lamproitic volcanic rocks are widely scattered. In Southern Spain, the youngest lavas are Plio-Quarternary (5-1 Ma) alkaline basalts. The youngest lavas in North Africa are also alkaline basalts, ranging in age from Messinian to Quaternary (6-1 Ma).

The older group of volcanics is, in places, strongly hydrothermally altered, e.g. the gold mineralisation of El Palin and La Islica (*Morales Ruano et al.*, 2000; *Carrillo Rosua et al.*, 2000). The younger volcanic series includes the Bréche Rouge (*Serrano and Gonzales Donoso*, 1989; *Uwe et al.*, 2003), characterised by volcaniclastic breccias with the inter-clast volumes infilled with a pink, muddy carbonate matrix rich in micro- and marcofossils that yield mid-Tortonian ages (8-9 Ma).

3.2.3   Sedimentary Basins

The Betic intermontane basins are located in the Internal Zone. These basins developed in Late Serravallian to Early Tortonian times (13-7 Ma). All of these basins have a common sedimentary evolution, characterised by three main sequences which are separated by unconformities of regional significance.

The oldest sequence records coarse-grained sediment shed from prominent uplifts developed in the footwall of the extensional detachments during Late Serravallian -Early Tortonian times (13-7 Ma). The lower part of the sequence was sourced exclusively from the two upper complexes of the Alboran domain. The first appearance of the Nevado-Filabride complex is higher in the sequence, recording the emergence of this lowest metamorphic complex. The second sequence represents a short-lasting (1.8-2 Ma) late Tortonian-Messinian marine inundation of the previously emergent Alboran domain, (*Meijninger*, 2006; *Rodríguez-Fernández and Sanz de Galdeano*, 2006). This sequence includes thick layers of evaporites (mainly salt and gypsum) which were deposited in the deeper parts of the basins, due to repeated sea flooding. This is known as the Mediterranean Messinian Salinity Crisis. Non-marine sedimentary rocks are seen towards the top of the sequence, indicating re-emergence due to relatively rapid uplift (*Rodríguez-Fernández et al.*, 1984; *Montenat et al.*, 1990). This marine inundation may have been caused by subsidence due to extensional tectonics (*Rodríguez-Fernández and Sanz de Galdeano*, 2006). The final sequence is made up of continental sediments which were deposited by braided and meandering rivers, as well as by alluvial fans.

In summary, the lower (Upper Serravallian-Lower Tortonian, 13-7 Ma) and upper sequences (uppermost Tortonian-Upper Messinian, 7-5 Ma) consist of continental clastic sedimentary rocks. The intermediate sequence (Upper Tortonian-Upper Messinian,

7-5 Ma) is made up of marine sedimentary rocks. The first and fastest stage of basin development has been interpreted to record rapid extensional tectonics. Following this, basement uplift and basin continentalisation are recorded with lower subsidence rates.

Two main groups of hypotheses have been proposed to explain the origin of the Betic intermontane basins. As most of the basins display strike-slip structures along their edges, it was initially thought that their origin was related to this strike-slip faulting (e.g. *Montenat et al.* (1987); *Sanz de Galdeano and Vera* (1992)). However, detailed structural studies focused on basin-bounding fault kinematics have shown that the basins were generated in the hanging walls of the main extensional detachment systems responsible for the exhumation of the deeper metamorphic basement units (e.g. *Martínez-Martínez and Azañon* (1997); *Meijninger and Vissers* (2006); *Rodríguez-Fernández and Sanz de Galdeano* (2006)).

During late Tortonian- Early Messinian times (7-6 Ma), a change in the Africa-Europe convergence direction produced a re-arrangement of the Betics in terms of stress-orientation and dominant structures. The major compressional stress shifted from WNW-ESE to NNW-SSE orientation, generating E-W trending compressional folds, NW-SE oriented high-angle normal faults, as well as E-W and NE-SW trending strike-slip faults. These structures have affected the basins and their basements in a complex manner. Strike-slip faults have strongly deformed some of the basin edges, obliterating the previous extensional structures. *Meijninger* (2006) and *Meijninger and Vissers* (2006) propose a late Miocene-Early Pliocene age for the reactivation of former extensional faults in a strike-slip regime (Crevillente and Alhama de Murcia faults).

3.3 Tectonic Structures

The major tectonic structures of the Internal Zone of the Betic Cordillera include E-W compressional folds, NW-SE oriented high-angle normal faults, E-W and NE-SW trending strike-slip faults and the extensional detachments between the metamorphic complexes. These structures are related to approximately NW-SE compression and coeval NE-SW extension since the Miocene. The maximum compression was orientated WNW-ESE during much of the Miocene (25-5 Ma). A change in the convergence direction between Africa and Iberia shifted this to NNW-SSE compression from the Late Miocene (late Tortonian-Early Messinian, 7-6 Ma) onwards.

3.3.1 Folding

Kilometre-scale folding with E-W to ENE-WSW orientation is seen throughout the area, with antiforms coinciding with mountain ranges where the metamorphic rocks crop out. During the Serravalian-early Tortonian (15-7 Ma), the Sierra Nevada and

Sierra de los Filabres started to emerge as large antiforms that folded the extensional detachments (*Martínez-Martínez et al.*, 1995; *Martínez-Martínez and Azañon*, 1997; *Galindo-Zaldivar et al.*, 2003). Large-scale folds continued growing and propagating to the north (*Pedrera et al.*, 2007) and to the south from late Tortonian (7 Ma) with the development of E-W kilometre-scale folds of the Sierra Alhamilla and Sierra Cabrera (*Weijermars et al.*, 1985).

Sedimentary rocks are widely deformed by folds with hundreds of metres amplitude that consistently show a ENE-WSW trend onshore and offshore. These folds deformed the sediments before the Messinian (before 7 Ma) generating a cartographic unconformity between the highly folded upper Tortonian rocks and the less deformed post-Messinian sediments (*Weijermars et al.*, 1985). In the Sierra Alhamilla, the late Tortonian (10-7 Ma) rocks dip 20 degrees in the southern slopes, yet are vertical or even overturned on the northern slops as a consequence of the northward fold vergence (*Weijermars et al.*, 1985; *Sanz de Galdeano*, 1989). ENE-WSW folds affect the Pliocene and Quaternary (5-0 Ma) sediments that extend along the continental shelf of the Almeria Gulf, the Campo de Dalias (*Martin-Lechado et al.*, 2006) and the Nijar basin (*Sanz de Galdeano*, 1989; *Huibregtse et al.*, 1998; *Pedrera et al.*, 2006), indicating the continuity of the deformation after the major Messinian unconformity.

3.3.2 Faulting

Major faults in this region include, among others, the NE-SW trending Crevillente, Alhama de Murcia and Carboneras faults, and the N-S trending Palomares fault. These faults form part of the Trans-Alboran shear zone, a predominantly left-lateral shear zone that extends from Alicante to Almeria and offshore into the Alboran Sea (*de Larouzière et al.*, 1988). Many of the faults in the Trans-Alboran shear zone show signs of recent activity i.e. recorded seismic activity or deformation of recent sediments (*Masana et al.*, 2004).

During the Miocene (25-5 Ma) the Betics were first under a WNW-ESE maximum horizontal stress. However, during the Tortonian (10-7 Ma), the compressional axis rotated to a NNW-SSE direction and several NE-SW and E-W faults were activated or re-activated with sinistral and dextral components respectively (*Montenat et al.*, 1987). The same maximum horizontal stress direction has been maintained until the present, with small variations (*Martinez-Diaz*, 2002).

For example, the Crevillente fault, which forms the northern boundary of the Betic zone, behaved as a dextral fault from late Burdigalian to early Tortonian (17-9 Ma) (*Sanz de Galdeano and Buforn*, 2005). However, the fault was reactivated in a sinistral sense from the late Tortonian (*Allerton et al.*, 1993). Total displacement on the Crevillente fault is estimated to be at least 20 km (*Le Blanc and Olivier*, 1984). Although the fault is presently active, the main stage of movement is considered to be

pre-Tortonian (*Azema*, 1977).

The Alhama de Murcia fault is one of the most active faults in the eastern Betics (*Masana et al.*, 2004). It is a sinistral strike-slip fault (*van Meijninger and Vissers*, 2006), almost continuous along a total length of 100 km. In the central section, the fault zone consists of two strands. The Northern Alhama de Murcia Fault is a reverse fault and dips towards the northwest. The Southern Alhama de Murcia Fault (SAMF) is a left-lateral high-angle reverse fault and dips to the southeast. The two strands join together to the southwest and the SAMF appears to be discontinuous to the northeast (*Martinez-Diaz*, 2002; *Masana et al.*, 2004).

The Palomares fault is another prominent strike-slip fault in the eastern Betics. Unlike the other major faults in this system, the Palomares fault is N-S trending. The fault zone, first mapped by *Völk* (1967), is approximately 4 km wide and is thought to have approximately 16 km of north-south displacement (Booth-Rea et al. 2004). The fault developed since the late Tortonian (7 Ma), and has been active during the Pliocene and Quaternary (5-0 Ma) (*Bousquet*, 1979; *Montenat et al.*, 1987; *Ott d'Estevou et al.*, 1990). It is thought to be responsible for moderate-sized earthquakes (e.g. 1518 Vera earthquake). It bounds the eastern edge of the Vera basin and has been inferred to extend offshore along the seabed and follow the coastline southwards at least to the east of the town of Carboneras (*Westra*, 1969). Whilst its termination is uncertain, the fault could link with the Carboneras fault offshore, which has also been active during the Neogene and Quaternary (25-0 Ma) (*Keller et al.*, 1995; *Bell et al.*, 1997).

The Carboneras fault zone (CFZ) is a major regional left-lateral strike-slip fault that extends 40 km onshore along the Almeria-Nijar basin (*Bousquet and Montenat*, 1974; *Ott d'Estevou and Montenat*, 1985; *Keller et al.*, 1995; *Scotney et al.*, 2000; *Faulkner et al.*, 2003) and continues 100 km offshore along the Almeria Gulf in a NE-SW direction (*de Larouzière et al.*, 1988; *Gràcia et al.*, 2006). Associated splays have also been imaged offshore. The fault initiated in the Middle Miocene, around 11 Ma (*Scotney et al.*, 2000) and the initiation is closely linked to volcanism at this time (*Pedrera et al.*, 2010). Some sections of the fault may still be active. Onshore recent activity of the CFZ is well observed near Barranquete in the SW sector, where N30-45E sub-vertical left-lateral fault surfaces deform Quaternary sediments (e.g. *Boorsma* (1992); *Pedrera et al.* (2006)) and offshore seismic activity has been recorded. The total displacement on the CFZ may be up to 40 km but is at least 15 km (*Rutter et al.*, 2012). The onshore portion of the fault zone has been mapped extensively (e.g. *Faulkner et al.* (2003); *Rutter et al.* (2012). A number of continuous strands of fault gouge are observed, each typically 5 m wide. Two main strands have been identified (referred to as the northern strand and the southern strand), and subsidiary strands exist between them (*Rutter et al.*, 2012). The whole zone of deformation is approximately 1 km wide (*Rutter et al.*, 1986; *Keller et al.*, 1995). It has been determined that some strands of the fault

were active while others were not, as late Miocene sediments overlie some fault strands and are fault bounded by others. The Carboneras fault has been interpreted as a stretching transform fault, with material to the NW of the fault having been stretched, and material to the SE of the fault forming a relatively rigid block (*Rutter et al.*, 2012). The Carboneras fault, along with other left-lateral faults in the region, may form the southern boundary of the stretched Betic-Alboran wedge (*Gutscher*, 2012).

3.4   Present day seismicity

Iberia and Africa converge at a rate of 4.5-5.6 mm/yr with a maximum horizontal stress direction of NNW-SSE (*Martinez-Diaz*, 2002). Studies of seismic slip vectors suggest that the Iberian plate is currently converging toward the African plate following an average NW-SE direction with a velocity of 5.4-5.6 mm/yr. Recent plate motion measurements by GPS suggest 4.5 mm/yr convergence velocity (*Argus et al.*, 1989; *deMets et al.*, 1990, 1994; *Kiratzi and Papazachos*, 1995; *McClusky et al.*, 2003; *Pondrelli*, 1999). The seismicity of the region is mainly related to this convergence (see figure 3.3). The shallow seismicity of the region is broadly distributed, but is mainly within the Internal zones of the Betic and Rif ranges (see figure 3.3). The area is characterised by continuous activity of low to moderate magnitude (< M5.5) earthquakes. Seismicity is particularly dense along the deformation zone controlled by the Alhama de Murcia, Caboneras and Palomares faults in the Betics. Historically, large destructive earthquakes (Medvedev-Sponheuer-Karnik (MSK) intensity IX-X) have also occurred in the region (*IGN*, 2001; *Masana et al.*, 2004; *Lopez et al.*, 2001; *Marin-Lechado et al.*, 2005) (see figure 3.4). Historical and archaeological records suggest that this region has been affected by at least 50 destructive earthquakes over the past 2000 years (*Marin-Lechado et al.*, 2005). The town of Almeria was devastated by earthquakes in 1487, 1522 (MSK IX), 1658 (MSK VIII) and 1804 (MSK IX) and Vera was destroyed in 1518 (MSK IX) and 1863 (MSK VII) (*Buforn et al.*, 1995; *IGN*, 2001; *Marin-Lechado et al.*, 2005). These events have been attributed to motion along the Carboneras and Palomares fault systems (*Keller et al.*, 1995). The 1910 Adra Earthquake (Mw=6.1, MSK VIII) occurred offshore and was probably generated by ESE-WNW trending faults, consistent with moment tensor calculations (*Stich et al.*, 2003). A number of significant historical events are also linked to the Alhama de Murcia fault, notably the Lorca earthquakes of 1579 (MSK VII), 1674 (MSK VIII) (*Martinez Solares and Mezcua*, 2002) and more recently in 2011.

Important seismicity also occurs at intermediate depths (40-150 km deep) in this region (see figure 3.3). Intermediate depth seismicity occurs on both sides of the Strait of Gibraltar. On the east side (i.e. in the western Alboran Sea), epicentres have a north-south distribution (*Buforn et al.*, 2004). This seismicity is possibly linked to an ancient subduction zone or to delamination (*Buforn et al.*, 1995).

28
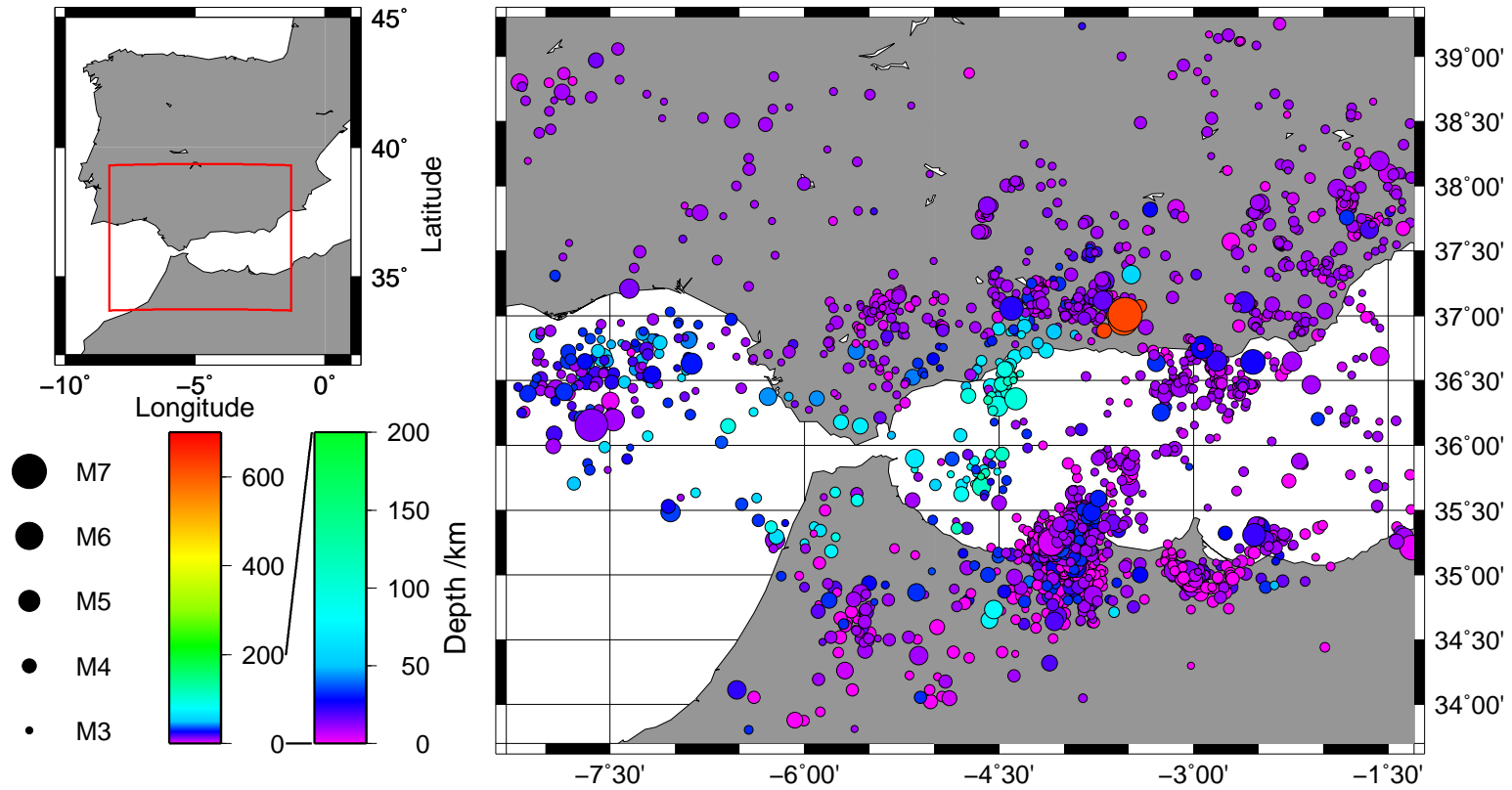
Figure 3.3: Map of seismicity since 1954 in Southern Spain. A location map is shown to the left. The red box indicates the area represented by the main plot. Circles represent seismicity. The size of each symbol represents the magnitude of the earthquake, as indicated. The colour of each symbol represents the depth of the earthquake, as indicated by the colour scales. Data plotted is from the National Earthquake Information Centre (NEIC) catalog (http://earthquake.usgs.gov/regional/neic/).
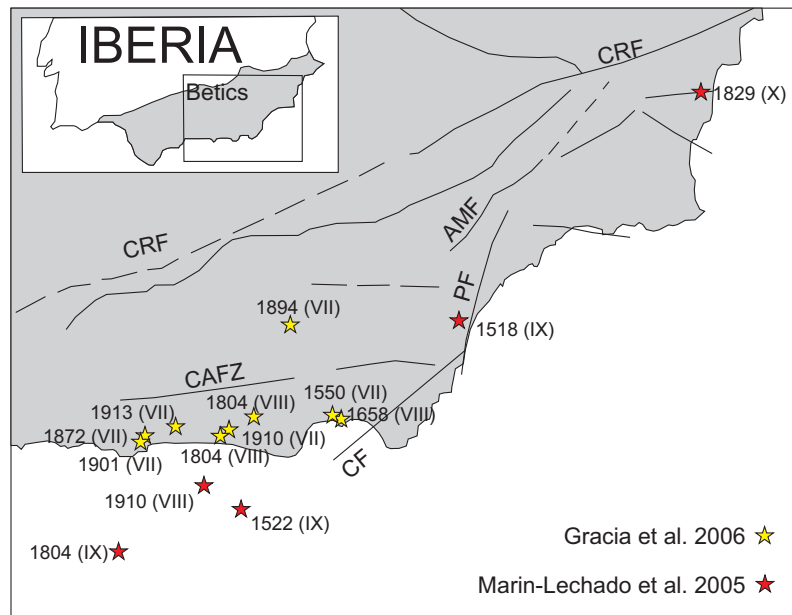
Figure 3.4: Map showing the historical seismicity of SE Spain (*Gràcia et al.* (2006); *Marin-Lechado et al.* (2005)). The inset map shows the location of the main map. Earthquakes of Medvedev-Sponheuer-Karnik (MSK) intensity of VII or greater are shown. Each earthquake is labelled by its MSK intensity and the year in which it occurred. Major faults in the region are also shown. Labelled are the Crevillente Fault (CRF), Alhama de Murcia Fault (AMF), Palomares Fault (PF), Corredor de las Alpujarras Fault Zone (CAFZ) and Carboneras Fault (CF).

Five deep hypocenters (over 600 km depth) have also been recorded in this region (see figure 3.3). The first of these was the 1954 M_w 7.8 earthquake (*Hodgson and Cock*, 1956). This earthquake was felt over a large part of Spain (MSK V) but did not cause damage. Since then, four more earthquakes have occurred in the same area: a m_b 4.8 in 1973 (*Hatzfeld*, 1978), M_w 4.8 in 1990 (*Buforn et al.*, 1991, 1997), M_w 4.3 in 1993 (*Buforn*, 2008) and M_w 6.2 in 2010 (*Buforn et al.*, 2011). Tomographic studies in this area have shown the existence of an anomalous body with a high seismic velocity between 200 -700 km depth in this region. It has been proposed that a former subduction slab (*Zeck*, 1996) or a detached block of lithospheric mantle, sufficiently cold and rigid to generate earthquakes, may exist in this region (*Udías and López Arroyo*, 1972; *Chung and Kanamori*, 1976; *Udías et al.*, 1976; *Grimison and Chen*, 1986; *Buforn et al.*, 1991, 1997).

3.5 Summary

The Carboneras fault zone is a major structure within the Trans-Alboran shear zone, which forms part of the diffuse plate boundary between Africa and Iberia. The surrounding region is geologically complex and includes mountain ranges (sierras) composed of metamorphic basement rocks, as well as intermontane basins with a common sedimentary evolution. The area has also experienced two volcanic episodes. The evolution of this region since Miocene times has been characterised by NW-SE shortening and coeval NE-SW extension, which may have been caused by removal (delamination) of lithospheric material or by back-arc extension due to an eastward-subducting slab rolling back to the west. The tectonic evolution has caused significant folding and faulting in the region.

Chapter 4

Velocity measurement of Carboneras mica schist and fault gouge

4.1 Introduction

Seismic imaging is often used as a method of investigating fault zone structure at depth. Successful interpretation of seismic images relies on an understanding of the influences of seismic properties. Therefore, as part of a project aimed at seismically imaging the Carboneras fault zone of SE Spain, laboratory measurements were performed on samples of fault gouge and its protolith. Using ultrasonic waves, the velocities of mica-schist rock and gouge are measured at a range of confining pressures in order to determine the velocity contrasts expected at a range of depths (up to approximately 3 km). As the mica schist appears strongly anisotropic in structure, the velocity anisotropy is also investigated. The effect of fracturing on the velocities measured is explored through cyclic loading experiments. The strong foliation present in the rock causes strong velocity anisotropy and shear wave splitting. Increased cracking in cyclic loading experiments causes a relatively small change in velocity. Gouge velocities are measured to be less than those through its protolith. A greater difference is seen between the fast and slow directions in the rock samples than between the fault gouge and rock. These results are discussed in terms of seismic investigations of the fault zone.

4.1.1 Carboneras fault zone, SE Spain

The Carboneras fault is a major left-lateral strike-slip fault in SE Spain (see figure 4.1). It has an onshore extent of 40 km, and continues offshore for another 100 km (*Gràcia et al.*, 2006). Associated splays have also been imaged offshore. The fault initiated in the Middle Miocene, around 11 Ma (*Scotney et al.*, 2000) and the offshore section may still be active, as it cuts recent sedimentary units. The total displacement on the CFZ may be up to 40 km but is at least 15 km (*Rutter et al.*, 2012). Regional compressional
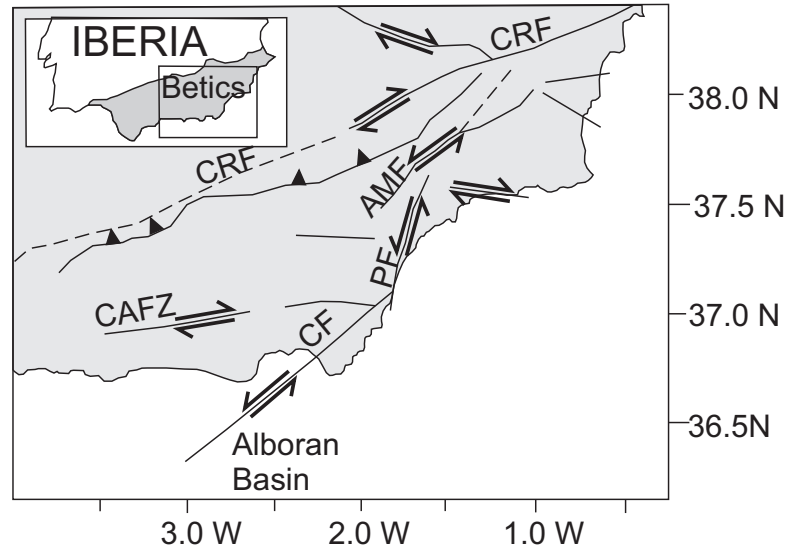
Figure 4.1: Map showing the location of the Carboneras fault in SE Spain. A number of major faults cut across this area. Labelled are Crevillente Fault (CRF), Alhama de Murcia Fault (AMF), Palomares Fault (PF), Corredor de las Alpujarras Fault Zone (CAFZ) and Carboneras Fault (CF).
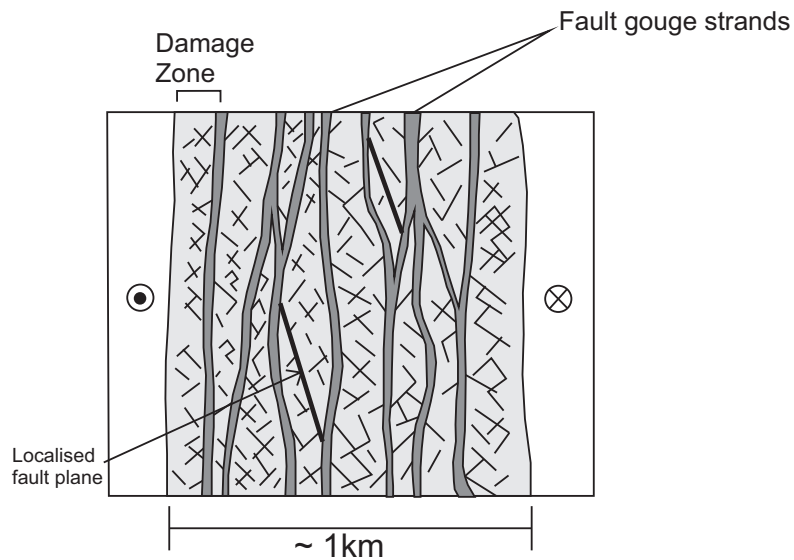
Figure 4.2: Schematic cross-section, showing the structure of the Carboneras fault zone as suggested by *Faulkner et al.* (2003), based on field mapping.

tectonics due to the convergence of Africa and Iberia have caused the onshore section of the fault to be exhumed from an estimated depth of 1.5-4 km during the last 10 Ma (*Faulkner*, 1997).

The onshore portion of the fault zone has been mapped extensively (e.g. *Faulkner et al.* (2003); *Rutter et al.* (2012). A number of continuous strands of fault gouge are observed, each typically ∼5 m wide. Two main strands have been identified (referred to as the northern and the southern strand), and subsidiary strands exist between them (*Rutter et al.*, 2012). Lenses of variably damaged protolith lie between the fault strands. Also included in the fault zone are blocks of dolomite that contain thin (<1 cm thick) fault planes. At the margins of the fault zone, a fractured damage zone of approximately 100 m width is inferred. The whole zone of deformation, including the layers of fault gouge, the included blocks of country rock and the damage zone, is approximately 1 km wide (*Rutter et al.*, 1986; *Keller et al.*, 1995)). This style of faulting is summarised in figure 4.2. It has been determined that some strands of the fault were active while others were not, as late Miocene sediments overlie some fault strands and are fault bounded by others. The strands of fault gouge are thought to exhibit distributed deformation and to have strain hardening and/or velocity hardening characteristics (*Faulkner et al.*, 2003, 2008). As the Carboneras fault developed, strain hardening in the fault gouge would spread the deformation across each layer. Multiple layers develop as frictional lock-up of earlier strands occur. The mechanical strength of the fault gouge and its protolith are thought to be similar due to the wide zone of distributed deformation that is observed (*Faulkner et al.*, 2008).

The strands of fault gouge in the mapped sections of the Carboneras Fault zone are principally derived from graphitic mica schist. This is part of the Nevado-Filabride complex, which forms part of the metamorphic basement of the region. A strong, pervasive, milimetre-scale foliation is present in the mica schist, commonly trending ENE. The schist is dominated by phyllosilicate (mostly muscovite) and is often cut by quartz veins. The fault gouge is also highly foliated and includes fragmented quartz veins.

4.2 Methods

4.2.1 Laboratory set-up

P and S wave velocities through mica schist rock and fault gouge were measured in the laboratory. Ultrasonic waves were pulsed through the samples using piezoelectric ceramics as sources and receivers. Piezoelectric crystals with different polarisation directions were used to simulate P and S waves. The orientation of a sample relative to the polarisation of the S waves could be adjusted before an experiment. Two sample assemblies were used (one in a uniaxial press and one in triaxial confinement). Details
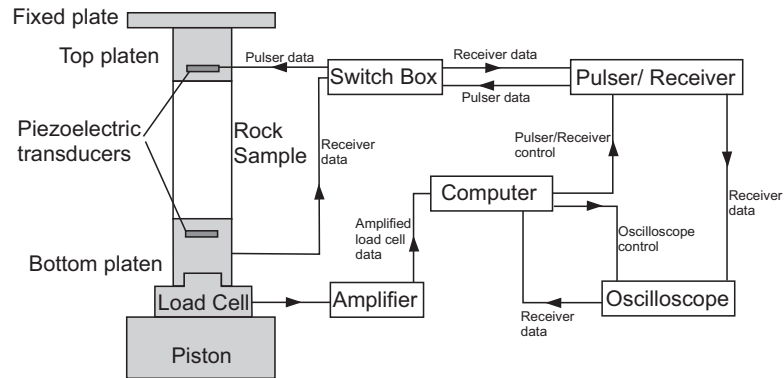
Figure 4.3: Schematic diagram illustrating the main components in the laboratory set-up and how they interact.

Figure 4.4: Schematic diagram showing the geometry of the piezoelectric crystals in the sample assemblies. The two pulsing crystals are shown to the left, and the three receiving crystals to the right. The crystals shown in pink pulse waves with a P-wave polarisation i.e. polarisation direction parallel to the direction of travel. Those shown in blue and green pulse waves with S-wave polarisations. The polarisation directions are indicated by the arrows.
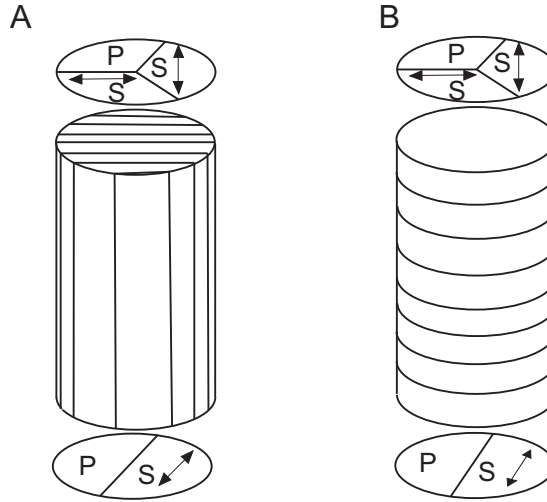
Figure 4.5: Schematic diagram illustrating the orientation of the main foliation of the mica schist through the samples. A. shows the orientation of the foliation in x- or y-orientation samples. B. shows the orientation of the foliation in z-orientation samples. Also shown is the standard geometry of the P and S piezoelectric crystals used in the experiments unless otherwise stated. For the x- and y-orientation samples (A) the polarisation directions of the receiving S wave crystals are parallel and perpendicular to the foliation. The polarisation direction of the pulsing S wave piezoelectric is at 45 degrees to this.

of each sample assembly are summarised below. Full details of the sample assemblies used are given by (*Blake*, 2011). Ultrasonic waves were pulsed through rock samples and recorded using the sample assemblies and ultrasonic measurement system described below and summarised in figure 4.3.

Uniaxial Sample Assembly

The uniaxial sample assembly consists of a top and bottom platen, between which the rock sample is placed in an unconfined state. The bottom platen has one P wave and one S wave piezoelectric ceramic. Two separate top platen arrangements are available. One has a P wave piezoelectric ceramic, and a single S wave piezoelectric ceramic. The other has a P wave ceramic and two S wave piezoelectric ceramics, with polarisation directions perpendicular to each other. The piezoelectric ceramics are attached using silver-loaded epoxy adhesive. A backing material is also attached (see below). The uniaxial sample assembly is placed in a standard uniaxial press, between a fixed rigid plate and moving hydraulic piston, which is controlled by a hand-operated valve pump. A load cell is used to measure the applied load. The load cell is capable of accuracy of ± 7.5 N.

Hydrostatic Sample Assembly

The hydrostatic sample assembly consists of: top plug, top and bottom platen, top and bottom platen holder. The top platen has one P wave and one S wave piezoelectric ceramic. The bottom platen has a P wave and two S wave piezoelectric ceramics. This geometry of the crystals is summarised in figure 4.4. This sample assembly was placed in a pressure vessel with silicon oil used as a confining fluid. The sample is kept separate from the confining medium by placing it in a PVC (PolyVinyl Chloride) jacket. The PVC jacket seals on o-rings at the top and bottom platens. The confining pressure and load is controlled by a combination of servo-controlled pumps. A high pressure pipe allows the introduction of pore fluid into the sample. However, pore fluids were not introduced into the experiments presented in this thesis.

Ultrasonic measurement system

The piezoelectric ceramic used has a fundamental frequency of 1.5 MHz. Sintered stainless steel is used as a backing material. The backing material controls the vibration at the face of the piezoelectric crystal to which it is attached. It protects the crystal from the effects of slight movements of the cables. As it is difficult to soft solder to stainless steel, a thin sheet of copper is glued onto the stainless steel using silver-loaded epoxy. High frequency coaxial cables are then soldered to the copper.

A pulser/receiver generates the energy that drives the transmitting piezoelectric ceramic and amplifies the electrical response arriving from the receiving piezoelectric ceramic. A JSR DPR300 pulser/receiver operated in through-transmission mode was used. In the through-transmission mode, one piezoelectic ceramic is used to generate the elastic wave and another piezoelectic ceramic is used to receive the elastic wave that propagated through the rock sample. The pulser/receiver can be controlled manually or through a computer using the JSR Instrument Control Panel program. A 300 MHz bandwidth digital oscilloscope (Tektronix TDS 3032B) is used for displaying and recording the received pulse. The oscilloscope can be controlled manually or through a computer using the Tektronix Escope remote control program. A switch-box is used to select different combinations of pulsing and receiving crystals.

4.2.2   Sample preparation

Samples were cored from two blocks of Carboneras mica schist, referred to as A and B, both collected from $30°S$ 0597527 4101241 (UTM European 1950). In hand specimen, block A was observed to be more micaceous than block B. Samples were drilled using diamond-tipped coring drills with diameters of 20 mm (hydrostatic samples) and 25mm (uniaxial samples). Uneven ends were cut using a diamond blade circular saw, and a grinding machine was used to square the samples. The coring drill, diamond blade saw and grinding machine use water as a coolant. An oven is used to dry the cores

Figure 4.6: Photo showing collection of gouge samples. Copper tubes were hammered into the fault gouge. They were then removed and the ends of the tubes were secured with glue.

at 80° C. Cores were drilled perpendicular and parallel to the main foliation of the mica schist (see figure 4.5). Samples cored perpendicular to the foliation were referred to as z orientation whereas samples parallel were referred to as x or y orientation, with x perpendicular to y (see figure 4.5). Samples varied in length due to difficulty in coring. Cores tended to break easily along the strong foliation in the rock during sample preparation. The gouge samples were collected by hammering a copper tube into the fault gouge (see figure 4.6). Sample MS1z was collected from $30°S$ 0596415 4099213 (UTM European 1950). Glue was used to secure the ends of the samples in transport. After sample collection, the copper tubes were reduced in thickness from 2 mm to 1 mm in a lathe. The ends were removed and the sample was cut to length using a circular saw with water as a coolant. Gouge samples were dried on top of an oven.

4.2.3 Experimental Procedure

Four main types of experiments were carried out on rock samples from the Carboneras mica schist. The gouge sample underwent a fifth, different experimental procedure. Each of these are detailed below. Information on samples used in each experiment are summarised in table 1. Except where otherwise discussed, the piezoelectric ceramics were orientated as shown in figure 4.5.

Uniaxial Experiments

Samples AZ3, AY2 and AX1 were taken to failure in the uniaxial press. This allowed investigation of P and S velocities under different loads, in an unconfined state. Determining the uniaxial compressive strength also allowed the failure load at confining pressure to be estimated.

Confining Pressure experiments

Using the hydrostatic sample assembly, velocities were measured at confining pressures up to 80 MPa. This type of experiment was applied to samples BZ2 and BY1.

Shear-Wave Splitting

Unfortunately, coupling of the two receiving S-wave piezoelectric crystals meant that shear wave splitting could not be investigated during the other experiments. Therefore, shear waves with polarisations parallel and perpendicular to the to the foliation were pulsed through sample BX1 by manually rotating the sample by 90 degrees. Shear waves pulsed through the sample in perpendicular polarisations were recorded at a confining pressure of 25 MPa.

Cyclic-loading experiments

Cyclic loading was carried out in the hydrostatic pressure vessel. A sample is taken to 40% of its expected failure pressure. On increasing cycles the sample is taken closer to failure, and then unloaded. Rocks are significantly weakened or fatigued when subjected to cyclic loading (*Haimon*, 1978). This induces microcracks in the sample. With each new cycle the rock is expected to have more microcracks. The effect of this on velocity was measured at confining pressures of 25 MPa (samples BZ3 and BY2) and 50 MPa (samples BZ4 and BY1), corresponding to depths of approximately 1 km and 2 km, respectively. This allows us to determine how velocity might change in the damage zone close to a fault strand, as it is well established that fracture density increases from the undamaged state to that commensurate with failure immediately adjacent to the fault (*Mitchell and Faulkner*, 2009).

Cyclic Confining Pressure Experiments for fault gouge

Fault gouge samples were repeatedly subjected to confining pressure of 0 to 60 MPa and velocities measured. Shortening of the sample throughout was recorded using the hitpoint method in order to calculate true velocity measurements. In the hitpoint method the piston is moved towards the sample until a small load is detected when contact is made.

Table 4.1: Summary of samples

Sample number	Length (mm)	Diameter (mm)	Experiment	Failure Load (MPa)
AZ3	39.8	25.5	uniaxial	119
AY2	47.4	25.5	uniaxial	51
AX2	38.8	25.5	uniaxial	22
BZ2	50.9	20.0	confining pressure	n/a
BZ3	52.6	20.0	cyclic (25MPa)	132
BZ4	36.3	20.0	cyclic (50MPa)	212
BY2	36.9	20.0	cyclic (25MPa)	176
BY1	53.0	20.0	confining pressure, cyclic (50MPa)	265
BX1	39.2	20.0	shear wave splitting	n/a
MS1z	45.0	19.0	gouge cyclic	n/a

4.2.4 Data Processing

Arrival times were manually picked as the first major deflection recorded. S wave traces can sometimes have strong reflections or conversions arriving before the main S arrival. This can lead to ambiguity in the pick-time. The traces that we have recorded generally show clear arrivals. The arrival times can be difficult to pick at low load values, when recordings are of lower amplitude. Errors associated with the velocity and V_P/V_S measurements were estimated by picking a maximum and minimum arrival time for each trace. The error was greater when arrivals were unclear or the recorded signal was noisy. The arrival times were corrected for time-of-flight through the sample assembly itself. This has been measured previously by *Blake* (2011). The data collected on the hydrostatic sample assembly contained high frequency (>3 MHz) noise, most likely electrical noise. Therefore, these traces were filtered before arrival times were determined. This aided in picking the arrival times. Filters used are discussed in more detail below.

4.3 Results

4.3.1 Uniaxial Experiments

Uniaxial experiments were carried out using samples cored perpendicular and parallel to the main foliation in the mica schist. Examples of traces pulsed and recorded on P-polarisation crystals (P-P traces) are shown in figure 4.7A and examples of traces both pulsed and recorded on S-polarisation crystals (S-S traces) are shown in figure 4.7B. The determined P and S velocities for these samples are shown in figure 4.8. The velocities increase with increasing axial stress. Cracks orientated perpendicular to the applied pressure will close as the pressure increases, causing an increase in the measured velocities. An increase in velocity could also be due in part to bulging and shortening of the samples in these unconfined tests. By comparing velocities measured in samples of different orientations we can observe an anisotropy (see figure 4.8). Waves travel much more quickly in the sample cored parallel to the foliation. P-waves travel at velocities of 4700 ms^{-1} to 5500 ms^{-1} through these samples, whereas they travel at between 2500 ms^{-1} to 4000 ms^{-1} in the samples with perpendicular orientation. S-waves travel at velocities of approximately 4000 ms^{-1} in samples cored parallel to the foliation, compared to 2000 ms^{-1} to 2500 ms^{-1} in the samples with perpendicular orientation. V_P/V_S ratios are also calculated and are shown in figure 4.9. The greatest changes in V_P/V_S ratio are in the sample cored perpendicular to the foliation. It is interesting to note that two of the three samples fail at approximately the same V_P/V_S ratio (1.5).
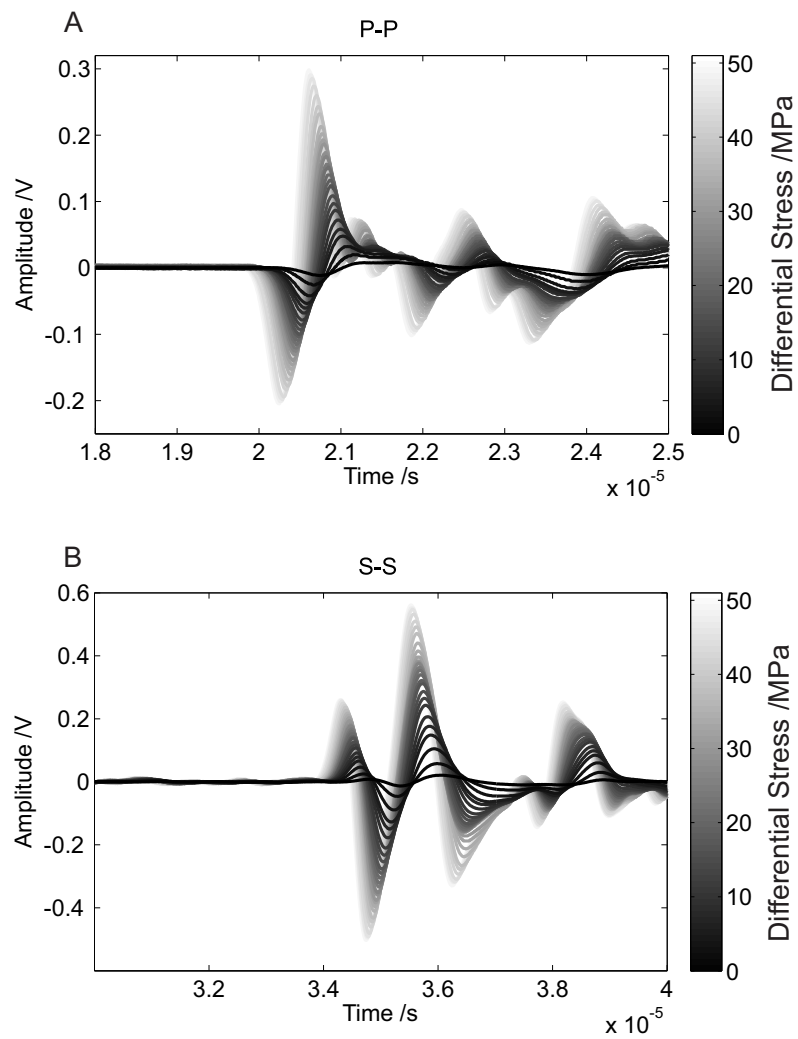
Figure 4.7: A. P-P and B. S-S traces recorded on the uniaxial sample assembly through sample AY2. Traces recorded at low to high differential stress are shown, as indicated by the grey-scale.
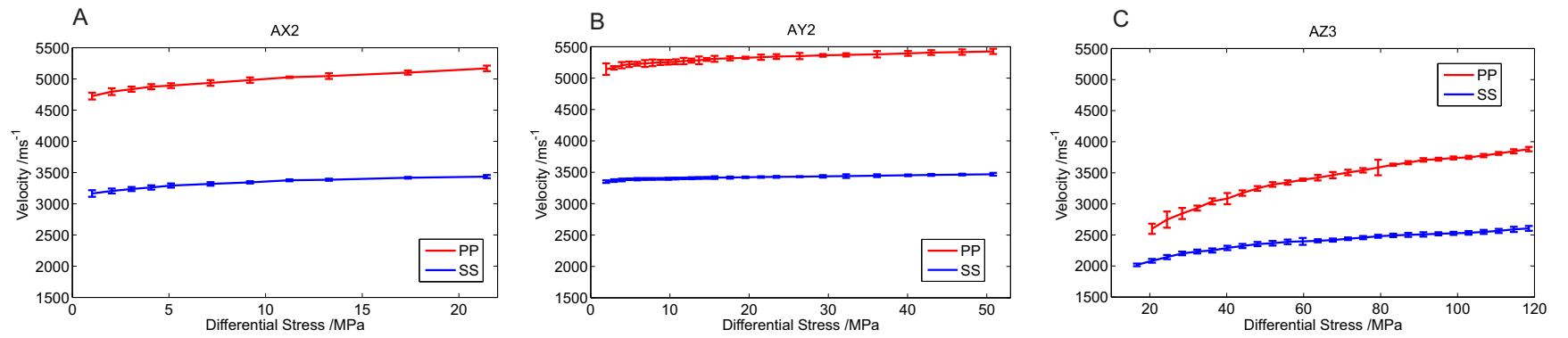
Figure 4.8: Measured P-P and S-S- velocities for samples A. AX2, B. AY2, and C. AZ3. By comparing velocities shown in A. and B. with those in C., a strong velocity anisotropy is observed. The same scale is shown on all y-axes for easy comparison.

Large differences in velocities measured in different orientations of samples suggest that the foliation has a strong effect. Waves can travel much more quickly along the foliation than across it. Measured velocities through the z-orientation sample are of the order of 30% less than those through the y-orientation sample. The largest changes in velocity with increasing pressure occur in the z-orientation sample, as do the largest changes in V_P/V_S ratio. This suggests that the greatest change in crack density occurs in this orientation of sample.
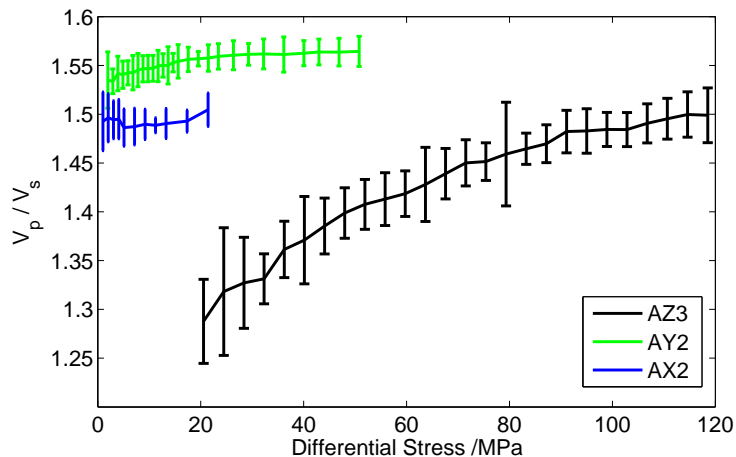
Figure 4.9: V_P/V_S ratios for samples AZ3 (black), AY2 (green) and AX2 (blue).

4.3.2 Confining Pressure Experiments

Traces were recorded at confining pressures up to 80 MPa in samples cored parallel and perpendicular to the main foliation. Examples of traces recorded in the hydrostatic sample assembly are shown in figure 4.10. P-wave traces were low-pass filtered at 3 MHz, with a filter order of 16. S-wave traces were low-pass filtered at 3 MHz, with a filter order of 4. Examples of filtered and unfiltered traces are shown in figure 4.10.

Velocities increase with increasing confining pressures (see figure 4.11). This can be interpreted as crack closure with increasing pressure. In the sample cored parallel to the foliation (y-orientation), P-wave velocities are seen to increase from 5200 ms^{-1} to 5600 ms^{-1} and S-wave velocities are seen to increase from 3400 ms^{-1} to 3700 ms^{-1}. In the sample cored perpendicular to the foliation (z-orientation), P wave velocities are observed to increase from 3000 to 3900 ms^{-1} and S wave velocities from 2300 to 2600 ms^{-1}. This causes an increase in the V_P/V_S ratio in the sample cored perpendicular to the foliation. However, the V_P/V_S ratio stays relatively constant in the y-orientation sample. As with the uniaxial experiments, a strong difference in both P and S velocity is seen in samples of different orientations. Waves can travel much more quickly in y-orientation samples than in z-orientation samples. Velocities measured through z-orientation samples are of the order of 30% less than those measured through y-

44
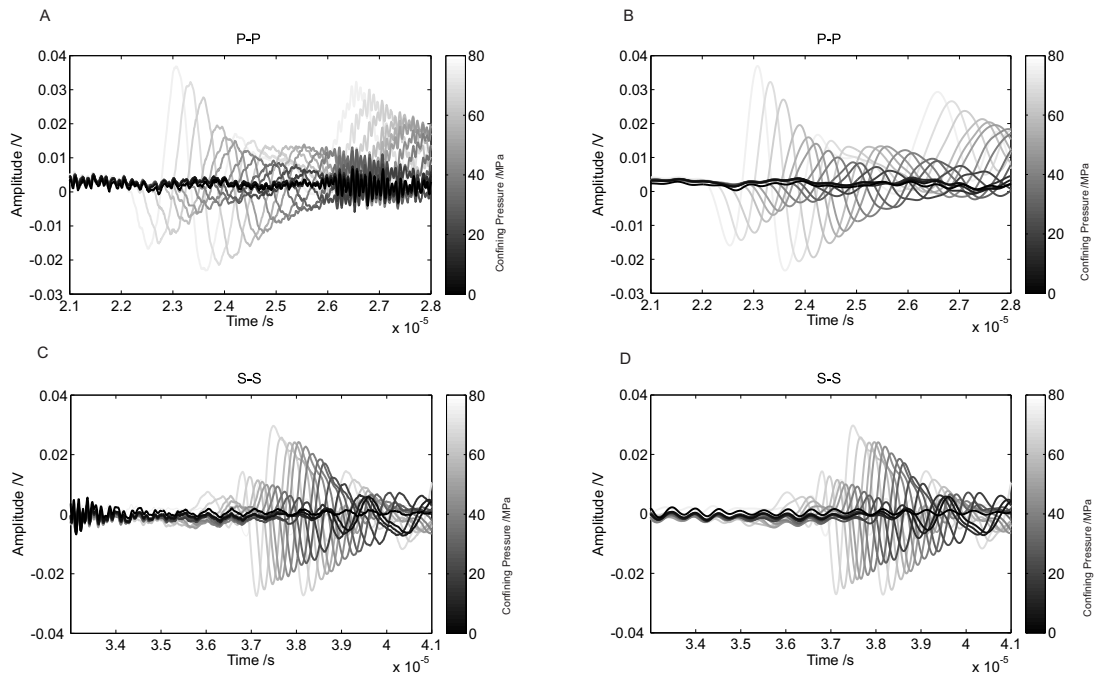
Figure 4.10: A. unfiltered P-P traces, B. filtered P-P traces, C. unfiltered S-S traces and D. filtered S-S traces. Traces recorded at low to high confining pressures are shown, as indicated by the grey-scale.

orientation samples. The greatest changes in velocity and V_P/V_S are measured in the sample cored perpendicular to the foliation, suggesting that the greatest changes in crack density occurred in these samples.
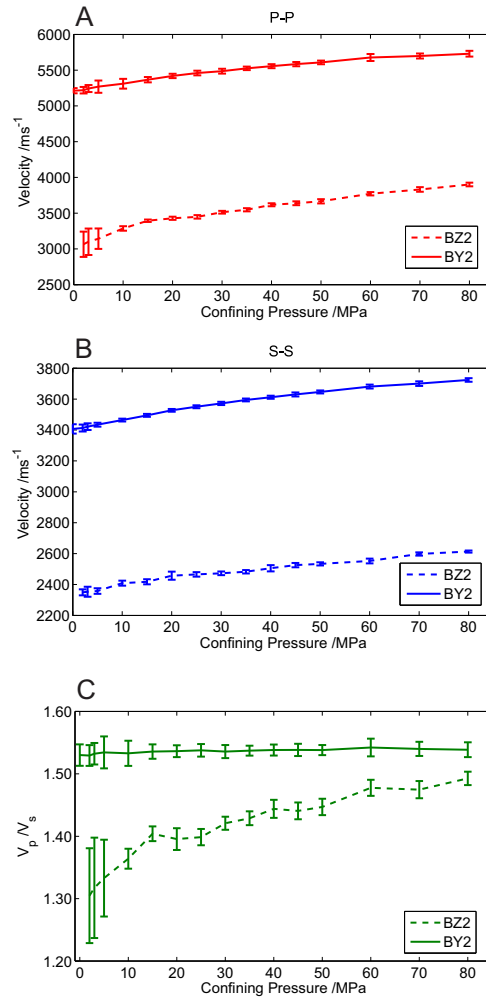
Figure 4.11: A. P velocities, B. S velocities and C. V_P/V_S ratios calculated for samples BZ2 and BY2 as a function of confining pressure. By comparing the velocities measured from the two samples (i.e. solid lines with dashed lines), strong anisotropy is seen in the velocity measurements. Smaller error bars are seen when clear arrivals are observed.

Shear Wave Splitting
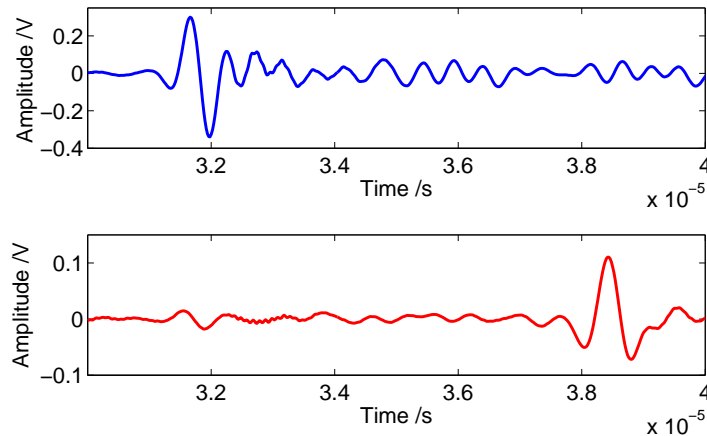
Figure 4.12: Shear waves recorded for sample BX1, with shear wave polarisations parallel to and perpendicular to the foliation in the rock sample.

Throughout the hydrostatic experiments, S waves recorded on the two crystals with perpendicular polarisations were observed to be identical. It appears that the two crystals are in some way coupled. This prevented shear wave splitting measurements throughout the previous experiments. However, given that such a dramatic difference in velocity is observed between samples of different orientations, the occurrence of shear wave splitting was investigated. Sample BX1 was taken to a confining pressure of 25 MPa, with the polarisation of both the pulsing and receiving S crystals aligned to the foliation. This was then repeated with the same sample, rotated by 90 degrees i.e. the polarisation directions of both the pulsing and receiving S wave crystals were perpendicular to the foliation in the sample. The traces recorded in these experiments are shown in figure 4.12. It is observed that the S waves arrive at different times. The later S wave appears to be of lower amplitude, and with a shorter wave-train, suggesting that it is also more highly attenuated. The S wave arrival times correspond to velocities of 3400 ms^{-1} and 2200 ms^{-1}. This agrees well with the S wave velocities measured in different sample orientations at 25 MPa confining pressure in the hydrostatic confining pressure experiments. The velocity of the slower S wave is 35% less than the faster S wave. This corresponds to a very significant amount of shear-wave splitting.

4.3.3 Cyclic Loading Experiments

Cyclic loading was carried out at confining pressures of 25 MPa and 50 MPa on samples cored parallel and perpendicular to the foliation. Microcracks are opened or closed with increasing cycles and changes in stress, both of which cause changes in the velocity measured. Cyclic tests allow the effects of fracture damage and stress changes on velocity measurements to be isolated. For each of these experiments, by plotting traces

at the same load, but on successive cycles, we can see that there is in general only a small difference in the arrival times (e.g. see figure 4.13). Differences in arrival time are approximately within the error of the pick-times. We therefore have considered not only the manual picks of the first deflection, but also the time of the first maximum and the first minimum, which can be automatically picked. As with the hydrostatic confining pressure experiments, traces were filtered before processing.

25 MPa Confining Pressure: Y-Orientation

Figure 4.13: A. unfiltered and B. filtered P-P traces recorded through sample BY2. C. unfiltered and D. filtered S-S traces through sample BY2. The traces shown are recorded at the same load value, but on successive cycles.

Figure 4.14: A. P-P velocities, B. S-S velocities and C. V_P/V_S ratio through sample BY2 during a cyclic loading experiment.

Sample BY2, cored parallel to the foliation, was subjected to cyclic loading at 25 MPa confining pressure. Recorded P-P and S-S traces measured at a constant load on successive cycles are shown in figure 4.13. Changes in arrival times are observed, most significantly for the final cycle, which has a relatively late arrival for both the P-P and S-S traces. Both filtered and unfiltered traces are shown, to illustrate that these small changes in arrival time are not affected by the filter. However, arrival times are more easily picked on the filtered traces. The velocity changes calculated from these changes in arrival time are shown in figure 4.14. These changes are approximately within error of each other. The changes in time until the initial arrival, the first minimum and the first maximum show more clearly the changes in velocity. The first 3 cycles shown have very similar arrival times. However, the final cycle shows a later arrival. This is most likely due to micro-fracturing as the rock sample approaches failure.

25 MPa Confining Pressure: Z Orientation

Figure 4.15: A. unfiltered and B. filtered P-P traces recorded through sample BZ4. C. unfiltered and D. filtered S-S traces through sample BZ4. The traces shown are recorded at the same load value, but on successive cycles.
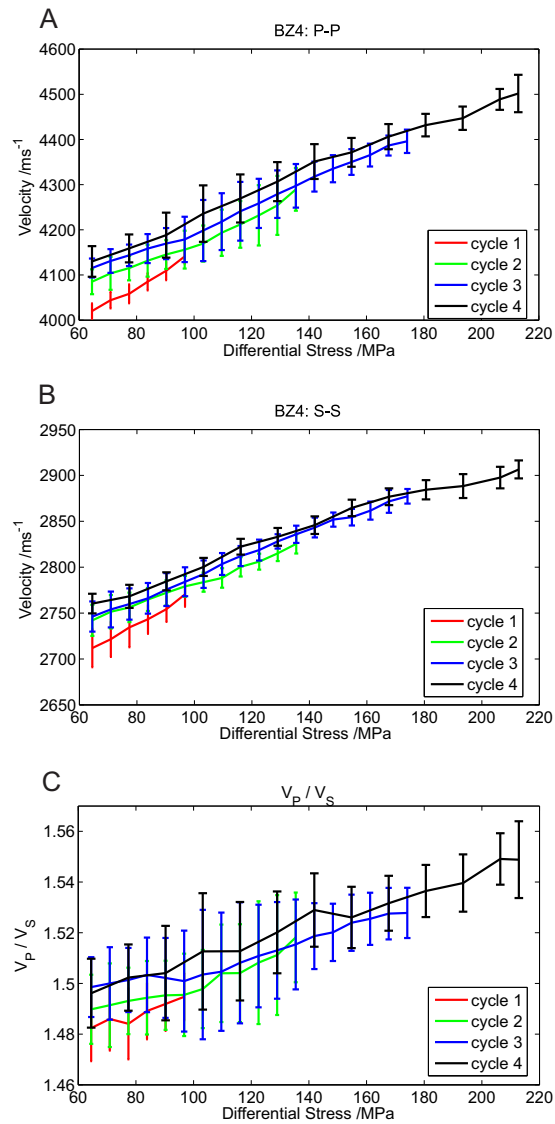
Figure 4.16: A. P-P velocities, B. S-S velocities and C. V_P/V_S ratio through sample BZ4 during a cyclic loading experiment.

Sample BZ4, cored perpendicular to the mica-schist foliation, was also subjected to cyclic loading at a confining pressure of 25 MPa. P-P and S-S traces recorded at constant load are shown in figure 4.15. With increasing cycles, the signal is observed to arrive earlier, with the most significant change between the first and second cycles. This is equivalent to an increase in velocity with increasing cycles in both the P and S velocities (see figure 4.16). This is also apparent in the times until the first minimum and first maximum. This increase in velocity with increasing arrival times is likely due to progressive closure of the cracks along the foliation surfaces, perpendicular to the load that is applied.

50 MPa confining pressure: Y Orientation
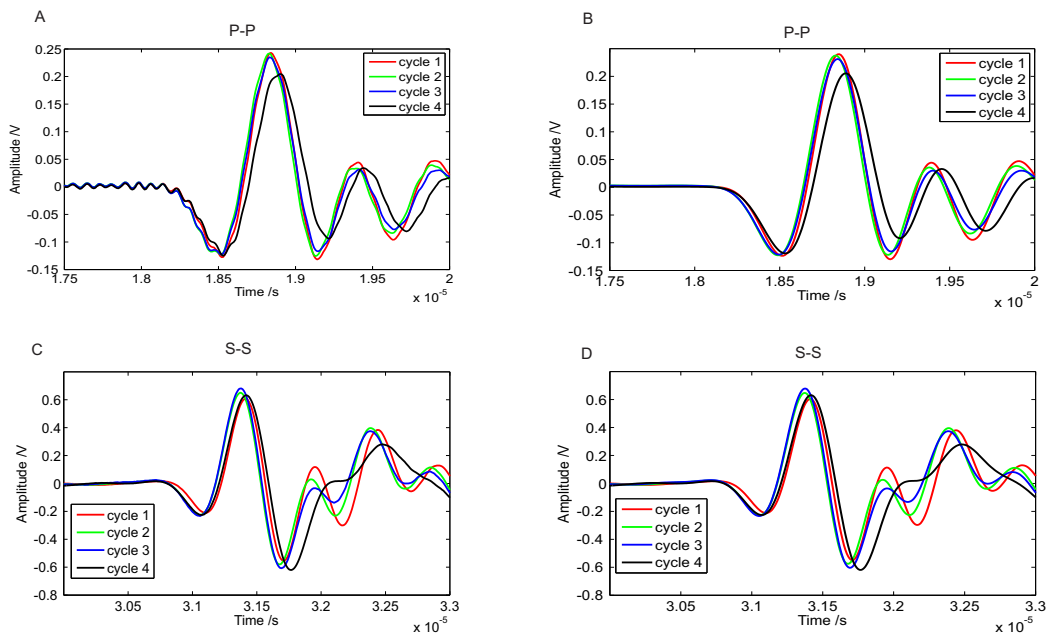
Figure 4.17: A. unfiltered and B. filtered P-P traces recorded through sample BY1. C. unfiltered and D. filtered S-S traces through sample BY1. The traces shown are recorded at the same load value, but on successive cycles.
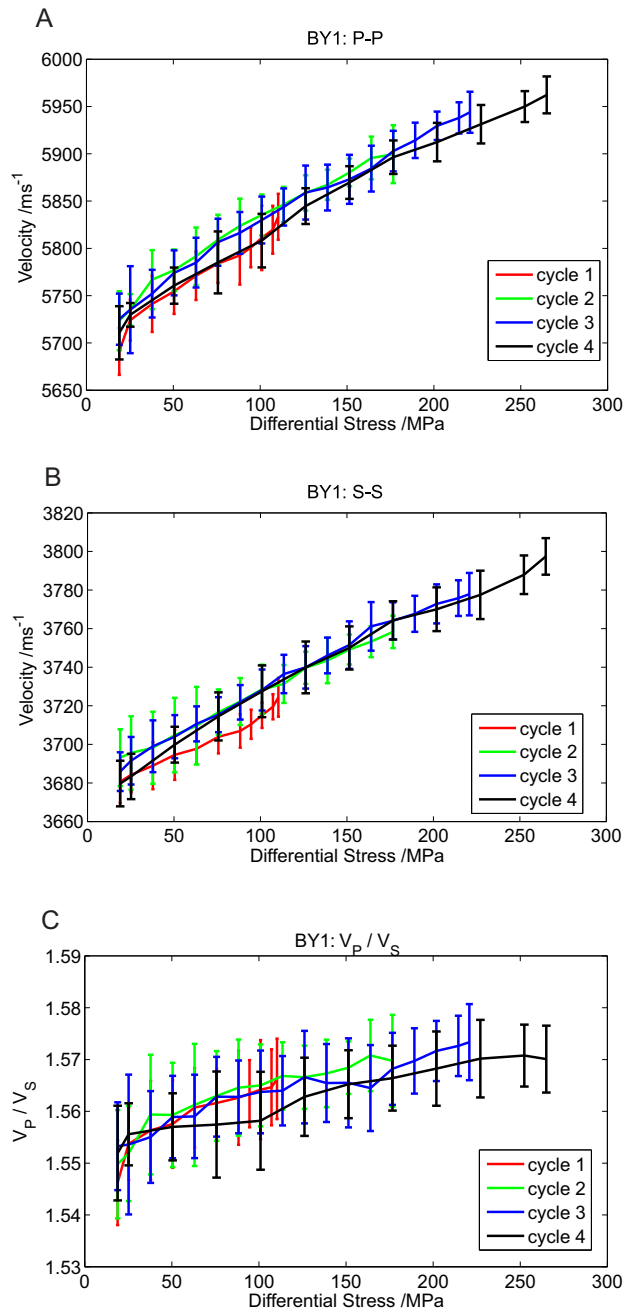
Figure 4.18: A. P-P velocities, B. S-S velocities and C. V_P/V_S ratio through sample BY1 during a cyclic loading experiment.

Sample BY1, cored parallel to the foliation, was subjected to cyclic loading at a confining pressure of 50 MPa. Examples of P-P and S-S traces recorded at a constant load are shown in figure 4.17. In the P-P traces, signals from the first and final cycles appear to arrive later than those from the intermediate cycles. In the S-S cycles, the late arrival from the first cycle is more apparent. This leads to an initial increase in velocity, followed by a decrease in velocity (see figure 4.18). In the P-P traces, the late arrival of the first cycle becomes less apparent in the times of the first minimum and first maximum, whereas the late arrival of the final cycle remains significant (see figure 4.17). In the S-S traces, however, the late arrival of the first cycle remains apparent in the times of initial arrival, first minimum and first maximum. The late arrival of the final cycle is most apparent from the first maximum. The initial decrease in velocity might be due to compaction of the sample or closure of cracks perpendicular to the applied load. Subsequent decreases in velocity are likely due to increased microfracturing with increasing cycles.

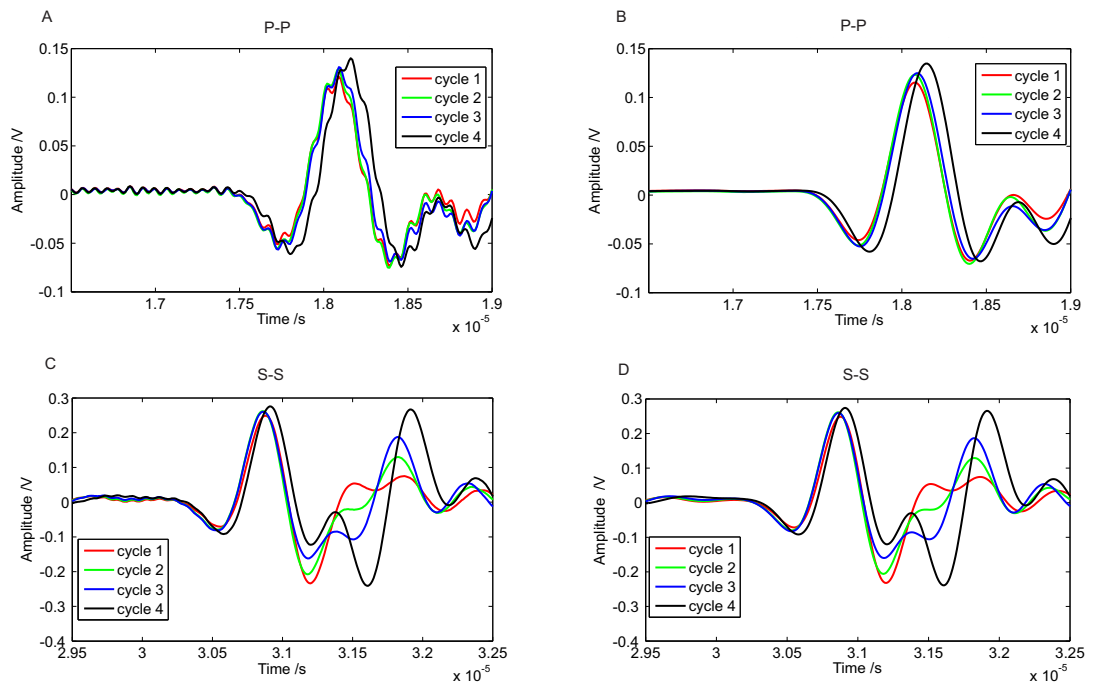## 50 MPa confining pressure: Z Orientation
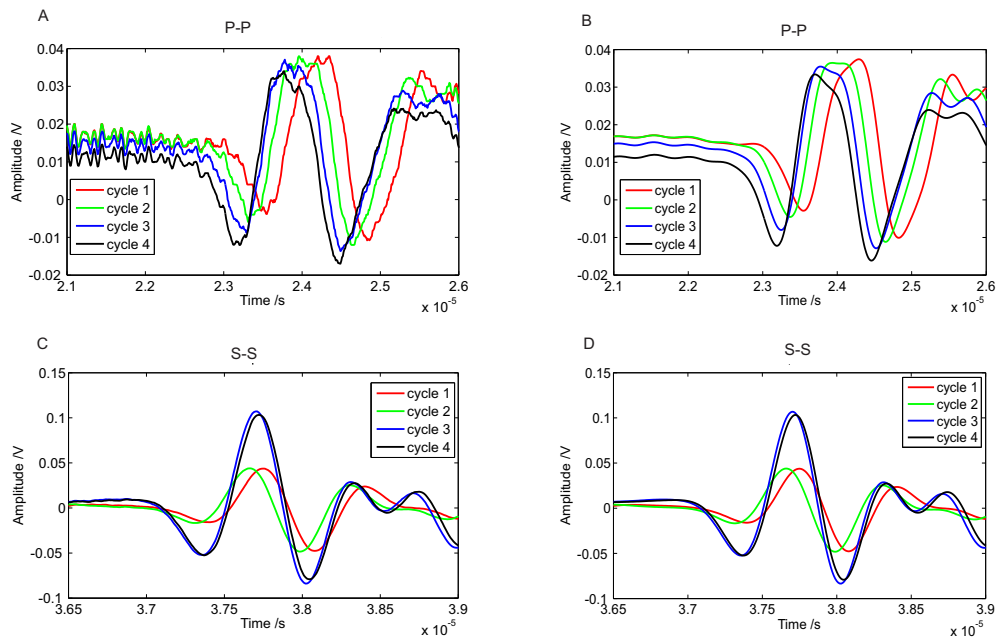
Figure 4.19: A. unfiltered and B. filtered P-P traces recorded through sample BZ3. C. unfiltered and D. filtered S-S traces recorded through sample BZ3. The traces shown are recorded at the same load value, but on successive cycles.

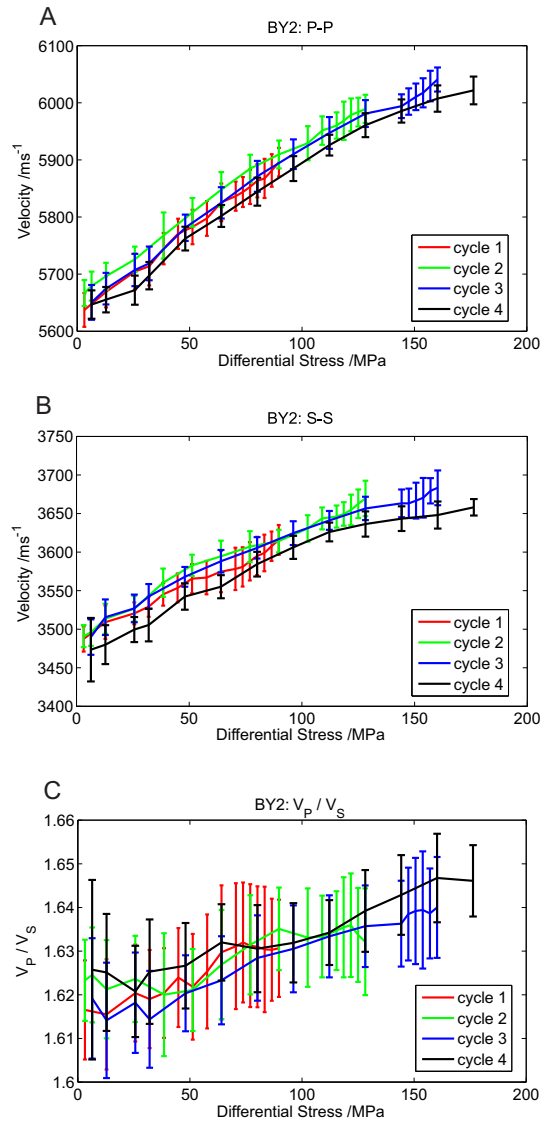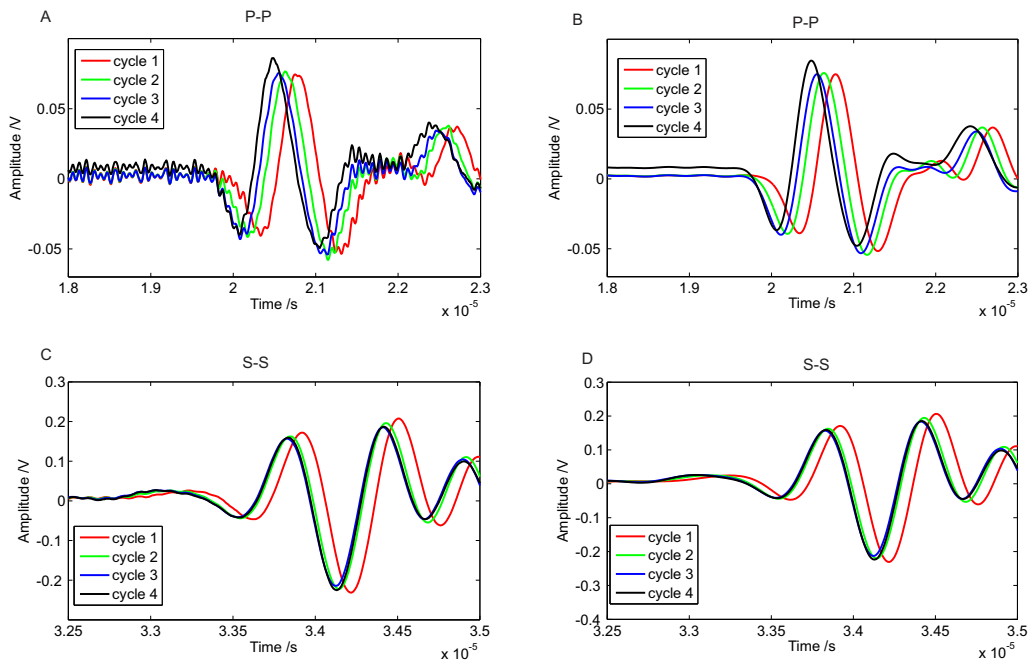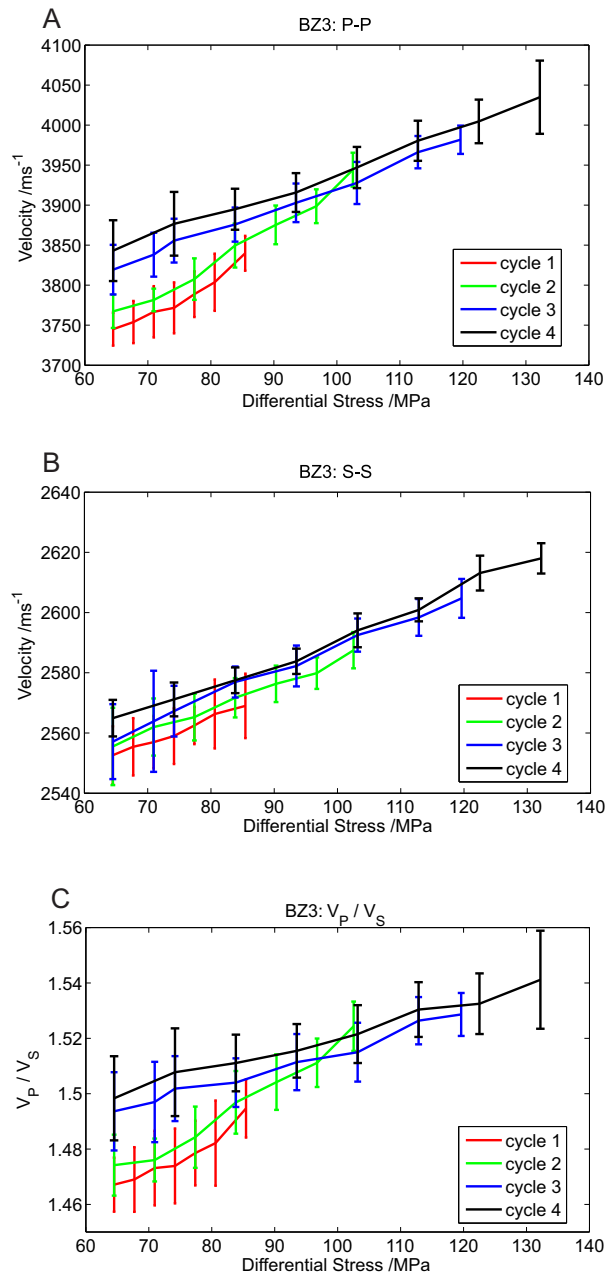Figure 4.20: A. P-P velocities, B. S-S velocities and C. V_P/V_S ratio through sample BZ3 during a cyclic loading experiment.

Sample BZ3, cored perpendicular to the foliation, is subjected to cyclic loading at 50 MPa confining pressure. P-P and S-S- traces recorded at a constant load are shown in figure 4.19. The signals are observed to arrive earlier with increasing cycles. The effect of this is to increase both the P and S velocities with increasing cycles (see figure 4.20). The increasingly early arrival times, and times of the first minimum and first maximum, are shown for P-P and S-S traces in figure 4.19. For the final cycle, a very slight increase in S-S travel-time is observed (i.e. decrease in S velocity). This is most obvious at the first maximum. This progressive increase in velocity with increasing cycles is most likely due to closure of cracks parallel to the foliation, perpendicular to the load applied. The small decrease in S-S velocity on the final cycle may be due to cracks propagating just before sample failure.

4.3.4 Cyclic Confining Pressure Gouge Experiment
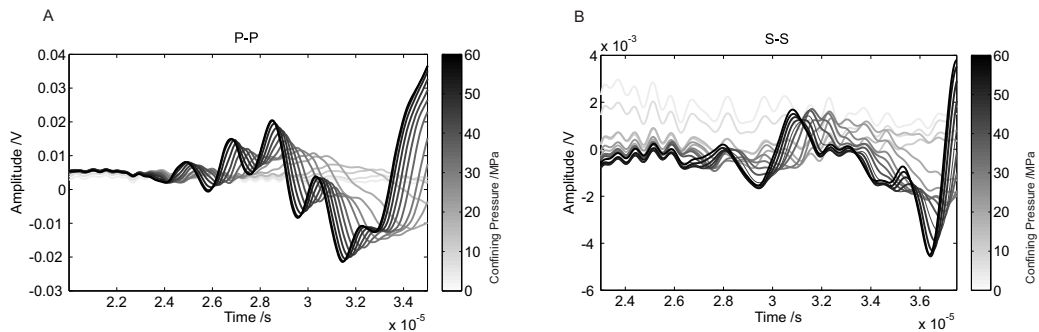
Figure 4.21: A. P-P traces and B. S-S traces through gouge sample MS1z during one cycle of the fault gouge experiment. Darker lines represent traces recorded at higher confining pressures, as indicated by the grey-scale.

A sample of mica-schist fault gouge was subjected to cyclic confining pressure conditions as P-P and S-S velocities were measured. The confining pressure was repeatedly varied from 0 to 60 MPa. With increasing confining pressure the fault gouge sample underwent permanent shortening. However, this change in length of the sample was recorded throughout the experiment, and corrected for in calculating the velocities with increasing cycles. Traces recorded over one cycle are shown in figure 4.21. Traces at fixed confining pressure, on different cycles, are shown in figure 4.22 A and B. The calculated velocities over each cycle are shown in figure 4.22 C and D. Decreases in both P and S velocities are observed in subsequent cycles. It is also interesting to compare the velocities measured through the gouge with those through its protolith. The gouge velocities are slower than the velocities through the mica-schist rock. There is a greater velocity difference between the two orientations of rock samples than between the fault gouge sample used and the slower rock sample. However, it is noted that ve-

56
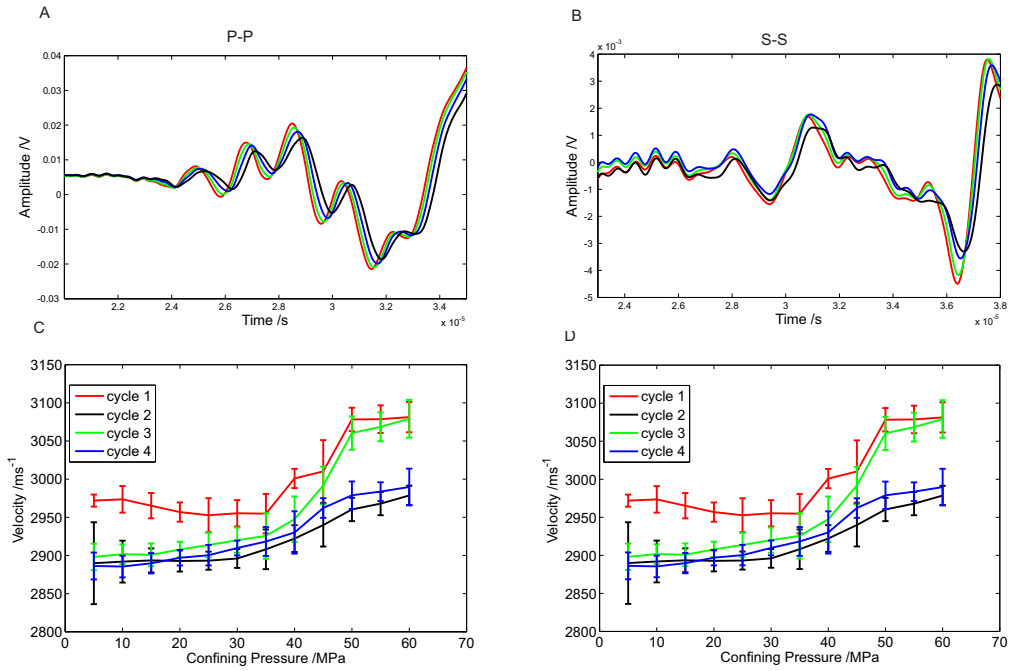
Figure 4.22: A. P-P and B. S-S traces recorded through the fault gouge at constant confining pressure but on different cycles. C. P-P and D. S-S velocities measured through the fault gouge on each cycle.

locities have been measured through only one orientation of fault gouge sample. This sample is from within the plane of the fault, perpendicular to the slip direction. It has foliations running approximately parallel to the length of the sample. The velocities measured correspond to velocities of y-orientation rock samples reduced by 40-50% or z-orientation samples reduced by 10-20%.

4.3.5 Summary of Results

In the uniaxial experiments, both P and S wave velocities were observed to increase with increasing load. This increase in velocity is interpreted as closure of cracks perpendicular to the applied pressure. The greatest changes in velocity were observed in the sample cored perpendicular to the foliation. The velocities measured in the sample cored perpendicular to the foliation were significantly less than those measured in the samples cored parallel to the foliation. In the sample cored perpendicular to the foliation, significant changes in V_P/V_S were also measured, increasing from 1.3 to 1.5 at failure. Perpendicular to this V_P/V_S was measured as 1.5 to 1.55. It is noted that two of the 3 samples failed at approximately the same V_P/V_S ratio. An increase in V_P/V_S ratio can be caused by closure of cracks (e.g. *O'Connell and Budiansky*

57

(1974)). The greatest changes in velocity and V_P/V_S ratio in the sample perpendicular to the foliation suggest that more cracks closed in this orientation.

In the confining pressure experiments, velocities were observed to increase with increasing confining pressures. This can be explained by closure of cracks, in all orientations with increasing confining pressure. Again, significant differences in both the P and S wave velocities are observed in samples of different orientation. Velocities in the slow direction are of the order of 30% less than those in the fast direction. An increase in the V_P/V_S ratio with increasing confining pressure is observed in the sample cored perpendicular to the foliation. However, the V_P/V_S ratio stays relatively constant in the sample cored parallel to the foliation. Again, the greater changes in V_P/V_S ratio in the sample cored perpendicular to the foliation suggest more crack closure in this sample. However, in this experiment, cracks of all orientations are closing. This implies that samples cored perpendicular to the foliation may contain more micro-cracks.

Significant shear wave splitting was observed. The later S wave appears to be of lower amplitude and with a shorter wave-train, suggesting that it may be more attenuated. The velocity of the slower S wave is 35% less than the faster S wave.

In the cyclic loading experiments, velocity changes are observed with increasing cycles. In the samples perpendicular to the foliation (z-orientation), the velocities are observed to increase with increasing cycles. This is the case at both 25 MPa and 50 MPa confining pressure. It appears that the main influence is closure of cracks perpendicular to the applied load (i.e. parallel to the foliation) in increasing cycles. In samples cored parallel to the foliation (y-orientation), decreases in velocity are observed before sample failure. At 25 MPa only very small changes, within picking error, occur in the first 3 cycles. Resolvable changes only occur in the final cycle (relative to the earlier cycles). At 50 MPa, there appears to be a velocity increase following the first cycle and a subsequent velocity decrease on the final cycle. This initial velocity increase may be due to compaction of the sample under these confining pressures, or to closure of cracks perpendicular to the greatest principal stress. The subsequent velocity decrease is interpreted as due to an increase in micro-fracturing before sample failure. Measured velocity changes due to cyclic loading are less than 5% of the original velocity.

With increasing confining pressure the measured velocity through the fault gouge sample increases. Decreases in both P and S velocities are observed in subsequent cycles. It is also interesting to compare the velocities measured through the gouge with those of its protolith. The gouge velocities are slower than the velocities through the mica-schist rock. However, greater differences in velocity are observed between the fast and slow directions in the mica-schist rock, than between the gouge and the slow direction of the rock. However, velocities were measured through only one sample of fault gouge. Other orientations of gouge samples may be slower. Velocities measured through the fault gouge correspond to velocities of y-orientation samples reduced by

40-50% or z-orientation samples reduced by 10-20%.

4.4 Discussion

Throughout the experiments, the foliation in the mica schist is observed to have a strong effect on the measured velocities. Up to confining pressures of at least 80 MPa (equivalent to approximately 3 km depth in the crust), significant differences are observed in the P and S velocities measured parallel and perpendicular to the foliation. The velocities measured perpendicular to the foliation are of the order of 30% less than those measured parallel to the foliation. This strong anisotropy allows us to observe shear wave splitting. Cyclic experiments were carried out to investigate the influence of micro-cracks on the measured velocities. Again, the foliation has a strong influence on the results. For samples perpendicular to the foliation (z orientation), increasing cycles cause an increase in the rock velocity. This can be interpreted as closure of cracks parallel to the foliation (and perpendicular to the applied load) as a dominant influence. For samples parallel to the foliation, increasing cycles cause a decrease in rock velocity, which can be interpreted as micro-cracks opening due to cyclic loading. Velocity changes measured due to cyclic loading are less than 5% of the original velocity.

Gouge velocities are measured to be slower than those through the mica-schist rock samples. A greater difference in velocity is measured between the fast and slow directions in the rock samples than between the fault gouge and the slower rock samples. The measured velocities in the gouge are reduced by 40-50% relative to the y-orientation rock samples or 10-20% relative to the z-orientation rock samples.

Using this dataset, and given the fault zone structure determined by mapping (and summarised in figure 4.2), we can build up an image of the likely velocity structure of the shallow crust in the Carboneras fault zone. It is noted that frequencies used in the laboratory experiments presented are of the order of 1 MHz, whereas frequencies used in seismic investigations are generally < 100 Hz. However, the observed fabric responsible for the anisotropy is pervasive throughout the protolith and so can be expected to cause a velocity anisotropy at seismic frequencies also.

The confining pressures that we have considered represent approximately the upper 3 km of crust. The anastomosing strands of fault gouge will form low velocity structures. As the velocity of the fault gouge appears to increase with confining pressure more slowly than the velocity of the mica-schist rock, the velocity contrast between rock and gouge may increase with depth. Whether the foliation in the rock is vertical, horizontal or dipping when in association with the gouge may also influence the velocity contrast (see figure 4.23). If the orientation of the foliation changes along the strike of the fault, the velocity contrast may also change. Relatively quick changes in the orientation of the foliation due to, for example, folding could conceivably also influence seismic images. Depending on the raypath geometry, this could potentially result in apparent widening

of the fault strand in seismic images (e.g. see figure 4.24). Seismic investigations that sample along strike of the fault may find a different apparent thickness of low velocity fault core than those that aim to image a transect across the fault (e.g. see figure 4.24). For foliations that are vertical near a fault strand and shallow laterally away from the fault, the greatest velocity contrast could potentially be due to the change in orientation of the foliation, rather than due to the strand of fault gouge within the rock, (e.g. for an investigation across the fault, see figure 4.24). If the foliation is approximately parallel to the strike of the fault (whether or not it is dipping or vertical), seismic investigations that sample along the fault (e.g. fault zone guided wave experiment) will be sensitive to the velocity contrast between gouge and the fast direction in the rock (see figure 4.24). The effects of the velocity anisotropy may also depend on the length scales and frequencies considered, and so this potential influence needs to be determined for specific source-receiver geometries and the local geological fabric in the locations of seismic experiments.

Strong fracturing within mica-schist rock, as observed close to the fault strands, would be expected to cause a decrease in the rock velocity (see figure 4.23), and in the velocity contrast between the rock and the gouge. We have shown velocity changes of less than 5% in cyclic loading experiments. However, changes in velocity due to fracturing may be greater in the field as macrofractures would also be expected. Alteration and fluid content may also have an influence.

Throughout these experiments, the strong influence of the foliation of the mica schist on velocities measured has been shown. The influence of the mica-schist foliation should be carefully considered in seismic investigations of the fault zone.

4.5 Conclusions

Samples of mica-schist rock and fault gouge were collected from the Carboneras fault zone, SE Spain. Ultrasonic velocities of these samples were investigated under a range of confining pressures. Cyclic loading also allowed us to investigate the influence of microcracks on measured velocities. The foliation in the mica schist was observed to have a strong influence on the velocities. Much faster velocities were measured in samples cored parallel to the foliation than those perpendicular. Shear wave splitting was also observed. Gouge velocities were slower than those through mica-schist rock. However, greater differences in velocity are observed between the fast and slow directions in the mica-schist rock, than between the gouge and the slow direction of the rock. The potential influence of this on seismic studies is discussed. The importance of considering the orientation (or potential range of orientations) of the foliation in interpretation of seismic experiments of the fault zone is emphasised.
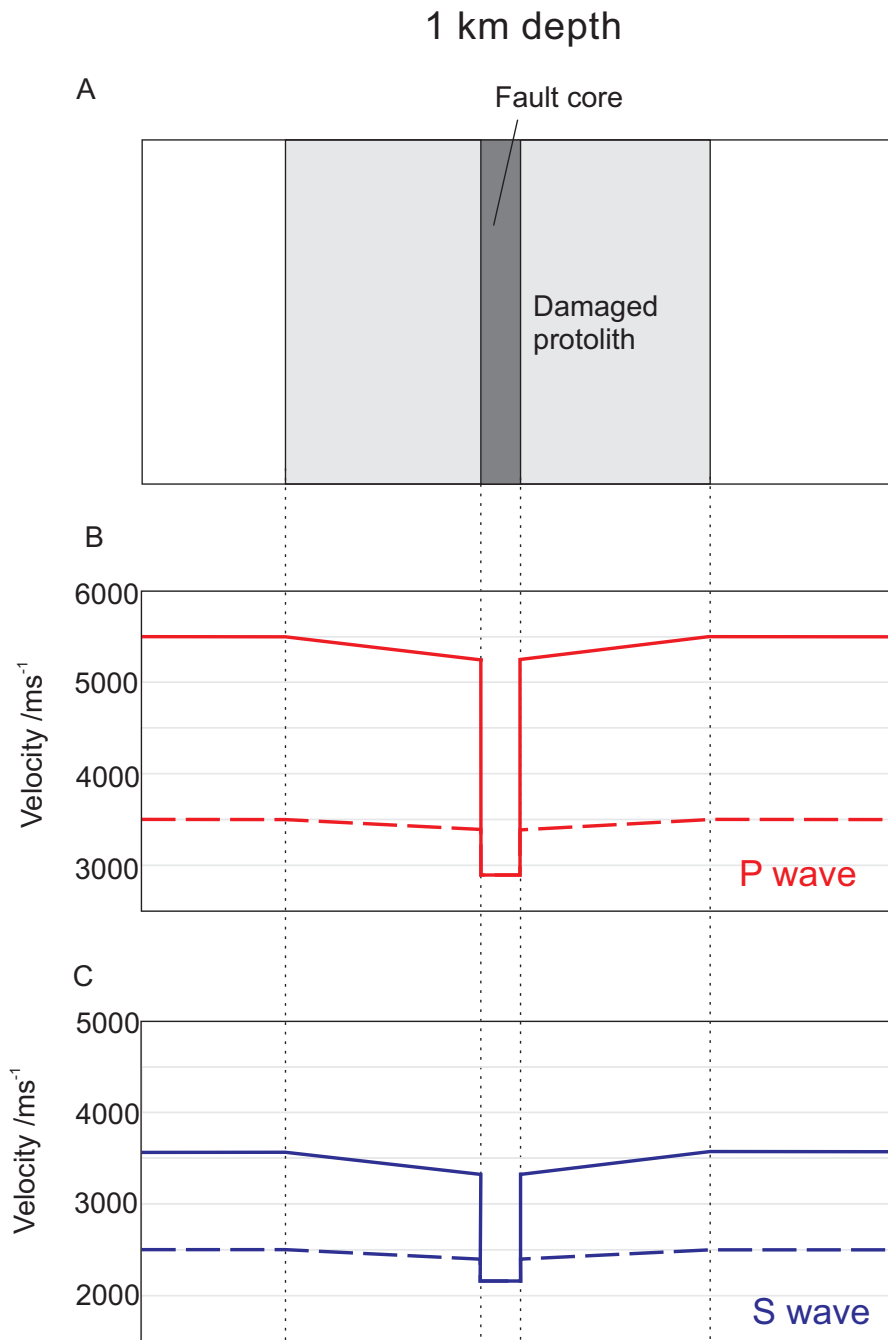
Figure 4.23: For a single fault strand surrounded by damaged protolith (as shown schematically in A.), the range of B. P-wave and C. S-wave velocity contrasts are shown. The slower mica-schist rock velocities are indicated by the dashed lines and the faster velocities with solid lines. A large difference in velocity contrast between the rock and the gouge is seen, depending on the orientation of the foliation. In the area of damaged protolith near the fault core the velocities are reduced. However, the dominant factor remains the orientation of the foliation. Values shown are from experiments at 25 MPa (equivalent to approximately 1 km depth).
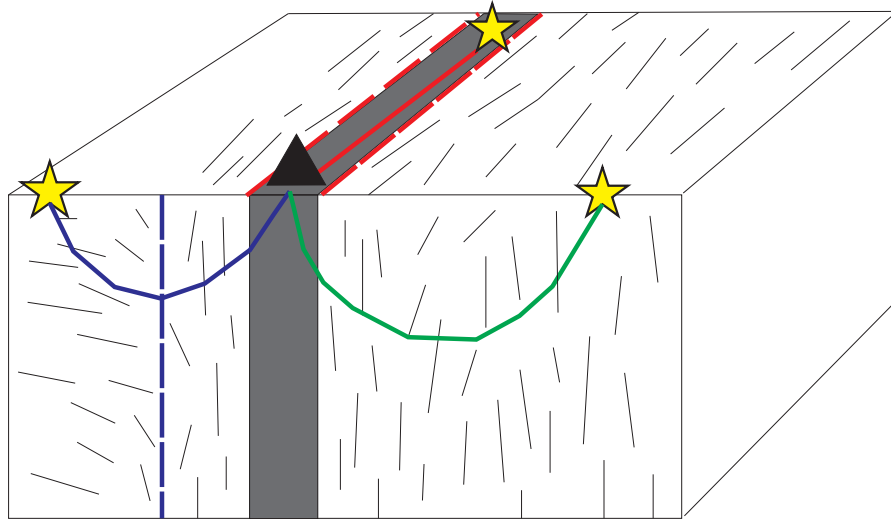
Figure 4.24: Schematic diagram illustrating how the raypath geometry and the geological fabric may influence the apparent width of the fault zone. Sources and a receiver are represented by stars and a triangle respectively. A strand of fault gouge is shown in grey. The geological fabric surrounding this is also indicated. In this example, the foliation is approximately parallel to the strike of the fault strand and close to the fault core the foliation is vertical, but on one side shallows laterally away from the fault core. The solid red line indicate a ray travelling along the fault core. In this experimental set-up, the observed velocity contrast would be expected to be between the gouge and the fast rock direction (parallel to the foliation). The apparent fault zone width is indicated by the dashed red lines. The solid blue line indicates a ray travelling across a transect of the fault, where the foliation changes from dipping to vertical. The greatest change in velocity would be expected to be between the areas of dipping and vertical foliation, as indicated by the blue dashed line. The green solid line represents a ray that samples gouge and rock with vertical foliation. A small change in velocity associated with the contact between the gouge and slower rock direction may be resolved.

Chapter 5

Crustal structure of the Carboneras Fault region from ambient noise analysis

Contributions

This chapter is based on collaborative work with Nick Harmon, Univeristy of Southampton. Many of the main scripts used in processing of data were adapted from scripts by Nick Harmon. Scripts were adapted from previous use with a larger scale seismic network in order to be more flexible for different networks. Pre- and post-processing scripts were written to complement the adapted processing scripts.

5.1 Introduction

The Carboneras fault zone area is a geologically varied region, with a complex geological history. The region has been affected by a mixture of compressional and extensional tectonics, leading to uplift of basement rocks and development of sedimentary basins. The area has also been strongly affected by faulting and folding and has experienced two volcanic episodes. Although some of the faults in the area are still active, a relatively low level of seismicity occurs. The area has previously been mapped and studied at the surface, but the structure at depth is still unknown. There is some debate about the depth extent of faulting in the region and the depth extents of sedimentary basins and volcanic rocks are not well constrained. In order to develop a better understanding of the crustal structure of this geologically complex area, the seismic noise distribution of the area has been investigated and a surface wave velocity tomography model developed based on ambient noise. The geological history of the region is discussed, along with theory and background to ambient noise tomography. Noise characteristics are then investigated and a velocity model is developed and discussed in terms of the geology of the area. Possible implications of strong anisotropy in crustal rocks are discussed in terms of seismically imaging the area.

5.1.1 Carboneras region, SE Spain

The Carboneras Fault is a major transpressive sinistral strike-slip fault in SE Spain. It is part of the Trans-Alboran shear zone, a network of faults which form part of the diffuse plate boundary between Africa and Iberia. It passes close to the town of Carboneras at its north-eastern extent, where it links to or is terminated by the North-South striking Palomares fault. The Carboneras fault strikes to the southwest, towards Almeria, and continues offshore in the Alboran Sea (see figure 5.1).
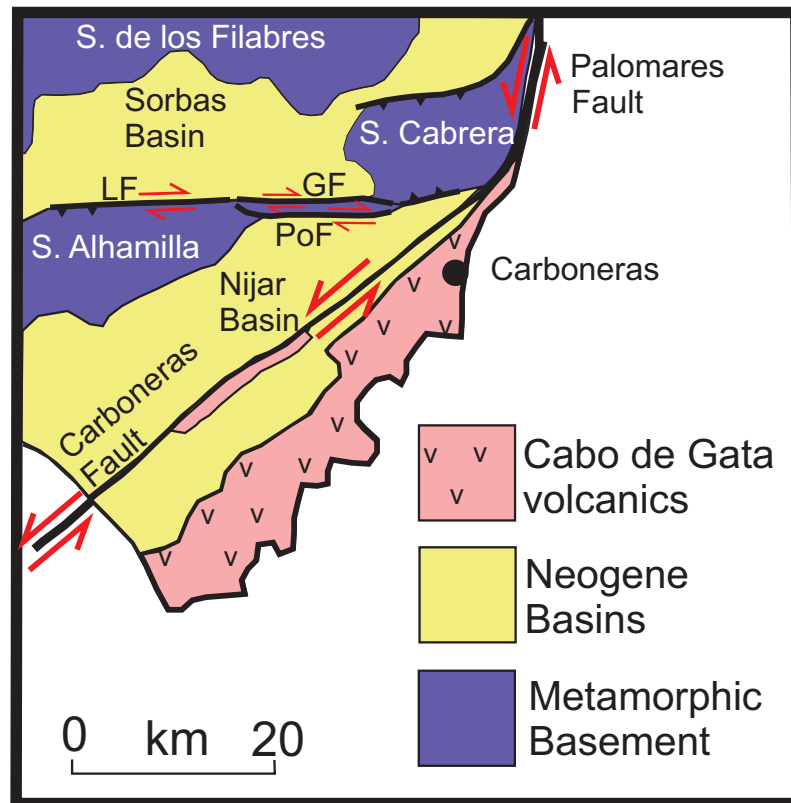
Figure 5.1: Geological summary of the area around the Carboneras fault zone. To the north of the Carboneras fault zone, mountains (Sierras) of metamorphic basement are observed. Sedimentary basins occur between these mountains. To the south of the Carboneras fault is the Cabo de Gata volcanic region. Faults in the region are shown as thick black lines. The Carboneras fault is a left-lateral strike slip fault, as is the Palomares fault. Other major fault zones in the area occur to the north of the Sierra Cabrera, to the south of the Sierra Cabrera and to the north of the Sierra Alhamilla (the Lucainena Fault (LF), the Gafarillos Fault (GF) and the Polopos fault (PoF)). Figure dapted from *Rutter et al.* (2012).

The geology of the surrounding region is widely varied (see figure 5.1). To the north of the fault, a basin-and-range topography is seen, with mountains (sierras) composed of uplifted metamorphic basement rocks. Intermontane basins onlap onto the metamorphic basements, and are often bounded by strike-slip faults. To the south of the Carboneras fault, in the Cabo de Gata region, the geology is dominated by

volcanic rocks, which are mainly calc-alkaline in composition.

The metamorphic basement rocks in the region include three major tectonic complexes, with different degrees of metamorphism. In ascending order (and decreasing metamorphic grade) these units are the Nevado Filabride complex, the Alpujarride complex and the Malaguide complex (*Egeler and Simon*, 1969; *Torres-Roldán*, 1979). These complexes are juxtaposed by extensional shear zones, so that where two units are in contact with each other, abrupt changes in metamorphic grade are observed. This NE-SW extensional activity occurred from Palaeogene to early Miocene, at the same time as NW-SE shortening due to convergence between Africa and Iberia (e.g. *Frizon de Lamotte* (1987); *García-Dueñas et al.* (1988); *Platt and Vissers* (1989)). These uplifted metamorphic rocks today compose the mountains in the region. Within the study area the main mountains are the Sierra Cabrera, the Sierra Alhamilla and the Sierra de los Filabres (see figure 5.1). In the Sierra Cabrera and Sierra Alhamilla both the Nevado Filabride and the Alpujarride complex are exposed, and the Malaguide complex appears in patches. In the Sierra de los Filabres, only the Nevado Filabride complex is exposed.

The intermontane basins of the study area (the Nijar basin and the Sorbas basin) both onlap the metamorphic rocks at the northern basin margins, and are bounded by strike-slip faults at the southern margins (see figure 5.1). These basins have a common sedimentary evolution, characterised by three main sequences which are separated by unconformities of regional significance (*Weijermars et al.*, 1985). The lower (Upper Serravalian-Lower Tortonian) and upper sequences (Upper Tortonian-Upper Messinian) consist of continental clastic sedimentary rocks. The intermediate sequence (Upper Tortonian-Upper Messinian) is made up of marine sedimentary rocks. The first and fastest stage of basin development has been interpreted to record rapid extensional tectonics, as the metamorphic units were uplifted. The intermediate sequence represents a short marine inundation which may have been caused by subsidence due to the stretching of the crust. Continued convergence of Africa and Iberia allowed further emergence, which caused the connection to the sea to become precarious, causing thick deposits of evaporites. Eventually, continued convergence and uplift caused a return to continental conditions (*Rodríguez-Fernández et al.*, 2012). The basins are believed to have formed in the hanging walls of major extensional faults that were also responsible for the exhumation of the metamorphic units (e.g. *Martínez-Martínez and Azañon* (1997); *Meijninger and Vissers* (2006); *Rodríguez-Fernández and Sanz de Galdeano* (2006)). In late Tortonian-Early Messinian times, a change in the Africa-Europe convergence direction produced E-W trending compressional folds, NW-SE oriented high-angle normal faults and E-W and NE-SW trending strike-slip faults (*Dewey et al.*, 1989). Such structures have affected the basins and their basements in a complex manner. Strike-slip faults have strongly deformed some of the basin edges, obliterating the

previous extensional structures (e.g. *Rodríguez-Fernández et al.* (2012)).

The main fault in the study area is the Carboneras fault. This NE-SW trending left-lateral strike-slip fault has been active from upper Miocene to recent times. The total offset on this fault may be as much as 40 km, but is at least 15 km (*Rutter et al.*, 2012). The Carboneras fault has been interpreted as a stretching transform fault, with material to the NW of the fault having been stretched, and material to the SE of the fault forming a relatively rigid block (*Rutter et al.*, 2012). The Carboneras fault, along with other left-lateral faults in the region, may form the southern boundary of the stretched Betic-Alboran wedge (*Gutscher*, 2012). The fault running along the northern boundary of the Sierra Alhamilla is the dextral Lucainena fault (*Sanz de Galdeano*, 1989). To the east, the Lucainena fault branches into the Gafarillos fault and the Polopos fault (or North Gafarillos fault and South Gafarillos fault respectively) (*Stapel et al.*, 1996; *Huibregtse et al.*, 1998; *Jonk and Biermann*, 2002; *Gianconia et al.*, 2012). The Gafarillos fault cuts the upper Tortonian sediments and the metamorphic rocks of the Sierra Cabrera (*Sanz de Galdeano*, 1989) and the Polopos fault continues to the south of the Sierra Cabrera (see figure 5.1, *Gianconia et al.* (2012)). Some authors have suggested that this set of faults are conjugate to the Carboneras fault zone (*Stapel et al.*, 1996; *Booth-Rea et al.*, 2003). More recently, it has been suggested that these faults developed in the early Miocene, as part of the extensional faulting activity, and were perhaps reactivated during the Upper Miocene activity on the Carboneras fault zone (*Rutter et al.*, 2012). South-dipping reverse faults form the north edge of the Sierra Cabrera (*Booth-Rea et al.*, 2004) and north-dipping reverse faults form the southern edge (*Keller et al.*, 1995).

To the South of the Carboneras fault, the volcanic rocks of the Cabo de Gata series include extrusive lavas and a range of volcaniclastic rocks. Age determinations and stratigraphic relations show that the volcanic rocks form two groups. An older group formed between 20-13 Ma and before the Carboneras fault was active (e.g. *Serrano* (1990a,b); *Scotney et al.* (2000); *Rutter et al.* (2012)). In places, these are tilted towards the vertical against the Carboneras Fault Zone. A younger, unconformable group formed between 13-6 Ma, during the time of main activity on the Carboneras Fault Zone (*Serrano and Gonzales Donoso*, 1989; *Uwe et al.*, 2003; *Rutter et al.*, 2012). Two large elongate intrusive bodies, of several kilometres in length, as well as many thin andesitic dykes, are present within the fault zone itself. The fault zone may have acted as a conduit to bring intrusive rocks to the surface. It has been inferred that eruptive centres may have developed along the trace of Carboneras Fault Zone, but that any surface edifices have since been removed (*Rutter et al.*, 2012).

The area has previously been mapped and studied at the surface, but the structure at depth is still unknown. There is some debate about the depth extent of faulting in the region, and the depth extents of the sedimentary basins, and volcanic rocks are not

well constrained. In this region with a low to moderate level of seismicity, we attempt to address some of the uncertainties though ambient noise analysis of the region.

5.1.2 Seismic Interferometry

Theory

It has been shown theoretically (e.g. *Weaver and Lobkis* (2001); *Wapenaar* (2004)) and verified by observation (e.g. *Shapiro and Campillo* (2004)) that cross-correlation of diffuse wavefields (e.g. ambient noise) between two stations approximates to the Green's function between those two stations.
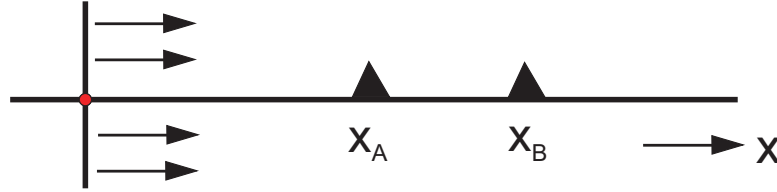
Figure 5.2: Schematic illustration of a source propagating towards two stations at X_A and X_B. Cross correlating the signal from the station at X_A with that from the station at X_B will give the Green's function between the two stations.

Considering the one-dimensional case (see figure 5.2), the response of a station at x_A to an impulsive source at position x_S is $G(x_A, x_S, t)$, the Green's function between x_A and x_S in the time (t) domain. For an impulsive source travelling at constant velocity c, this response will be an impulse at t_A, i.e. $\delta(t - t_A)$ where $t_A = (x_A - x_S)/c$. Therefore,

$$G(x_A, x_S, t) = \delta(t - t_A) \tag{5.1}$$

where $\delta(t)$ is the Dirac delta function. Similarly, the response of a staion at x_B to the same source will be $G(x_B, x_S, t)$ and will be equal to $\delta(t - t_B)$ with $t_B = (x_B - x_S)/c$. The cross-correlation of the responses at x_A and x_B is defined as

$$G(x_A, x_S, t) * G(x_A, x_S, t) = \int G(x_B, x_S, t + t')G(x_A, x_S, t')dt'. \tag{5.2}$$

For an impulsive source this can be written as

$$\int \delta(t + t' - t_B)\delta(t' - t_A)dt' = \delta(t - (t_B - t_A)) = \delta(t - (x_B - x_A)/c). \tag{5.3}$$

This is an impulse at time $(x_B - x_A)/c$, which can be interpreted as the response at x_B if the source was at x_A (i.e. the Green's function $G(x_B, x_A, t)$). The traveltime along the common path (x_S to x_A) cancels in the cross-correlation process, leaving the traveltime along the remaining path from x_A to x_B. Thus it can be written:

$$G(x_B, x_A, t) = G(x_B, x_S, t) * G(x_A, x_S, t) \tag{5.4}$$

i.e. the cross-correlation between the two stations at x_A and x_B is equal to the Green's function between the two stations.

For a source travelling in the opposite direction, the cross-correlation will be equal to the response at x_A for a source at x_B. If there are two sources, from different directions, the cross-correlation will result in a two-sided function, with a positive (causal) lag and a negative (acausal) lag. If the source function is a wavelet instead of an impulse, then the cross-correlation of the responses at the two stations gives the Green's function between these two stations, convolved with the auto-correlation of the source function. This principle holds for any source time function, including noise. In the case of impulsive or transient sources, the responses must be cross-correlated separately, after which a summation over the sources takes place. In the case of uncorrelated noise sources, a single cross-correlation suffices.

This can also be considered in two or three dimensions (see figure 5.3). For two stations (e.g. seismometers) surrounded by energy sources, the wavefield from each source propagates into the medium and is recorded at both receivers. On cross-correlation, the energy that travels along the path between the stations will add constructively, whereas energy that did not travel along this path will add destructively. Hence, the resulting signal will approximate to the Green's function between the stations. Because the sources have a finite frequency content, not only do the sources exactly in line with the path between the receivers (at 0 and 180 degrees) contribute to the signal, but also the sources in the Fresnel zones around these angles. The events in all traces outside of the Fresnel zone are expected to interfere destructively and give no coherent contribution to signal. For a 3D source distribution, all sources in Fresnel volumes, rather than Fresnel zones, contribute to the retrieval of the Green's function between the stations.
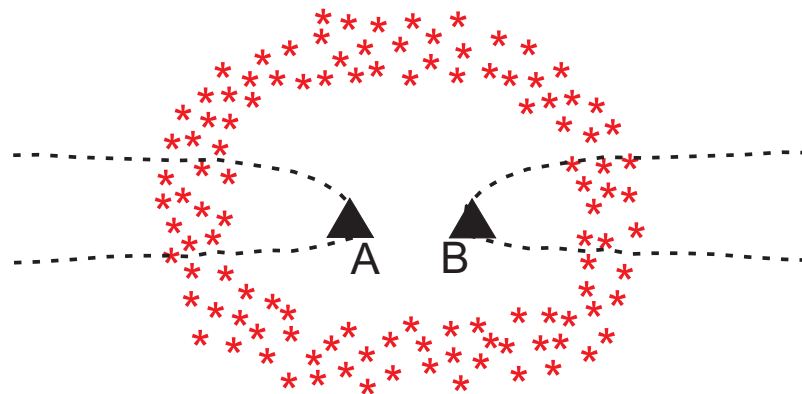
Figure 5.3: A 2D distribution of noise sources surrounding two stations A and B. Cross-correlating the signal at station A with that at station B will return the Green's function between the two stations. The noise sources which contribute to the cross-correlation fall within the Fresnel zone, approximated here by the dashed line.

Ambient Noise

The first seismological demonstrations of seismic interferometry were by *Campillo and Paul* (2003), *Shapiro and Campillo* (2004) and *Sabra et al.* (2005a) who showed that cross-correlation of ambient seismic noise between seismometers approximates to the Green's function between the two seimometers. Sources of ambient seismic noise include primary and secondary oceanic microseismic noise (around 12-14 s and 6-8 s respectively), wind (0.01-2 s), anthropogenic noise (0.1-1 s, with characteristic frequencies depending on the source), and micro-seismic events (< 1 s).

Correct reconstruction of the Green's functions requires diffuse fields (*Lobkis and Weaver*, 2001), isotropic noise source distribution (e.g. *Snieder* (2004); *Roux et al.* (2005)) or isotropic incidence of wavefields (*Nakahara*, 2006). However, studies show that the actual distribution of ambient noise energy is not isotropic, and varies temporally (*Stehly et al.*, 2006; *Yang and Ritzwoller*, 2008a; *Yao et al.*, 2009). As a consequence, the determined empirical Green's function (EGF) may be an incomplete reconstruction of the true Green's function. This may be apparent in asymmetry of the EGF between two receivers (e.g. *Yao et al.* (2006)). An uneven distribution of noise sources can produce a bias in the surface wave velocities measured from the EGF, whereas in the case of a spatially homogeneous distribution of noise sources or diffuse wavefields, we would expect accurate traveltime measurements. Although the distribution of ambient noise is not isotropic, the use of long time periods (e.g. 1 year) and the presence of multiple scatterers in the crust will allow the azimuthal distribution of noise sources to homogenise (*Campillo and Paul*, 2003; *Yang and Ritzwoller*, 2008a). Temporal whitening of data can also make the distribution of noise sources more isotropic. Comparisons of phase velocities from ambient noise interferometry and traditional two-station analysis (*Yao et al.*, 2008) and of phase-velocity maps from ambient-noise tomography and teleseismic surface-wave tomography (*Yang and Ritzwoller*, 2008b), as well as numerical simulations for certain types of noise distribution (*Lin et al.*, 2008; *Yang and Ritzwoller*, 2008a), indicate that the bias is, indeed, small when these steps are taken.

Surface Wave Tomography

Surface waves are dispersive. Longer periods have a longer wavelength and penetrate deeper into the earth. As seismic velocity generally increases with depth in the crust, the longer period waves generally travel faster. Since different periods are sensitive to properties at different depths, the surface-wave dispersion can tell us about how seismic velocity varies with depth in the crust (e.g. *Dwiewonski et al.* (1969, 1972)). For EGFs from many station pairs, at a particular period we can determine the velocities along different raypaths and can therefore apply a tomographic reconstruction in order to determine the velocity structure at that period. This can be repeated for different

periods, and with knowledge of the depth sensitivity at each period, the velocity structure at depth can be determined. The first applications of seismic interferometry for surface wave tomography were by *Shapiro et al.* (2005) and *Sabra et al.* (2005b). The tomographic maps of California that they produced agree well with surface geology and previous seismic studies in the region. Passive seismic interferometry does not require earthquakes. Therefore, the raypaths available for the tomographic inversion, and the achievable resolution, depend primarily on the geometry of the seismic network. This means that this technique is particularly useful in relatively aseismic areas (e.g. *Nicolson et al.* (2012)).

Ambient noise interferometry has also been used to monitor velocity changes in volcanoes correlated with volcanic events (*Duputel et al.*, 2009; *Brenguier et al.*, 2008a) and velocity decreases at the time of earthquakes (*Minato et al.*, 2012; *Brenguier et al.*, 2008b).

5.2 Data

In the current study of the Carboneras Fault region, data used are from the Carboneras Fault Experiment (CAFE) network. This was a temporary network deployed by the University of Liverpool, with SEISUK, and was in operation for one year from February 2010 -February 2011 (see figure 5.4). This network of 24 stations included 10 broadband seismometers in a regional network layout, and two transects of ESPD and 6TD instruments perpendicular to the Carboneras fault. The transects were near the villages of Sopalmo and El Saltador and included 9 (3 EPSD an 6 6TD) and 5 (3 EPSD and 2 6TD) stations respectively. The seismometers recorded continuously with a sampling rate of 100 sps. Instruments were buried at shallow depths where possible, though stations AGUA, LPNR and RODA were deployed sub-aerially.

5.3 Determining Noise Characteristics

Approximately a year of data from all 24 stations of the CAFE network are cross-correlated. To perform the cross-correlation, the data from each station is first split into individual day-long files. The daily trend and mean are removed from the raw signals. Each day-long file is then bandpass filtered between 0.025 and 10 Hz. Temporal normalisation is applied, using a moving average filter as described by *Bensen et al.* (2007). This is to remove unwanted earthquake signals and instrument irregularities. Cross-correlations are then calculated between all possible station pairs on all available dates. The determined noise correlation functions (NCFs) are shown in figure 5.5. Each of these cross-correlations approximate to the Green's functions between a pair of stations. A clear move-out is observed in both the causal and acausal component. The signals are observed to be relatively symmetric, though some variations between
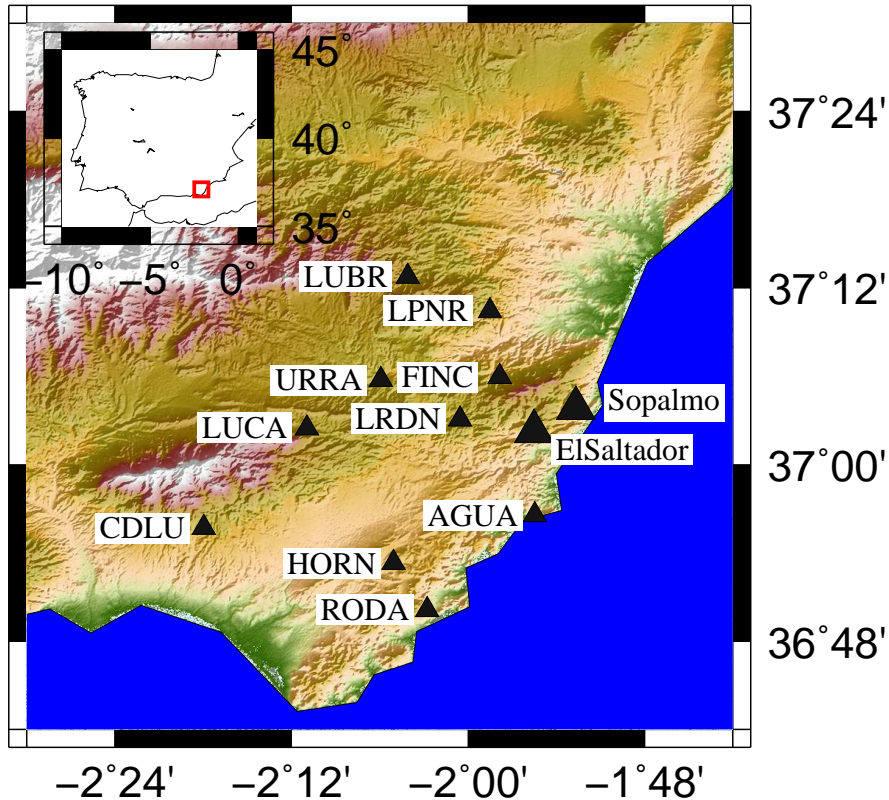
Figure 5.4: Station map for the CAFE network. Ten instruments are in a regional network layout. The remaining fourteen seismometers are deployed in two transects (at Sopalmo and El Saltador) crossing the Carboneras fault.

the two components are clear. This may represent non-uniform distribution of noise sources. For the station pairs with close station spacing (i.e. our transects across the fault), a spike at zero lag time is observed. This suggests that there is a noise source perpendicular to these station pairs.

The distribution of the sources are then calculated from these NCFs. For each NCF the power at the period of interest is determined for both the causal and acausal components, by calculating the frequency transform. This power in the frequency domain at a particular period is then plotted at the relevant azimuth for this station pair. The azimuthal variation in the power of noise sources for periods of 0.1, 0.5, 1, 3, and 5 seconds is shown in figure 5.6. Generally, a relatively isotropic distribution of noise sources is seen, at a particular period. At shorter periods, the amplitude of the noise sources is less.

5.4 Shear Velocity Inversion

The group velocity as a function of period can be measured using frequency-time analysis (e.g. *Bensen et al.* (2007)). For our analysis, we use the symmetric component, i.e. the average of the causal and acausal components of the NCFs. For each NCF,

71
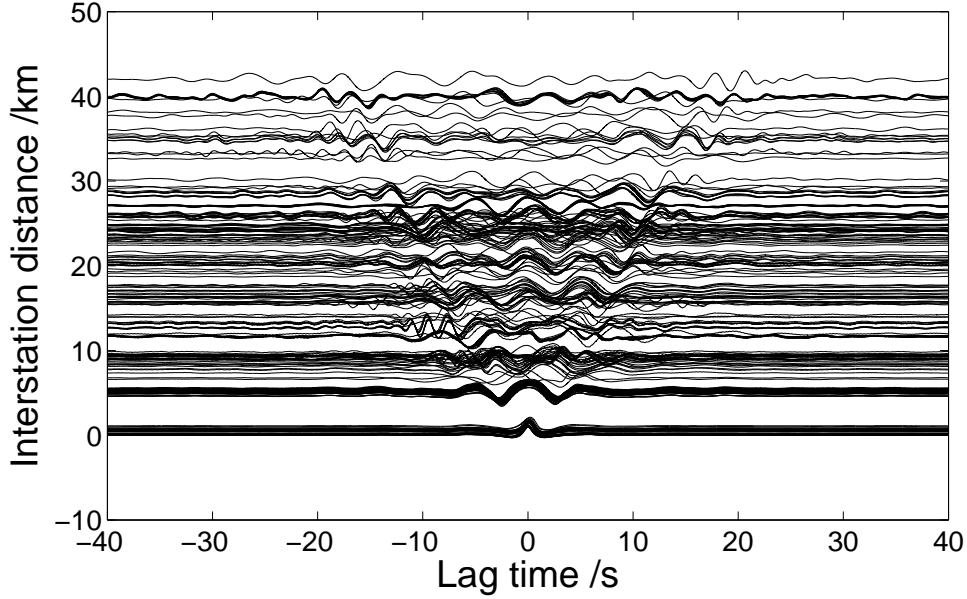
Figure 5.5: Noise correlation functions from a year of data from the CAFE network. Each of these cross-correlations approximate to the Green's function between a pair of stations.

using a set of narrow bandpass filters, a spectrogram is generated (e.g. figure 5.7). Periods of 0.7 to 5 seconds are used. At each period of interest, group velocities are determined from the maximum of the power. Error in the group velocity pick is scaled to the width of region with 99% of the maximum power, and each dispersion curve fit is checked manually.

A dispersion curve representing the whole region is calculated as the average of all the dispersion curves, weighted by the inter-station path length of each. Each period is sensitive to a range of depths, described by the sensitivity kernels. Therefore, for a particular velocity-depth model, the resulting dispersion curve can be calculated, with knowledge of the sensitivity kernels (see figure 5.8). A velocity-depth profile representing the region is searched for. The model is required to produce a dispersion curve that agrees with the average dispersion curve for the region. An inversion is applied to perturb the velocity model to produce a better fit to the average dispersion curve. A damped iterative least-squares approach is used (*Tarantola and Valette*, 1982),

$$\Delta m_{i+1} = (G^T C_{nn}^{-1} G + C_{mm}^{-1})^{-1} [G^T C_{nn}^{-1} \Delta d + C_{mm}^{-1} (m_i - m_0)] \tag{5.5}$$

where m_0 is the starting model, Δm_i is the change to the shear velocity model at iteration i, G is the matrix of group velocity sensitivity kernels, C_{nn} is the data covariance matrix, C_{mm} is the a priori model covariance matrix and Δd is the difference between the observed and predicted group dispersion. The velocity model is required to remain stable under inversion, and produce a good fit to the average dispersion curve.
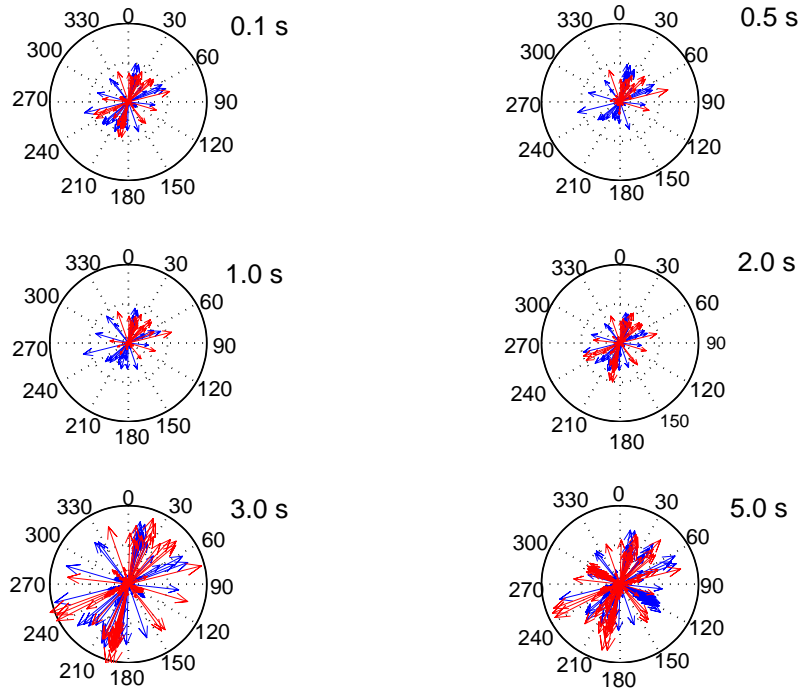
Figure 5.6: The determined noise distribution for sources of periods 0.1, 0.5, 1.0, 2.0, 3.0 and 5.0 seconds. The red arrows represent noise sources determined from the causal components of noise correlation functions, and the blue arrows those from the acausal components. The length of each arrow represents the relative amplitude of each noise source.

Group velocity sensitivity kernels are calculated using DISPER80 (*Saito*, 1988).

At each period, group velocity maps are determined from velocities from all available station pairs, using a fat ray approach. At each spatial co-ordinate, information from velocity maps of all periods is combined and this dispersion information is inverted to obtain a 3D shear velocity model using a damped iterative least-squares approach described above (*Tarantola and Valette*, 1982). The determined average velocity-depth profile is used as a starting model.

Resolution tests are also performed. Checkerboard tests with different sizes of squares are carried out to test the ability of the array to resolve features of different sizes. Raypath plots for a number of different periods are also shown.
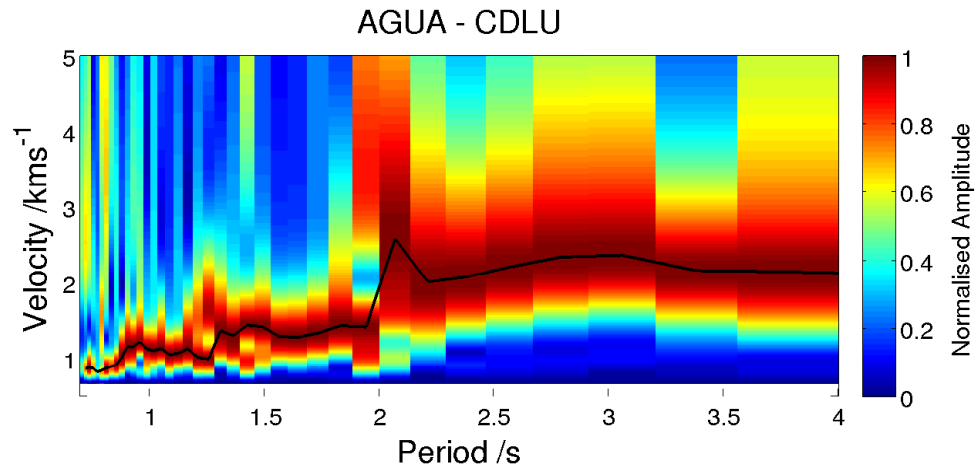
Figure 5.7: Spectrogram determined from the noise correlation between stations AGUA and CDLU (see figure 5.4). The colour scale represents the normalised amplitude of the signal. The black line shows the ridge of the spectrogram.

5.5 Results

The 1D velocity model to fit the average dispersion curve is shown in figure 5.8. Sensitivity kernels show that depths of up to approximately 12 km are sampled, though the greatest sensitivity is to approximately 4 km (figure 5.9A). The 1D model consists of a shallow low-velocity layer that overlies a crust of shear velocity 3.1 km/s. This is the starting model used in the three dimensional inversion.
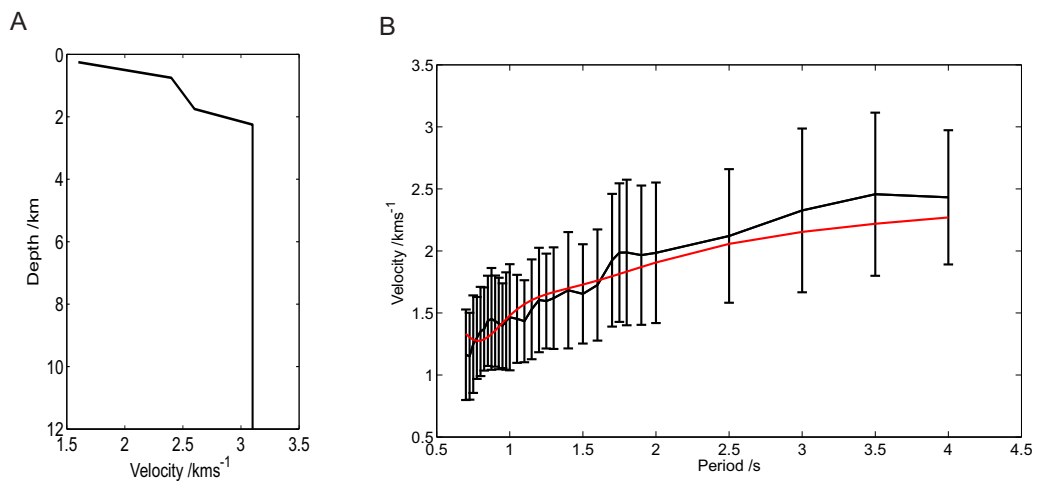
Figure 5.8: A) Velocity-depth model used as the starting model in the 3D shear velocity inversion. B) The weighted average dispersion curve, with error bars is shown in black. The red dispersion curve represents that expected from the velocity-depth model shown in A).

Horizontal slices from the 3D velocity model at depths of 1 km and 3 km are shown in figures 5.10 A and B respectively. Corresponding resolution tests and plots of raypaths

used are shown in figure 5.9. Resolution tests show that the best resolved area is between latitudes of 37 and 37.1°N. Better resolution is achieved by the eastern part of the network, whereas to the west, fewer rays cross (see figure 5.9). Particularly, the area at the south of the Sierra Alhamilla, and the area to the southeast of the Carboneras fault (the Cabo de Gata region) are poorly resolved and may be subject to some smearing. At shallow depths, the lowest velocities are observed in the Nijar basin region and close to the Carboneras fault (see figure 5.10). Low velocities are also observed in the the Sorbas basin region. Higher velocities are seen to correspond to the Sierra Cabrera and Sierra de los Filabres in the north. To the Southeast of the Carboneras fault, in the Cabo de Gata region, velocities are relatively low, though, as discussed above, this area is not well resolved and may be subject to some smearing. The general pattern observed in figure 5.10A in the velocity slices is similar down to 1 km depth, though there is an overall increase in velocity with depth.

At greater depths the resolution deteriorates. However, we can resolve low velocities near the intersection of the Carboneras and Palomares fault and in the northern part of the Sierra Alhamilla, close to the Lucainena fault zone (see figure 5.10B). Higher-velocity material is observed to underlie the Nijar basin region.
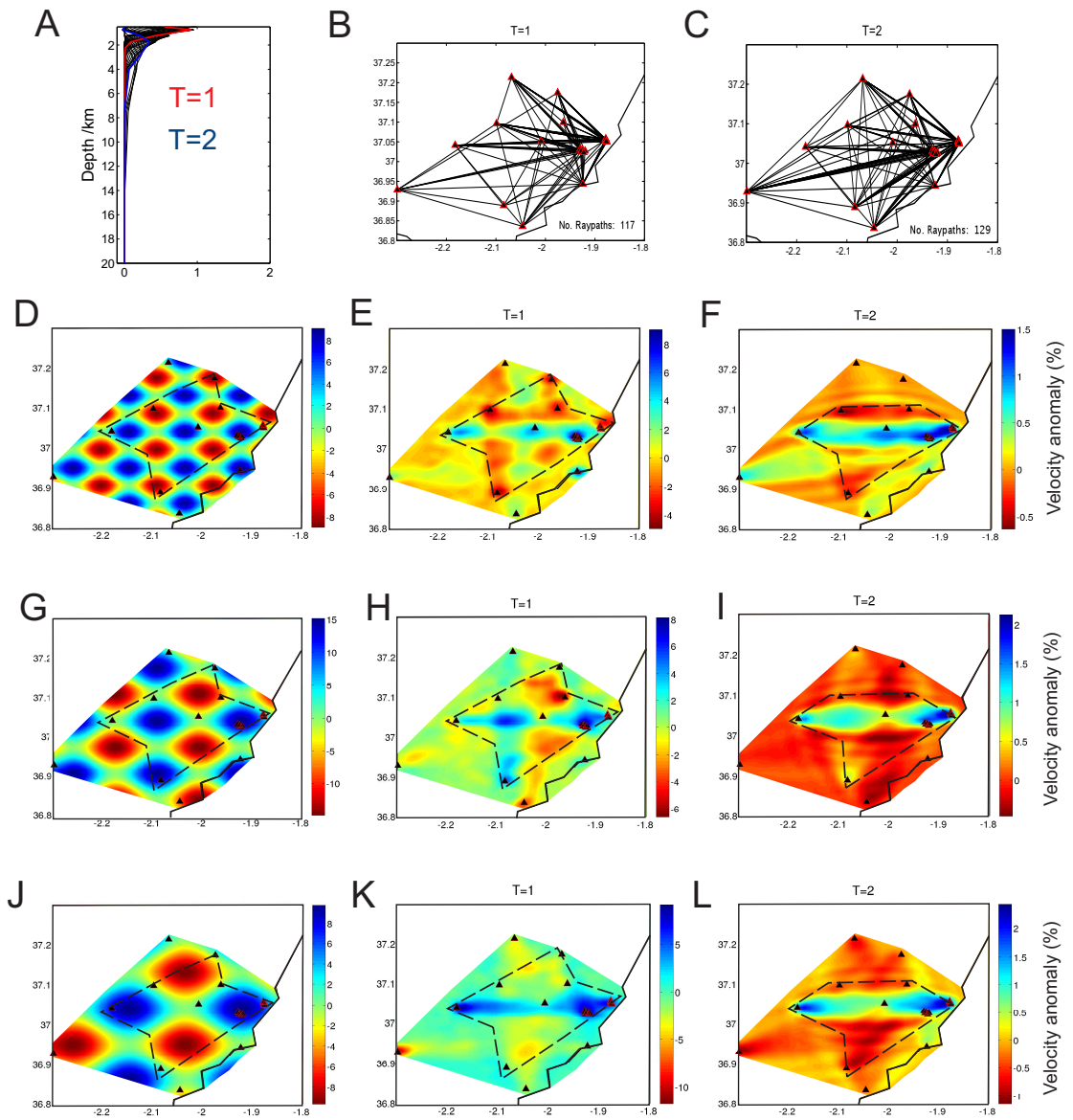
Figure 5.9: Results from resolution tests. A) shows the sensitivity kernels for each period used. Periods of 1 second and 2 seconds are highlighted in red and blue respectively. B) and C) show the raypaths used at 1 second and 2 seconds respectively. D), G) and J) show input checkerboard test models. E), H) and K) show the output models for the raypaths used at 1 second period and F), I) and L) show the outputs for the raypaths used at 2 seconds period. The areas that are resolved are indicated by the dashed lines.
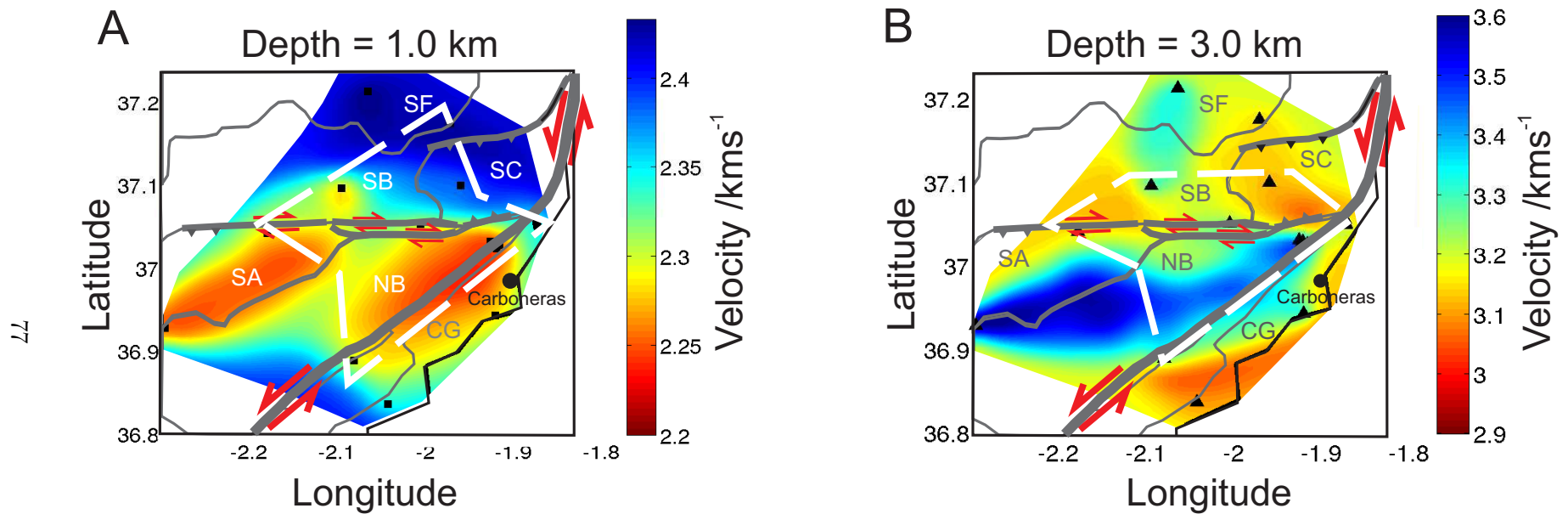
Figure 5.10: The determined velocity structure at a depth of A) 1 km and B) 3 km. The areas that are resolved are indicated by the white dashed lines. Locations of stations in the CAFE network are shown as black triangles. As a guide, the outline of the geological summary map shown in figure 5.1 is shown in grey. The main geological units are labelled: SF (Sierra de los Filabres), SC (Sierra Cabrera), SA (Sierra Alhamilla), SB (Sorbas Basin), NB (Nijar Basin) and CG (Cabo de Gata). The location of the town of Carboneras is marked by a black circle.

5.6 Discussion

The observed velocity structure can be understood in terms of the regional geology. At shallow depths, the observed low velocities correspond to the locations of the sedimentary basins in the area. The low velocities that correspond to the Nijar basin persist to depths of between 1 and 1.5 km, suggesting that this is the depth extent of the basin. A maximum sedimentary thickness in the Nijar basin of more than 1 km has previously been suggested from gravity data (*Pedrera et al.*, 2006). Borehole data have suggested depths of 500 m in some areas of the basin (*I.G.M.E.*, 1975).

At greater depths, it is interesting to note reduced velocities near the Lucainena fault and by the intersection of the Carboneras fault and the Palomares fault. The Lucainena fault is thought to have originated as an extensional detachment fault and to have been subsequently re-activated as a strike-slip fault due to changes in the regional stress field. This low-velocity area may therefore represent damage at depth due to at least two generations of faulting activity. Further to the east, the low velocities near the Carboneras and Palomares faults may represent damage due to the proximity of these two major faults, as well as thrust faults in the area.

It should be noted that the strong anisotropy of the mica schist of the Nevado Filabride complex, as reported in chapter 4, may have implications for seismic imaging of the region. The Nevado-Filabride, the Alpujarride, and the Malaguide complexes form large-scale folds in the region (see figure 3.2). In general, the foliation in the metamorphic rocks aligns with these fold axes (*Weijermars et al.*, 1985). The structurally lowest of the three sequences is the Nevado-Filabride complex. The mica schist used in laboratory measurements forms part of this sequence. As well as metamorphic mica shists, the Nevado-Filabride complex includes quartzites, medium grade metamorphic schists, marbles, amphibolites and gneisses (*Egeler*, 1963). The thickness of this lowest complex is at least 4 km but may be much greater. The laboratory measurements presented show a strong anisotropy at least to confining pressures equivalent to depths of approximately 3 km. The velocities measured perpendicular to the foliation were of the order of 30% less than those measured parallel to the foliation (see chapter 4). If the measured anisotropy due to the strong foliation in the mica schist is considered representative for the Nevado-Filabride complex, then the crust throughout this region may be highly anisotropic.

Anisotropy has previously been noted in this area from observations of SKS-splitting and studies of Pn arrivals. The SKS phase travels through the mantle as an S-wave, through the liquid outer core as a P wave and is converted back into a radially polarised S wave when passing back into the mantle. On its way to the Earth's surface, this SKS phase is split into two mutually orthogonal polarised shear waves if it propagates through an anisotropic medium. However, observed anisotropy may occur at any depth between the core-mantle boundary and the station. SKS measurements from stations
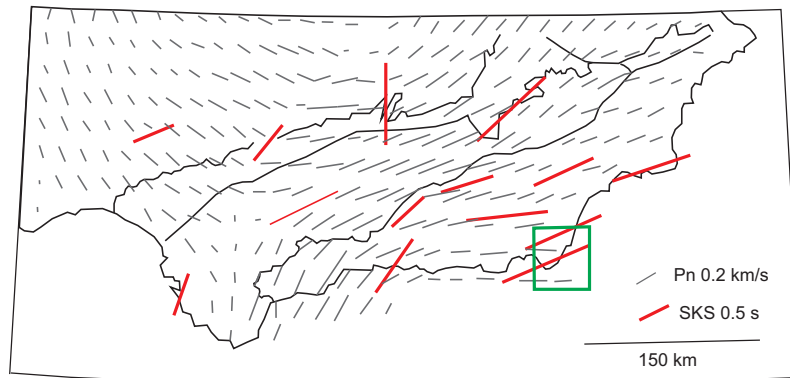
Figure 5.11: Observations of shear-wave splitting from SKS phases are shown in red (*Buontempo et al.*, 2008). Also shown are fast directions of *Pn* anisotropy from *Calvert et al.* (2000). Figure modified from *Buontempo et al.* (2008). The region of the current study is indicated by the green box.
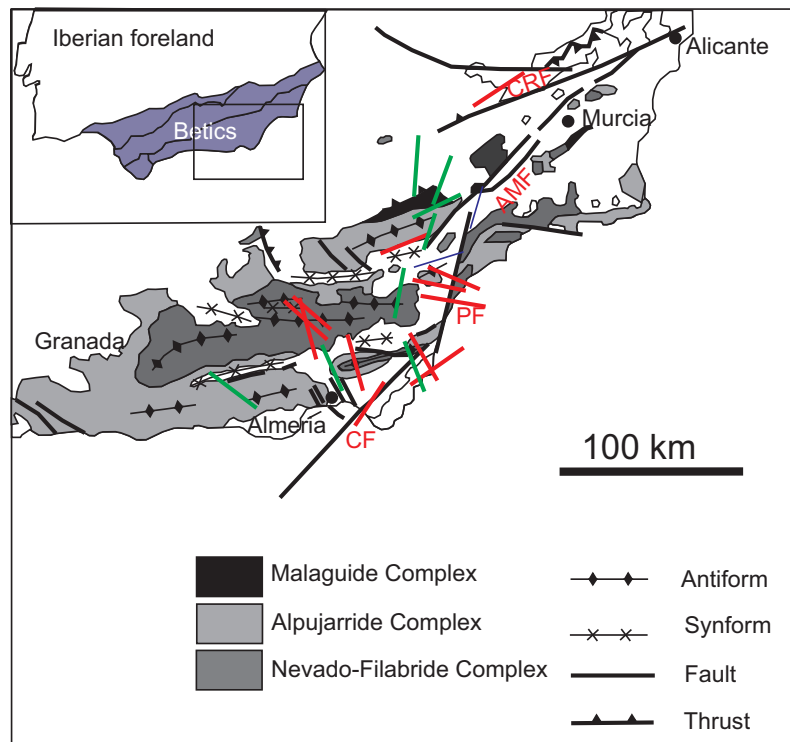
Figure 5.12: Fast directions of shear waves from regional crustal earthquakes as reported by *Buontempo and Wuestefeld* (2013). Red lines represent good measurements and green represent fair measurements. These are plotted on a simplified map of the geology, including major structural features. The labelled faults are the Carboneras Fault (CF), the Palomares Fault (PF) and the Alhama de Murcia Fault (AMF).

in the Internal Betics show ENE-WSW fast directions nearly parallel to the trend of the mountain belt (*Buontempo et al.*, 2008). Delay times of 1 - 1.5 seconds are observed (see figure 5.11). This is interpreted as anisotropy within the mantle related to deformation due to orogenesis (*Buontempo et al.*, 2008). A layer of 150 km thickness is postulated, assuming 4% anisotropy in the upper mantle. Studies of Pn anisotropy show similar orientations of fast directions (*Calvert et al.*, 2000; *Serrano et al.*, 2005). Pn travels horizontally just below the Moho and thus constrains anisotropy to that depth interval.

Given S wave velocities of 3700 and 2500 ms^{-1} (as measured in laboratory experiments of chapter 4), 4 km of anisotropic rock would cause 0.5 seconds of shear-wave splitting. Therefore, the SKS-splitting observations may have a significant crustal component. To explain the observed 1 - 1.5 s would require 8-12 km of rock with this level of anisotropy. Recently, observations of shear-wave splitting from regional, crustal events have also been presented (*Buontempo and Wuestefeld*, 2013). The observations suggest fast directions ranging from approximately E-W to NE-SW and NW-SE (see figure 5.12). These observations have been interpreted in terms of the geological fabric caused by faulting in the area. However, many of these observations may be explained by anisotropy in the metamorphic complexes of the region. Time delays of up to 0.3 seconds are observed and *Buontempo and Wuestefeld* (2013) infer that the anisotropy is concentrated in the upper 15 km of crust. Potential crustal anisotropy in this region has also been suggested by receiver function studies (A. Lodge, pers. comm.). The data set recorded in the CAFE experiment could potentially add significantly to this discussion, but such an analysis in not part of this thesis.

5.7 Conclusions

Ambient noise analysis is performed in the Carboneras area of SE Spain, using seismic data from the temporary CAFE network. Noise correlation functions representing the Green's functions of the area are calculated. The distribution of noise sources of different periods is investigated. Noise sources are generally well distributed for a range of periods, though the amplitude is found to diminish at shorter periods. For each noise correlation function a spectrogram is generated. Group velocities at each period are then determined from the ridge of the spectrogram. These are then used to develop a velocity model of the region. At shallow depths (<1 km) slow velocities are seen in the regions of the Nijar basin and the Sorbas basin. Slow velocities corresponding to the Nijar basin persist to depths of between 1 km and 1.5 km, suggesting that this is the depth extent of the basin. High velocities correspond to the locations of the Sierra Cabrera and Sierra de los Filabres. At greater depths, high velocities are observed in the Sierra de los Filabres and underlying the Nijar basin. Slower velocities are observed in the Cabo de Gata region, near the Lucainena fault zone and close to

where the Carboneras fault and the Palomares fault meet. These low velocities may be due to large areas of extensive damage due to generations of faults in the area and a complex tectonic history. It is noted that strong anisotropy measured in the mica schist of the Nevado Filabride complex may have implications for the seismic imaging of the crust in this region. The extent of the crustal anisotropy should be investigated further and future studies of the structure at depth in this region should take into account the potential crustal anisotropy.

Part II

Temporal Changes in fault zones

Chapter 6

Cracking and fluid flow at the time of an earthquake

The influences of fractures and fluids on seismic properties are discussed in chapter 2, along with the commonly-observed seismic properties of fault zones. However, both the crack density and the fluid distribution in a fault zone area are expected to change at the time of an earthquake. The current understanding of the temporal changes in both fracturing and fluid distribution in a fault zone setting are therefore summarised below. A wide range of observations are described. In the following chapter, changes in seismic attenuation at the time of the 2004 M6.0 Parkfield earthquake are investigated, and the observed signal is discussed in terms of potential coseismic and postseismic changes in fracturing and fluid flow.

6.1   Cracking at the time of an earthquake

At the time of an earthquake the crack density in a fault zone will be altered due to strong ground shaking and stress release. Fault scarps and surface breaks, representing
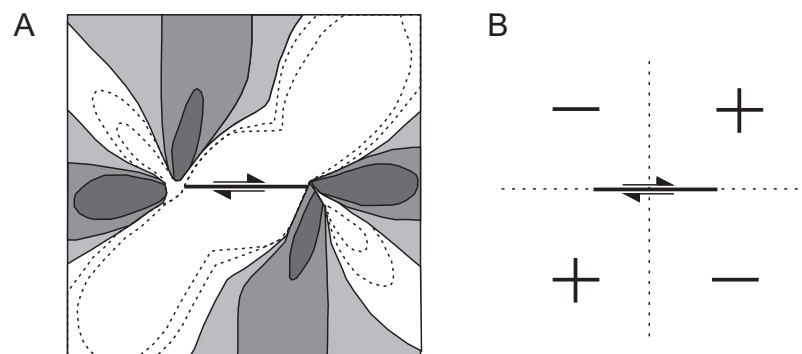
Figure 6.1: A. shows Coulomb stress changes from a right-lateral strike-slip rupture. Negative changes are shown in white and positive changes in grey. Adapted from *Cowie* (1998). B. shows dilatational strain from a right-lateral strike-slip rupture. The strain is compressional where there are + signs and dilatational where there are - signs.

the surface manifestation of a rupture are often observed and sometimes mapped after a large earthquake (e.g. *Rymer et al.* (2006)). At depth, an increase in cracking is inferred from changes in seismic properties (e.g. *Rubinstein and Beroza* (2005); *Li et al.* (1998b)). As discussed in chapter 2, seismic velocities will decrease and seismic attenuation will increase with increasing crack density (see chapter 2, figures 2.1 and 2.4).

Decreases in seismic velocity after a large earthquake are determined from repeating earthquakes (e.g. *Schaff and Beroza* (2004)), repeated active experiments (e.g. *Li and Vidale* (2001); *Li et al.* (2006)) and analysis of ambient noise (*Brenguier et al.*, 2008b; *Minato et al.*, 2012). Velocity reductions immediately after an earthquake are often interpreted as a coseismic increase in fracture density (e.g. *Li et al.* (1998b); *Vidale and Li* (2003)). Changes in both P and S wave velocities are observed. Changes in seismic attenuation, shear-wave splitting and hydrology can also give us information about cracking at the time of an earthquake.

At shallow depths (i.e in the top few hundred metres), cracking and subsequent changes in seismic velocity may be caused by strong ground shaking at the time of an earthquake. Seismic velocities are also expected to be influenced by stress changes. The Coulomb stress is defined as: $\sigma = \tau_\beta - \mu(\sigma_\beta - p)$, where τ_β is the shear stress, μ is the coefficient of friction, σ_β is the normal stress and p is the pore fluid pressure. During an earthquake, static stress changes rapidly. It decreases in most places on the fault plane, but it may increase in some places, especially near the edge of a fault, where stress concentration occurs (see figure 6.1). It is observed that aftershocks occur preferentially in areas where Coulomb stress has increased during a mainshock (e.g. *King et al.* (1994)). The Landers earthquake rupture occurred in an area where previous earthquakes had increased the Coulomb stress. The Big Bear earthquake, which followed the Landers earthquake, may also have been influenced in both its initiation point (near the maximum Coulomb stress increase due to the Landers rupture) and in its termination point (where the Coulomb stress change was negative) by stress changes due to the main event (*King et al.*, 1994). A decrease in static stress would be expected to cause a decrease in velocity in an unchanged crack network.

Dynamic (transient) stress changes, due to passing seismic waves, also occur at the time of an earthquake. Dynamic stress changes can influence permeability and simulate flow in fractures (*Elkhoury et al.*, 2006). Fracture models may provide insights into areas of preferential damage (e.g. *Rice et al.* (2005)).

6.1.1 Observations at shallow depths

By comparing signals from surface and borehole instruments, coseismic velocity changes after the 2004 M6.0 Parkfield earthquake have been determined to be concentrated in the top few hundred metres of the crust (*Rubinstein and Beroza*, 2005). It has

also been shown, after the 1989 M6.9 Loma Prieta earthquake that there is a strong correlation between the coseismic velocity change and the intensity of strong ground motion (*Rubinstein and Beroza*, 2004). Therefore, it seems likely that velocity delays are caused by cracks opening due to shallow ground shaking caused by the earthquake. Larger coseismic changes in S wave velocities than P wave velocities imply that cracks that have opened contain fluid (e.g. *Schaff and Beroza* (2004); *Rubinstein and Beroza* (2004); *Li et al.* (2003); *Li and Vidale* (2001), discussed further below).

Enhanced permeability after an earthquake has been proposed to explain hydrological observations following the 1989 Loma Prieta earthquake (*Briggs*, 1991; *Rojstaczer and Wolf*, 1992; *Rojstaczer et al.*, 1995) and the 1995 Kobe earthquake, Japan (*Tokunaga*, 1999; *Sato et al.*, 2000). These observations include enhanced stream-flow and lowering of the water table. Water appears to be expelled from relatively shallow depths, based on the chemistry of the stream water after an earthquake (*Rojstaczer et al.*, 1995). Permeability enhancement might also explain the increased electrical conductivity of water discharged after an earthquake (*Chamoille et al.*, 2005). Such an increase in permeability could be explained by an increase in fracturing at the time of an earthquake.

Coseismic decreases in seismic velocity have also been observed to greater depths of 2 km at Landers (*Li and Vidale*, 2001) and 7 km at Parkfield (*Li et al.*, 2006). These changes are also interpreted as opening of cracks during the earthquake. However, these observations are from short, dense arrays close to the fault (< 500 m). Therefore, they represent changes within the fault zone itself rather than in the surrounding rock. This difference in depth of fracturing may be explained by either a different mechanism in the fault zone (e.g. shearing induced damage) or different conditions, such as higher pore fluid pressures within the fault zone (*Rubinstein and Beroza*, 2005).

Changes in the degree of shear-wave splitting are also sometimes observed at the time of major earthquakes (e.g. *Tadokoro et al.* (1999); *Ikuta and Yamaoka* (2004)). Shear-wave splitting in a fault zone setting may be due to fractures orientated parallel to the strike of the fault, or principal stress axes. An increase in shear-wave splitting delay time may therefore imply that orientated fractures have opened or extended. In some cases, authors have searched for but not observed such a postseismic signal (e.g. *Cochran* (2003); *Cochran et al.* (2006)). It is possible that in these cases a different mechanism for shear-wave splitting is dominant (e.g. local geological fabric) or that the changes have been more heterogeneous (i.e. isotropic crack damage), and therefore have not affected one shear wave significantly more than the other, perpendicular shear wave.

Velocity reductions, when monitored, are observed to recover over approximately 2-5 years (e.g. *Brenguier et al.* (2008b); *Li et al.* (2003); *Schaff and Beroza* (2004)). This velocity recovery is inferred to be caused by cracks healing over time. Similarly,

postseismic recovery of permeability took about 2 years following two M6.5 earthquakes in the South Iceland seismic zone (*Claesson et al.*, 2007). Observed coseismic velocity and shear-wave splitting signals have been found to decay logarithmically after the earthquake (*Schaff and Beroza*, 2004; *Rubinstein and Beroza*, 2004, 2005; *Hiramatsu et al.*, 2005). A logarithmic decay is consistent with healing relationships determined from laboratory experiments (*Dieterich*, 1972).

During fault healing the reduction of crack density may be controlled by a combination of mechanical and chemical processes on the active fault. Fault healing may be affected by fluid variations or changes to the state of stress (*Blanpied et al.*, 1992; *Dodge and Beroza*, 1997; *Peltzer et al.*, 1998), fault normal compaction of the rupture zone (*Massonnet et al.*, 1996; *Boettcher and Marone*, 2004), crack dilatancy (*Nur*, 1972), time-dependent frictional strengthening (*Vidale et al.*, 1994; *Marone*, 1998; *Schaff and Beroza*, 2004), mineralogical lithification of gouge materials (*Angevine et al.*, 1982), cementation, recrystallisation, pressure solution, crack sealing and grain-contact welding (*Hickman and Evans*, 1992; *Olsen et al.*, 1998; *Sleep et al.*, 2000; *Morgan*, 2004).

6.1.2 Observations at greater depths

Variations in crustal scattering, tremor activity and GPS signals imply that coseismic changes also occur at greater depths in a fault zone. Temporal variations in crustal scattering suggest changes at depths greater than 10 km (e.g. *Audet* (2010); *Taira et al.* (2008)). Fractures may act as seismic scatterers for wavelengths comparable to the fracture size. Therefore, changes in crustal scattering suggest changes in fracture density. Time-dependent scatterers are observed in areas of predicted increases of Coulomb stress and it is suggested that changes in scatterers at these depths might be due to stress changes at the time of large earthquakes (*Taira et al.*, 2008). These crustal scatterers are interpreted as fluid-filled fractures (*Taira et al.*, 2008). Increased tremor activity at 15-40 km depths also corresponds with increased static Coulomb and shear stress changes from the 2003 San Simeon and 2004 Parkfield earthquakes (*Nadeau and Dolenc*, 2005). Changes in ambient seismic noise velocities at the time of the 2004 Parkfield earthquake are observed to have a similar decay to tremor activity and surface deformation. It has therefore been suggested that this variation in velocity might be explained by deep stress relaxation (*Brenguier et al.*, 2008b), although this has been contested by others (*Sleep*, 2009). *Minato et al.* (2012) observe coseismic decreases in ambient noise velocity at the time of the 2011 Tohoku-Oki earthquake. The velocity change shows correlation with both the changes in static strain derived from GPS records and the peak particle velocity experienced during the mainshock and 2 major aftershocks. They infer that the velocity changes may contain information on changes in the crust due to both shallow strong ground motion and deeper coseismic stress release (*Minato et al.*, 2012).

6.2 Changes in fluid distribution at the time of an earthquake

Hydrological responses to earthquakes, such as increased stream discharge, changes in stream water chemistry and water level changes in monitored well sites are often observed. As discussed above, an increase in fracturing at the time of an earthquake will cause an increase in permeability. Such changes will therefore facilitate the movement of fluid in and around the fault zone at the time of an earthquake. As discussed in chapter 2, fluid content and pore fluid pressure will affect the seismic properties of a medium. Therefore, we discuss observations of the changes in fluid distribution at the time of an earthquake, and the potential influences on the seismic properties, with reference to chapter 2. An increase in saturation will cause an increase in V_P, have little effect on V_S and increase the V_P/V_S ratio (see chapter 2, figures 2.1 and 2.2). An increase in saturation will also increase S-wave attenuation. Maximum P-wave attenuation is seen at partial saturation (see chapter 2, figure 2.5).

6.2.1 Increased shallow permeability

After the 1989 Loma Prieta earthquake, an increase in stream flow was observed within 15 minutes of the earthquake. Ionic concentrations of the stream water also increased, although the overall proportions of the major ions remained the same. Elevated ionic concentrations of stream water were observed for almost 3 years after the 1989 Loma Prieta earthquake (*Rojstaczer et al.*, 1995). Groundwater levels were lowered, in some areas by as much as 21 m, within weeks to months after the earthquake. Similarly, following the 1995 Kobe earthquake, a large amount of water was discharged, especially in mountainous areas and near active faults (*Oshima et al.*, 1996; *Tokunaga*, 1999). The anomalous flow rate gradually decreased over 2 years (*Sato et al.*, 2000). In some areas, the water table dropped more than 70 m within 90 days of the earthquake (*GRG*, 1996). The permeability has been estimated to have increased by a factor of 3.6 to 7 (*GRG*, 1996; *Sato et al.*, 2000).

Such postseismic changes have been observed following other earthquakes (*Briggs and Troxell*, 1955; *Whitehead*, 1985; *Nur*, 1974; *Waller*, 1966; *Bell and Katzer*, 1987). Changes are observed to persist for months to years. These hydrological observations can be explained together by an increase in permeability at the time of the earthquake. Permeability enhancement at the time of the earthquake would initially cause an increase in flow rates. This in turn would lower the water table. The change in water chemistry can then be explained by an increase in the proportion of water that has spent a long time interacting with rock at depth. The lack of compositional changes in stream chemistry implies that water is expelled from relatively shallow depths. After the earthquake, the permeability would be expected to decrease gradually to pre-

earthquake levels, and the water table would recover.

Changes in both P and S wave velocities are observed after an earthquake. However, greater changes in P wave velocities are often observed (e.g. *Schaff and Beroza* (2004); *Li et al.* (1998b, 2003, 2006)). A decrease in saturation is expected to decrease the P wave velocity, but have little effect on the S wave velocity. The ratio of travel time changes ($\frac{\Delta t_P}{\Delta t_S}$) can therefore reveal the state of saturation of the crust. In a Poisson solid, with isotropically oriented penny-shaped cracks, the $\frac{\Delta t_P}{\Delta t_S}$ ratio is 1.64 for dry cracks and 0.17 for water-saturated cracks (with a Poisson's ratio of 0.33) (*Garbin and Knopoff*, 1975; *Li et al.*, 2003). Applying this after the 2004 M6.0 Parkfield earthquake implies partial fluid saturation postseismically (*Li et al.*, 2006). This is also the case following the 1999 M7.1 Hector Mine earthquake (*Li et al.*, 2003) and the 1992 M7.5 Landers earthquake (*Li et al.*, 1998b). Furthermore, repeated seismic surveys (in 1994, 1996 and 1998) following the 1992 Landers earthquake show a decrease in the ratio of travel time changes. A value of 0.75 in the earlier 2 years decreases to 0.65 in the later 2 years, implying that cracks near the fault zone are becoming more fluid saturated with time after the earthquake (*Li and Vidale*, 2001). This observation fits well with the observed coseismic decrease in the water table, which recovers postseismically.

It is noted that following the 1989 Loma Prieta earthquake, the stream flow observations recover more quickly than the seismic velocities. However, stream-flow is controlled by permeability (connectivity of pore space), whereas seismic velocity is controlled by porosity (density of pore space). These observations can therefore be reconciled. We would expect permeability to recover more quickly, as closure of connective cracks will reduce permeability much more than porosity (*Rubinstein and Beroza*, 2004).

6.2.2   Poroelastic Flow

Large earthquakes coseismically cause pore pressures to increase in areas of compression and decrease in areas of dilatation (*Nur and Booker* (1972); *Björnsson et al.* (2001) and see figure 6.1). These pore-pressure gradients induce groundwater flow (*Roeloffs*, 1996) which results in poroelastic rebound i.e. postseismic subsidence within (coseimic) compressional quadrants and uplift in (coseismic) extensional quadrants. Poroelastic rebound has been inferred from InSAR measurements following the 1992 M7.3 Landers earthquake (*Peltzer et al.*, 1998; *Fialko*, 2004) the 2003 M6.6 Bam earthquake, Iran (*Fielding et al.*, 2009) and M6.0 earthquakes in Iceland (*Jonsson et al.*, 2003).

Following two strike-slip earthquakes in Iceland, *Jonsson et al.* (2003) investigated coseismic and postseismic changes in water level in geothermal wells of depth < 1.5 km. Coseismic water level increase was observed in the compressional quadrants and coseismic water level decrease in the extensional quadrants of each strike slip earthquake. Postseismically, the water level changes are in the opposite direction i.e. water

level decrease in the coseismic compressional quadrants and water level increase in the coseismic extensional quadrants. The water level changes recover within 1-2 months, similar to the surface deformation recorded in interferograms (*Jonsson et al.*, 2003). In contrast, the duration of the aftershock sequence was projected to be 3.5 years. Longer pore-pressure transients may exist at the depths of the aftershocks (3-10 km), where the permeability is expected to be lower. Water level changes are seen at wells up to 25 km from the ruptures.

Following the 1992 Landers earthquake, poroelastic rebound was observed in InSAR data at distances of 15 km from a rupture and for 3.5 years after the earthquake (*Peltzer et al.*, 1998). *Fialko* (2004) infer, from the fit of models to the InSAR and GPS data, that poroelastic rebound following the 1992 M7.3 Landers earthquake involves the whole upper crust (i.e. to a depth of 15 km).

The signal following the 2003 Bam, Iran earthquake has a much more limited spatial extent (500 m) and a relaxation time of 1.7 years. A small amount of broad-scale poroelastic rebound in the first two months after the earthquake cannot be ruled out (*Fielding et al.*, 2009).

The differences in spatial extent and recovery time in these examples are likely to be due to different levels of permeability. Longer relaxation times imply a lower permeability of the poroelastic rock volume (*Fielding et al.*, 2009).

This mechanism would be expected to form a pattern in velocity and attenuation changes, matching the areas of extension and compression. In the compressional areas where the pore pressure increases, the effective pressure will decrease. This would cause a decrease in both P and S wave velocities and an increase in both P and S wave attenuation. Conversely, in extensional areas where the pore pressure decreases, the effective pressure increases, which would cause an increase in both P and S wave velocities and a decrease in P and S wave attenuation.

6.3 Changes in Seismic Properties

As discussed above, at the time of an earthquake, an increase in cracking at shallow depths is expected due to the effects of strong ground shaking. An increase in cracking is expected to cause a decrease in both P and S wave velocities (see chapter 2, figure 2.1). Observed coseismic decreases in seismic wave velocities are often interpreted in this way. It appears that this effect is limited to the top few hundred metres, based on comparisons of surface and borehole seismic data (*Rubinstein and Beroza*, 2004). Chemical compositions of water expelled due to this increased permeability also suggest that this is a relatively shallow effect. Postseismic recovery of seismic wave velocities is interpreted as crack healing.

Hydrological observations also indicate a coseismic decrease in the water table. Therefore, a decrease in saturation at shallow levels is expected. A decrease in sat-

uration is expected to decrease the P wave velocity further, but have little effect on the S wave velocity (see chapter 2, figures 2.1 and 2.2). The difference in the P and S wave velocity changes can therefore reveal the state of saturation of the crust. Partial saturation after an earthquake is often inferred from the ratio of P and S travel times (e.g. *Li et al.* (2003, 1998b, 2006); *Schaff and Beroza* (2004)). Following the 1992 Landers earthquake, repeated seismic surveys show a decrease in the ratio of travel time changes over time, implying an increase in saturation over time (*Li and Vidale*, 2001).

An increase in cracking is also expected to cause an increase in both P and S wave attenuation (see chapter 2, figure 2.4). A decrease in saturation will cause a decrease in S wave attenuation, acting against the increase caused by the opening of fractures (see chapter 2, figure 2.5). Therefore, whether S wave attenuation is observed to increase or decrease at the time of an earthquake may depend on whether the influence of cracks opening (increasing S wave attenuation) or saturation decreasing (decreasing S wave attenuation) has a greater influence. This may depend on the initial permeability and water content of the crust, and the change in permeability caused by the earthquake. P wave attenuation is greatest at an intermediate saturation level. Therefore, a change in saturation may cause either an increase or a decrease in P wave attenuation, depending on the initial and final saturation levels (see chapter 2, figure 2.5). *Chun et al.* (2004) and *Chun et al.* (2010) use surface seismometers to observe a postseismic increase in P wave attenuation following the 1989 M7.0 Loma Prieta and 2004 M6.0 Parkfield earthquakes. Maximum attenuation was observed some weeks after the earthquakes. These changes were interpreted as an initial coseismic decrease in saturation to a level below that where maximum attenuation is observed. As the saturation postseismically increases to pre-earthquake values, attenuation must first increase until it reaches this peak and then will decrease. As discussed in the following chapter, our study of attenuation changes using borehole seismometers following the 2004 M6.0 Parkfield earthquake showed no such time lag. It is possible that this time lag is restricted to the top few hundred metres, above the level of the borehole seismometers, where saturation decreases may be most prominent.

At a greater depth, coseismic stress changes and poroelastic flow may have a strong influence over the changes in seismic velocities and attenuation. Coseismically, Coulomb stress decreases in most places on the fault plane, but it may increase near the edge of a rupture (see figure 6.1). A decrease in velocity and increase in attenuation would be expected in areas of decreased Coulomb stress. Large earthquakes coseismically cause pore pressures to increase in areas of compression and decrease in areas of dilatation (see *Nur and Booker* (1972); *Björnsson et al.* (2001) and figure 6.1). This mechanism would be expected to form a pattern in velocity and attenuation changes similar to the strain changes during the earthquake. In the compressional areas where the pore

pressure increases, a decrease in both P and S wave velocities and an increase in both P and S wave attenuation would be expected. Conversely, in extensional areas where the pore pressure decreases, an increase in both P and S wave velocities and a decrease in P and S wave attenuation would be expected. The depths at which poroelastic flow becomes an important mechanism may vary depending on the permeability in the area. Poroelastic flow has been interpreted to occur at depths of < 1.5 km (*Jonsson et al.*, 2003) and 15 km (*Fialko*, 2004).

Chapter 7

Temporal Changes in Attenuation associated with the 2004 M6.0 Parkfield Earthquake

Abstract

Elevated seismic attenuation is often observed in fault zones due to the high degree of fracturing and fluid content. However, temporal changes in attenuation at the time of an earthquake are poorly constrained, but can give indications of fracture damage and healing. In this study, spectral ratios between earthquakes within repeating clusters are calculated in an attempt to resolve temporal variations in attenuation at the time of the 2004 M6.0 Parkfield earthquake. A sharp increase in attenuation is observed immediately after the earthquake, which then decays over the next 2 years. Influences of inter-cluster magnitude variations, time-window length and previously-reported postseismic velocity changes are investigated. The postseismic decay is fit by a logarithmic function. The timescale of the decay is found to be similar to that in GPS data and ambient seismic noise velocities following the 2004 M6.0 Parkfield earthquake. The amplitude of the attenuation change corresponds to a decrease of approximately 10% in Q_p at the time of the earthquake. The greatest changes are recorded to the northeast of the fault trace, consistent with preferential damage in the extensional quadrant

behind a north-westerly propagating rupture tip. Our analysis suggests that significant changes in seismic attenuation and hence fracture dilatancy during co-seismic rupture are limited to depths of less than about 5 km.

7.1 Introduction

Fracturing around fault zones is important as it influences the strength and transport properties of the fault zone. How the fracture damage arises and how it evolves temporally over the seismic cycle is a key aspect to understand. Fault zone damage can yield information about the dynamics of rupture and changes to the physical properties of the fault as a result of the earthquake. An understanding of the static properties of fault zones has been built up by studies of their geometry and physical properties (e.g. *Chester and Logan* (1986); *Faulkner et al.* (2006); *Wibberley and Shimamoto* (2003)). A fault zone can be described by one or more fault cores, where slip is concentrated, surrounded by a damage zone with enhanced permeability due to fracturing (e.g. *Caine et al.* (1996)). The damage zone has been characterised in terms of the spatial distribution of fracture damage (e.g. *Anders and Wiltschko* (1994); *Vermilye and Scholz* (1998); *Wilson et al.* (2003)) and also in terms of the scaling of the extent of the damage zone with displacement (*Mitchell and Faulkner*, 2009; *Faulkner et al.*, 2011). This damaged interior can be imaged seismologically as a low velocity zone (e.g. *Cochran et al.* (2009)), and the in situ time-dependent evolution of fault damage can potentially be elucidated by changes in the seismic signal.

Studies of the temporal evolution of seismic velocity, InSAR and GPS data within fault zones indicate both pervasive coseismic cracking that heals with time and coseismic redistribution of crustal fluids (*Li and Vidale*, 2001; *Li et al.*, 2003; *Peltzer et al.*, 1998). Attenuation is strongly influenced by cracks and fractures, as well as pore fluids and saturation levels (e.g. *Winkler and Nur* (1982)). Elevated seismic attenuation is often observed at active faults in the brittle crust (e.g. *Rietbrock* (2001); *Lees and Lindley* (1994)). However, there are very few studies of how attenuation evolves over an earthquake cycle. Earlier studies of attenuation changes at the time of large earthquakes have used doublets or earthquake clusters with few repeats (e.g. *Got and Poupinet* (1990); *Aster et al.* (1996); *Got and Frechet* (1993)). Lower correlation coefficients between repeating events and/or greater inter-event distances meant that source variability was of concern. Use of recently-determined highly-correlated small magnitude clusters with only small variations in source position minimises these concerns. More recent studies using such clusters have reported attenuation changes at the time of earthquakes (*Allmann and Shearer*, 2007; *Chun et al.*, 2004, 2010). This study uses data from seismometers in boreholes of up to a few hundred metres depth. The high signal to noise ratio (SNR) allows smaller magnitude clusters to be used, which have a number of advantages, including more frequent repeats. Also, higher corner frequencies

93
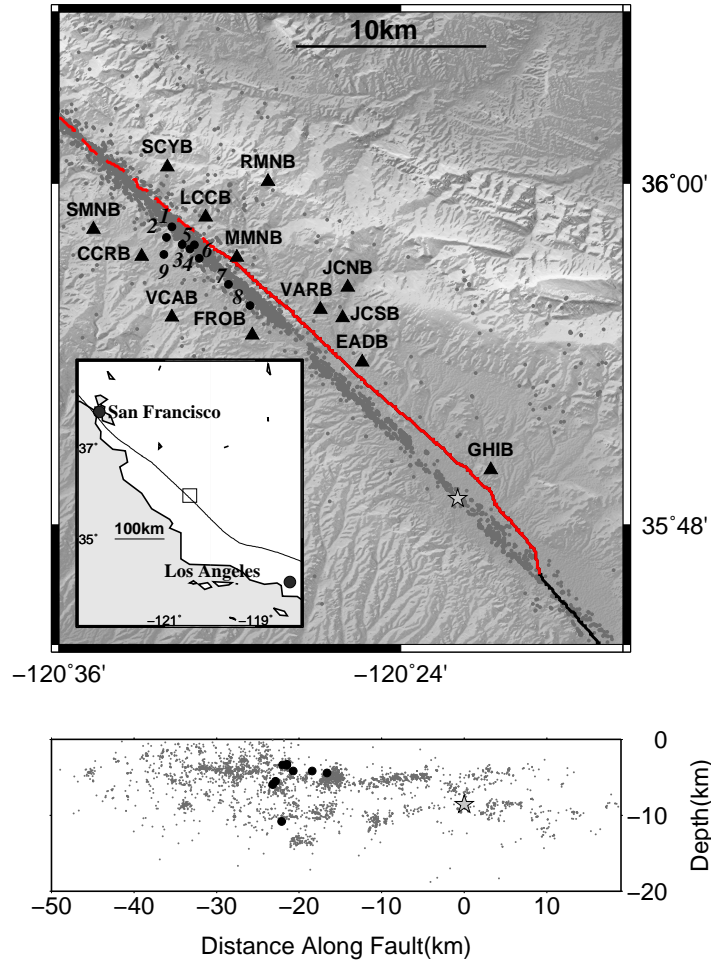
Figure 7.1: A map and cross section of the Parkfield area, indicating background seismicity (small grey circles) and locations of the clusters of earthquakes used in this study (black circles). The map also shows the locations of the HRSN stations (triangles). The hypocentre of the 2004 M6.0 earthquake is indicated by the star. The fault trace is shown (latitude and longitude by *Jennings* (1992)). The extent of the coseismic (solid red) and postseismic (dashed red) slip is also indicated (*Johanson et al.*, 2006). The inset map indicates the location of the study area shown in the map.

reduce any source influence within the recorded range, and allow us to extend our study to high frequencies.

The Parkfield area of the San Andreas fault is an area of great interest as it marks the transition between the creeping section of the fault to the North and the locked section to the South. Earthquakes of M6.0 have occurred on this segment of the fault in 1881, 1901, 1922, 1934, 1966 and most recently in 2004 (*Bakun and Lindh*, 1985; *Bakun et al.*, 2005). The 2004 event ruptured approximately the same area as the previous 1966 earthquake, but in contrast to the 1966 and 1934 events, ruptured from the south of the segment mainly towards the north (*Johanson et al.*, 2006). The hypocentre location of the 2004 earthquake, along with the extent of rupture, is shown in figure 7.1. The area has been heavily instrumented since 1985 in anticipation of this most recent M6.0 earthquake, including instrumentation for the San Andreas Fault Observatory at Depth (SAFOD) project. A major aim of this instrumentation has been to monitor temporal changes throughout the seismic cycle.

A variety of studies have taken place addressing the temporal evolution of this area at the time of the 2004 M6.0 earthquake. Such studies have included investigation of seismic velocity changes (e.g. *Rubinstein and Beroza* (2005); *Li et al.* (2006, 2007); *Brenguier et al.* (2008b)), variations in crustal scattering (*Audet*, 2010), and variations in the polarisation of surface waves (*Durand et al.*, 2011), as well as studies of GPS and InSAR data (e.g. *Johanson et al.* (2006); *Johnson et al.* (2006); *Freed* (2007)). Studies have inferred a large amount of afterslip, with moment release after the mainshock similar to the coseismic moment release (e.g. *Johanson et al.* (2006); *Johnson et al.* (2006); *Freed* (2007)). Many observations suggest that shallow coseismic damage occurs at the time of the 2004 M6.0 earthquake, which subsequently heals over time (e.g. *Rubinstein and Beroza* (2005); *Li et al.* (2006, 2007); *Sleep* (2009)). It is also suggested that there is a redistribution of crustal pore fluids and the breaking of impermeable barriers at middle to lower crustal levels (e.g. *Audet* (2010)). Increased tremor activity at depths of 15-30 km is observed immediately after the 2004 earthquake for at least 5 years and is possibly influenced by stress perturbations or episodic fluid release at these depths (*Nadeau and Guilhem*, 2009). With such coseismic damage and fluid redistribution at this time, a change in attenuation would also be expected.

In Parkfield, attenuation within the fault zone is significantly higher than in the surrounding rocks, with fault zone P-wave Quality factor, $Q_p \approx 50$ (*Abercrombie*, 2000). Attenuation across the fault in the surrounding area is highly asymmetric, with much higher attenuation to the northeast ($Q_p \approx 100$) than the southwest ($Q_p \approx 200$) (*Abercrombie*, 2000; *Bennington et al.*, 2008). This reflects the highly contrasting rock types juxtaposed across the fault. The more highly attenuating rocks to the northeast are the Franciscan basement rocks and the Great Valley sequence, which are also of lower seismic velocity than the Salinian granites and arkosic sandstones to the

southwest. *Antolik et al.* (1996) found no evidence of changes in coda attenuation at Parkfield using microearthquake clusters from 1987-1994. However, temporal changes in seismic attenuation in Parkfield around the time of the 2004 M6.0 earthquake have been noted by *Allmann and Shearer* (2007) and *Chun et al.* (2010). Here, a systematic study of attenuation values immediately after the 2004 M6.0 earthquake is presented. Clusters of repeating earthquakes are used to resolve changes in attenuation in the Parkfield area. We add spatial resolution and depth resolution to previous studies by using the borehole seismometers of the High Resolution Seismic Network (HRSN). We also investigate how the observed coseismic changes evolve with time after the earthquake. We use the dataset to investigate other possible influences in such a study i.e. how magnitude variations within a cluster, the length of chosen time window, the chosen bandwidth and coseismic velocity changes may affect results. First the data used and methods applied are presented. The results and their implications for co-seismic fracturing are then discussed.

7.2 Data

Data used are from the HRSN (see figure 7.1). This network of seismometers is deployed in boreholes of depths 63-345 m. Since its upgrade and expansion to 13 stations in March 2001, the HRSN stations have been recording continuous data at 250 samples-per-second. Seismic activity in the Parkfield area is known to be highly clustered in nature with about half of the microearthquakes recorded occurring within clusters of similar, repeating events (*Nadeau et al.*, 1994, 1995). Within the clusters, events are effectively co-located, which means that almost identical raypaths are sampled repeatedly, which is ideal for a temporal study. The extremely similar nature and location of events within a cluster are crucial for this study. Events are of similar magnitude and almost identical location and are inferred to have ruptured the same fault patch each time (*Nadeau et al.*, 1995). Clusters of seismicity at Parkfield are believed to be related to strong heterogeneities (asperities) on the fault (*Nadeau and Johnson*, 1998). These strong patches are believed to have high (100 MPa) stress drops (*Nadeau and Johnson*, 1998). The corresponding corner frequencies are therefore also very high, and often out of the range of the HRSN seismometers (e.g. see table 7.1). It has been shown that small differences in rupture kinematics and locations can cause variations in spectral ratio throughout coda, similar to that expected from significant attenuation change (*Got and Poupinet*, 1990; *Got and Frechet*, 1993; *Aster et al.*, 1996). However, corner frequencies well outside of the range of the recording set up should minimise the source effect when looking for attenuation changes.

Nine clusters of similar, repeating events with good temporal resolution between 2001-2010 are presented in this study (e.g. see figures 7.1, 7.2, 7.3, 7.4). Events are determined to be within the same cluster based on similarity. Events with a station

	Date	Time	Magnitude
	2002/03/05	08:21:22	0.196
	2002/09/05	14:21:02	0.116
	2003/03/31	17:35:32	0.133
	2003/12/20	17:03:24	0.184
	2004/06/02	05:59:15	0.132
	2004/10/02	11:07:15	0.351
	2004/10/06	15:00:02	0.288
	2004/10/13	15:47:39	0.352
	2004/10/27	13:27:41	0.339
	2004/12/07	19:54:27	0.306
	2005/02/08	12:19:34	0.297
	2005/03/26	13:09:56	0.293
	2005/05/18	07:53:46	0.306
	2005/07/08	03:10:11	0.257
	2005/09/13	00:51:07	0.264
	2005/12/01	18:50:29	0.273
	2006/03/09	10:19:59	0.288
	2006/06/07	22:09:07	0.250
	2007/03/22	00:54:52	0.313
	2007/07/15	04:44:43	0.233
	2007/12/15	10:25:43	0.268

Figure 7.2: Normalised traces from similar earthquakes within a cluster. A high degree of similarity is seen between events. This example shows events from cluster 4 as recorded at station LCCB (see figure 7.1). The 850 ms time window used is indicated by the box. The trace shown in black is the event used as the reference event (i.e. the event from this cluster that had the highest signal to noise ratio at this station). Event origin time and magnitude are also indicated.

Date	Time	Magnitude
2004/09/29	08:46:18	0.726
2004/10/01	07:06:51	0.751
2004/10/04	01:39:36	0.693
2004/10/08	11:33:23	0.683
2004/10/17	02:39:47	0.735
2004/10/28	10:03:39	0.720
2004/12/01	19:01:57	0.701
2004/12/21	09:08:57	0.653
2005/01/17	07:28:40	0.659
2005/02/28	10:04:02	0.685
2005/05/04	17:09:37	0.680
2006/01/19	10:18:08	0.650
2006/06/15	18:00:57	0.641
2007/03/11	17:31:28	0.625
2007/08/10	11:38:42	0.616
2008/01/21	19:12:24	0.619

Figure 7.3: As in figure 7.2 but for cluster 6, as recorded at station VARB.

Date	Time	Magnitude
2003/10/19	15:44:33	0.325
2004/06/09	13:50:31	0.851
2004/09/29	15:00:48	1.201
2004/09/30	05:14:59	1.160
2004/09/30	22:33:35	1.035
2004/10/02	02:10:35	1.151
2004/10/03	12:40:28	1.120
2004/10/05	13:49:21	1.120
2004/10/08	03:17:54	1.078
2004/10/11	10:36:26	1.059
2004/10/15	07:10:28	0.950
2004/10/20	07:10:45	1.050
2004/10/28	02:42:19	1.091
2004/11/05	17:01:58	1.031
2004/11/24	16:24:16	1.004
2004/12/08	04:00:16	0.955
2004/12/21	16:32:40	0.949
2005/01/08	06:59:12	0.960
2005/02/03	20:16:17	0.968
2005/03/06	15:32:38	0.596
2005/04/05	23:42:35	0.587
2005/05/07	00:06:31	0.565
2005/06/02	19:57:20	0.550
2005/06/25	06:36:39	0.484
2005/09/13	15:48:31	0.916
2006/02/09	06:51:35	0.825
2006/07/11	06:50:12	0.538
2006/11/06	17:26:35	0.801
2007/03/21	22:51:13	0.472
2007/08/10	04:32:20	0.511

Figure 7.4: As in figure 7.2 but for cluster 8, as recorded at station MMNB.

Table 7.1: Summary of clusters. Locations of clusters used in this study are given below. The range of magnitudes within each cluster, and the corresponding maximum ($\Delta\sigma = 100$ MPa) and minimum ($\Delta\sigma = 10$ MPa) corner frequencies are given, assuming the average cluster magnitude. Minimum phase coherency values for each cluster are also shown.

Cluster	Lat	Lon	Depth	Min Magn	Max Magn	Av Magn	fc min	fc max	Min. Phase Coherency
1	35.974349	-120.534003	5.943	0.834	1.185	1.071	100	215	0.96895
2	35.968176	-120.537128	5.531	0.200	0.617	0.461	202	434	0.89102
3	35.964109	-120.527876	3.341	0.571	0.825	0.667	159	342	0.98890
4	35.961460	-120.523435	3.271	0.116	0.352	0.261	254	547	0.98773
5	35.961889	-120.522817	3.390	-0.675	-0.149	-0.388	535	1153	0.90076
6	35.955913	-120.518058	4.180	0.597	0.809	0.663	160	344	0.98774
7	35.940641	-120.500785	4.171	0.421	0.859	0.607	170	367	0.96018
8	35.928252	-120.488176	4.400	0.298	1.287	0.782	139	300	0.95408
9	35.958243	-120.538726	10.827	0.854	1.450	1.221	84	181	0.92659
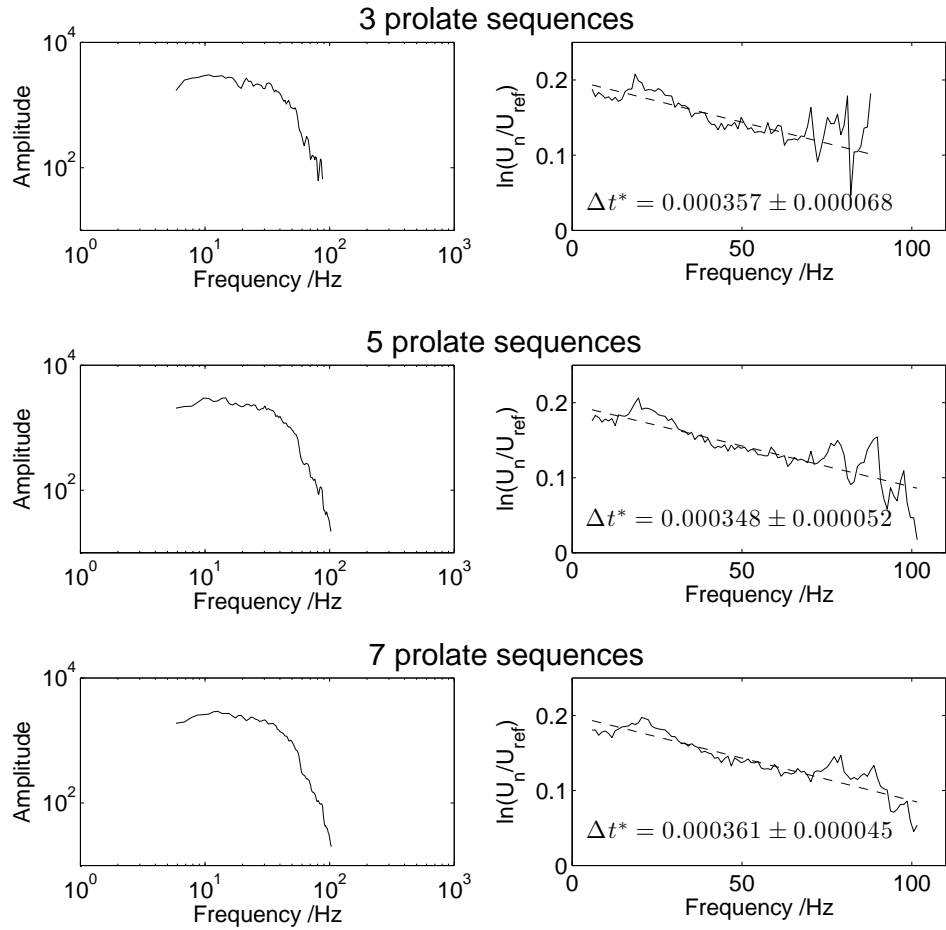
Figure 7.5: Frequency spectra and spectral ratios using 3, 5 and 7 prolate sequences in the spectral calculation. The graphs to the right show the natural logarithm of the spectral ratio as a function of frequency (solid line) and the least squares linear fit to the data (dashed line). The Δt^* values calculated from the gradient are shown for each calculation. This example is for event of origin time 2007/03/22 00:54:52 from cluster 4, as recorded at LCCB.
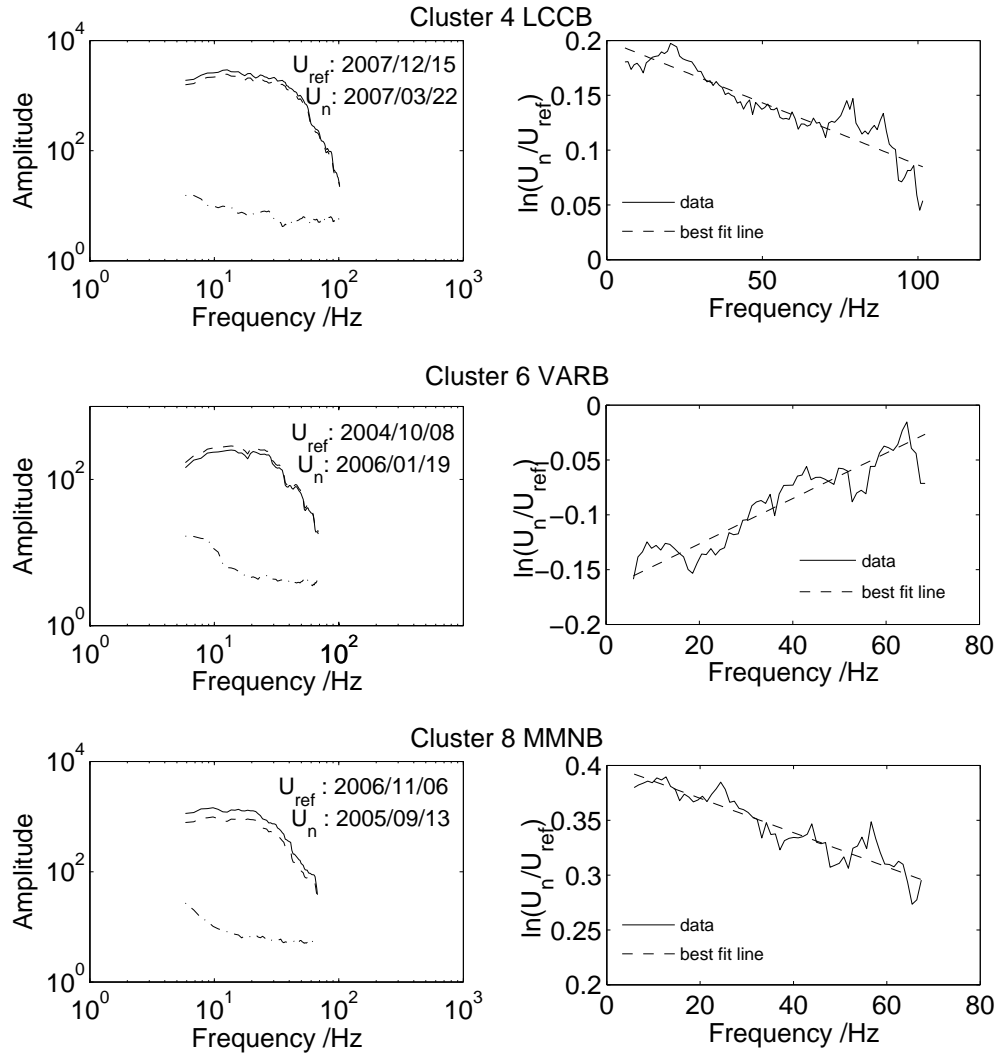
Figure 7.6: Left shows the three-component-stacked Fourier velocity spectra for an event (solid line), the corresponding reference event (dashed line) and the preceding noise (dash-dot line). Right shows the natural logarithms of the spectral ratios against frequency (solid line). Also shown are the least squares linear fit to the data (dashed line). The gradient of these lines are used to calculate the Δt^* value between an event and the reference event. Examples are shown from three separate clusters.

averaged cross-correlation above 0.8 to an original event are chosen as likely candidates for characteristic repeats of this event. Within this group, events are then characterised by dissimilarity, a weighted statistic based on phase spectrum coherences (weight 1.0), amplitude spectrum similarity (weight 0.8) and double-difference relocation separations (weight 0.3). Once these events are ranked by dissimilarity, those below the first break in the dissimilarity statistics are selected as members of the repeating sequence (*Turner et al.*, 2011). Including less similar (i.e more dissimilar) events risks the breakdown of the assumption of similar source. The locations of these clusters along with the station distribution are shown in figure 7.1. Eight of these clusters are at $3 - 6$ km depth, with the final cluster at 10.8 km depth. Events are of magnitudes M_p -0.7 to 1.5 where M_p refers to a refined estimate of event magnitude based on low frequency spectral ratios and the USGS/NCSN preferred magnitude scale (*Nadeau and Johnson*, 1998; *Wyss et al.*, 2004). The range of magnitude within clusters is as small as 0.2 to as large as 1.0. Within each cluster, the events have been double-difference relocated with respect to each other and maximum separation of event locations is typically less than $10 - 20$ m. Details of each cluster used in this study are presented in table 7.1.

7.3 Methods

The Fourier velocity spectrum U, of an earthquake i observed at a station j can be represented as:

$$U_{ij}(f) = S_i(f) \times B_{ij}(f) \times I_j(f) \tag{7.1}$$

where f is the frequency, $S(f)$ is the source model (the velocity spectrum at the source), $B(f)$ is the attenuation along the ray path and $I(f)$ is the instrument response function.

The source velocity spectrum, $S(f)$ can be modelled by

$$S_i(f) = \frac{2\pi f \Omega_0}{[1 + (\frac{f_c}{f})^{n\gamma}]^{1/n}} \tag{7.2}$$

(*Boatwright*, 1978), where f is the frequency, f_c is the source corner frequency, n and γ are dependent on the source model and define the high-frequency decay at the source, Ω_0 is the long-period plateau value at the source and:

$$\Omega_0 = \frac{M_0 R}{4\pi \rho r c^3} \tag{7.3}$$

where M_0 is the seismic moment, R describes the average radiation pattern (an average of 0.52 for P waves) (*Aki and Richards*, 1980), ρ is the crustal density, r is the hypocentral distance and c is the wave velocity. For $\gamma = 2$ and $n = 1$, $S_i(f)$ (equation 7.2) is equivalent to the Brune source model (*Brune*, 1970, 1971).

The attenuation along the raypath, B(f) is given by:

$$B_{ij}(f) = exp(-\pi t_{ij}^* f) \tag{7.4}$$

where

$$t^* = \frac{t}{Q} \tag{7.5}$$

with t as the travel time to the station and Q as the quality-factor along this path, the inverse of the whole path attenuation ($\frac{1}{Q}$).

By taking the ratio of one velocity spectrum U_1 over another U_2, recorded at the same station j, where both events have the same corner frequency and the long-period plateau values vary only due to moment, M_{0_i}, the instrument response $I(f)$ and the source $S(f)$ effectively cancel out. It can be shown, that :

$$ln\frac{U_{1j}}{U_{2j}} = ln\frac{M_{01}}{M_{02}} + \Delta t^* \pi f. \tag{7.6}$$

Therefore, in this case, a linear relationship is expected between frequency and the logarithm of the spectral ratio. Using this, a Δt^* value between the two events can be calculated from the gradient of the straight line. It should be noted that any change in t^* can be attributed to either a change in travel time t, or a change in attenuation $\frac{1}{Q}$, or a combination of both together.

In this study, spectral ratios are calculated between P arrivals of earthquakes within repeating clusters, in order to resolve temporal changes in the attenuation operator t^* and thus in attenuation ($\frac{1}{Q}$). This current study does not extend to S waves. As the S-P time is often very short, the S-wave arrival is often within the P-coda. It is therefore difficult to extract information about S-wave attenuation without contamination from the P-coda, S-P conversion and scattering.

A window of 850 ms around the P-arrival is extracted, including 150 ms before the P-arrival and 700 ms after. This time window is shown in figures 7.2, 7.3, 7.4 for the examples shown. A 850 ms window of noise immediately before the P-arrival is also extracted. The multitaper method (*Park*, 1987) is used to calculate the Fourier velocity spectra for all three components in order to capture as much energy as possible from within the time-window. Examples using 3, 5 and 7 discrete prolate sequences are calculated (see figure 7.5), but these different tapers are shown to have little effect on the calculated Δt^* values. Results quoted throughout use 7 discrete prolate sequences. Only frequencies with a SNR greater than 3 at 5-30 Hz in all three seismometer components are used. Higher frequencies are also included when the SNR is still good. Frequency spectra from the three components are then stacked. From each cluster, at each station, the event with the highest overall SNR across all frequencies is chosen as the reference event. For a particular cluster-station pair, only events with a frequency range at least 0.7 times the bandwidth of the reference event are used,

to ensure a similar bandwidth for comparable data. The spectral ratio is calculated between each event within the cluster and the reference event. A Δt^* value, relative to the reference event is determined from the gradient of the least squares linear fit of $ln(\frac{U_{1j}}{U_{2j}})$ against frequency f (see figure 7.6). Error bars are calculated as the 99% confidence intervals of the gradient. In this way, temporal changes in t^* values are determined around the time of the 2004 Parkfield event.

7.4 Analysis and Results

Spectral ratios are calculated between events from 2001-2010 within 9 clusters at the 13 HRSN stations. A similar temporal signal in Δt^* values is seen in data from each cluster. A sharp increase in t^* is seen directly after the 2004 M6.0 Parkfield earthquake followed initially by a fairly rapid decline and a subsequent gradual decrease over approximately 2 years. Examples of this trend are shown in figure 7.7. The perturbation in relative t^* values after the earthquake is generally of the order of 1×10^{-3} for each raypath. Other studies have reported postseismic changes in t^* of similar magnitude (e.g. *Chun et al.* (2004)). This signal could originate from time-dependent variations in the source, or along the travel path. Changes along the travel path that might contribute to such a change in the t^* signal include changes in seismic velocity, affecting the travel times, or changes in attenuation, $\frac{1}{Q}$. Both of these changes might be expected to occur after a large earthquake such as the 2004 M6.0 Parkfield earthquake. We therefore carry out a number of tests to determine the likely origin of the observed signal in t^*.

7.4.1 Synthetic tests

Length of Time window

A shorter time window, including only 30 ms before the P-arrival and 150 ms after, is tested without significant change to the trend of the results. Shorter time windows allow reflections and P-coda to be excluded from the signal, but also mean that the gradient of the linear fit must be calculated over a narrower frequency band. The shorter time window reduces the average t^* peak by 10% (see figure 7.8). The extra signal when the longer time window is used may represent the contribution from the coda which, by their scattered nature, sample a wider path. The time over which the perturbation decays is similar for both lengths of time window.

Bandwidth used

The effect of the bandwidth used in the spectral ratio calculation is investigated. Fixed bandwidths of 5-30 Hz, 5-45 Hz, 5-60 Hz and 5-90 Hz are investigated and the results are compared to those using the variable bandwidth method described. Spectral ratios and values of Δt^* from each of these bandwidths are shown in figure 7.9 for a number of
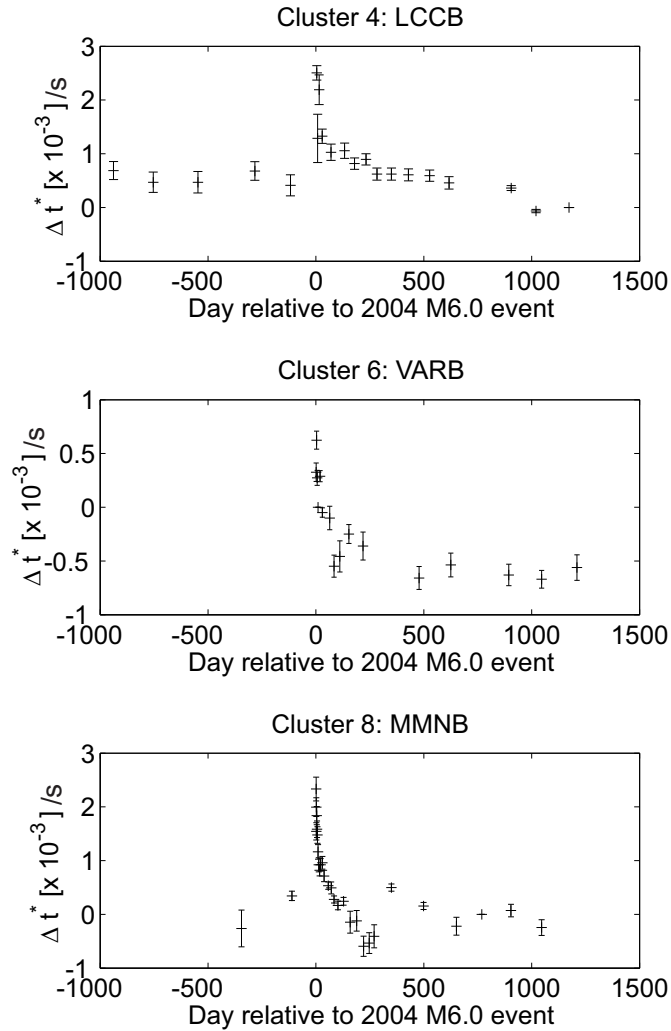
Figure 7.7: Determined Δt^* values against time in days relative to the 2004 M6.0 earthquake for three separate raypaths. Determined values are relative to the reference event. Error bars for each data point are calculated from the 99% confidence intervals of the least squares fit to equation 7.6. Prior to the M6.0 earthquake a fairly constant Δt^* is observed. Immediately after the earthquake, an elevated Δt^* is seen. This perturbation gradually decays to background levels.

Table 7.2: Bandwidths used for each raypath.

Cluster	Station	Min Bandwidth (Hz)	Max Bandwidth (Hz)	Cluster	Station	Min Bandwidth (Hz)	Max Bandwidth (Hz)
1	CCRB	5-120	5-123	6	FROB	5-88	5-105
1	EADB	5-37	5-45	6	JCNB	5-74	5-85
1	FROB	5-67	5-90	6	LCCB	5-88	5-91
1	JCNB	5-69	5-82	6	MMNB	5-56	5-75
1	LCCB	5-80	5-96	6	SCYB	5-33	5-33
1	MMNB	5-78	5-92	6	VARB	5-68	5-81
1	SCYB	5-37	5-51	6	VCAB	5-120	5-120
1	VARB	5-61	5-71	7	LCCB	5-64	5-80
1	VCAB	5-119	5-124	7	MMNB	5-68	5-88
2	LCCB	5-64	5-80	7	VARB	5-72	5-76
2	VCAB	5-113	5-121	8	CCRB	5-95	5-112
3	CCRB	5-119	5-123	8	EADB	5-47	5-58
3	FROB	5-64	5-65	8	FROB	5-104	5-116
3	JCNB	5-50	5-55	8	JCNB	5-74	5-94
3	LCCB	5-73	5-102	8	LCCB	5-62	5-78
3	MMNB	5-75	5-93	8	MMNB	5-49	5-67
3	VARB	5-42	5-45	8	SMNB	5-67	5-72
3	VCAB	5-82	5-112	8	VARB	5-68	5-90
4	CCRB	5-122	5-123	8	VCAB	5-97	5-115
4	JCNB	5-60	5-72	9	EADB	5-54	5-62
4	LCCB	5-82	5-102	9	JCNB	5-62	5-77
4	MMNB	5-67	5-80	9	LCCB	5-65	5-82
4	SCYB	5-33	5-37	9	MMNB	5-53	5-68
4	SMNB	5-95	5-103	9	RMNB	5-38	5-50
4	VARB	5-51	5-51	9	SCYB	5-51	5-51
4	VCAB	5-81	5-107	9	SMNB	5-120	5-124
5	LCCB	5-70	5-88	9	VARB	5-50	5-68
5	MMNB	5-55	5-72				
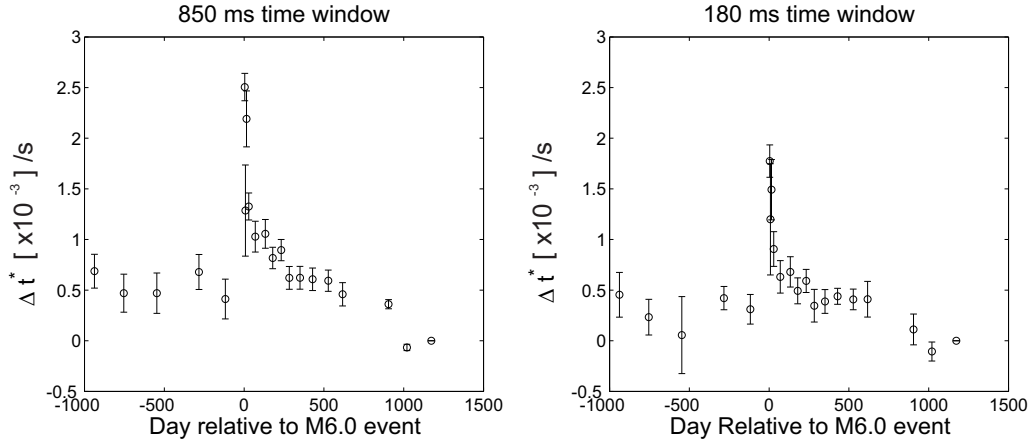
Figure 7.8: Determined Δt^* values against time, in days, relative to the 2004 M6.0 event for earthquake cluster 4 as recorded at station LCCB, using 850 ms (left) and 180 ms (right) time windows around the P arrival time. The observed perturbation immediately after the 2004 M6.0 earthquake is less in the case of the 180 ms time window, compared to the longer time window. This may represent the contribution from the coda. The time over which the perturbation decays is similar for both lengths of time window.

examples. Values are similar across different frequency bands and are generally within error of each other. Values of Δt^* determined from the 5-30 Hz bandwidth agree less well with those from the other bandwidths. Therefore, a note of caution is needed in comparing data of bandwidth less than 5-30 Hz to data of greater bandwidth. All data used in this study are required to have a minimum bandwidth of 5-30 Hz. Only 11% of raypaths use data with bandwidths shorter than 5-45 Hz. The bandwidths used for each raypath are given in table 7.2.

Coseismic Velocity Variations

As changes in t^* might be caused by changes in travel time or changes in attenuation, calculated Δt^* values are corrected for observed coseismic velocity changes. Spectral ratios of synthetic Brune spectra are calculated with velocity variations as reported by *Brenguier et al.* (2008b). The synthetically-determined Δt^* values act as correction factors to our results in order to account for the observed velocity changes. However, it is shown that this range of velocity perturbation has almost no effect on the determined Δt^* values.

Magnitude Variations

The spectral ratios method initially assumes that the two spectra involved in the division have the same corner frequency f_c and that the long-period plateau values Ω_0 vary only due to changes in moment. However, it is debatable whether or not these

108

Frequency Range (Hz)	$\triangle t^*$ (s)
5 - 30	-0.000077 $\pm$ 0.000206
5 - 45	0.000375 $\pm$ 0.000128
5 - 60	0.000409 $\pm$ 0.000080
5 - 90	0.000357 $\pm$ 0.000051
5 - 102	0.000361 $\pm$ 0.000045
5 - 30	-0.000234 $\pm$ 0.000319
5 - 45	-0.000748 $\pm$ 0.000199
5 - 60	-0.000671 $\pm$ 0.000124
5 - 68	-0.000658 $\pm$ 0.000107
5 - 30	0.000315 $\pm$ 0.000192
5 - 45	0.000507 $\pm$ 0.000109
5 - 60	0.000493 $\pm$ 0.000081
5 - 67	0.000498 0.000068
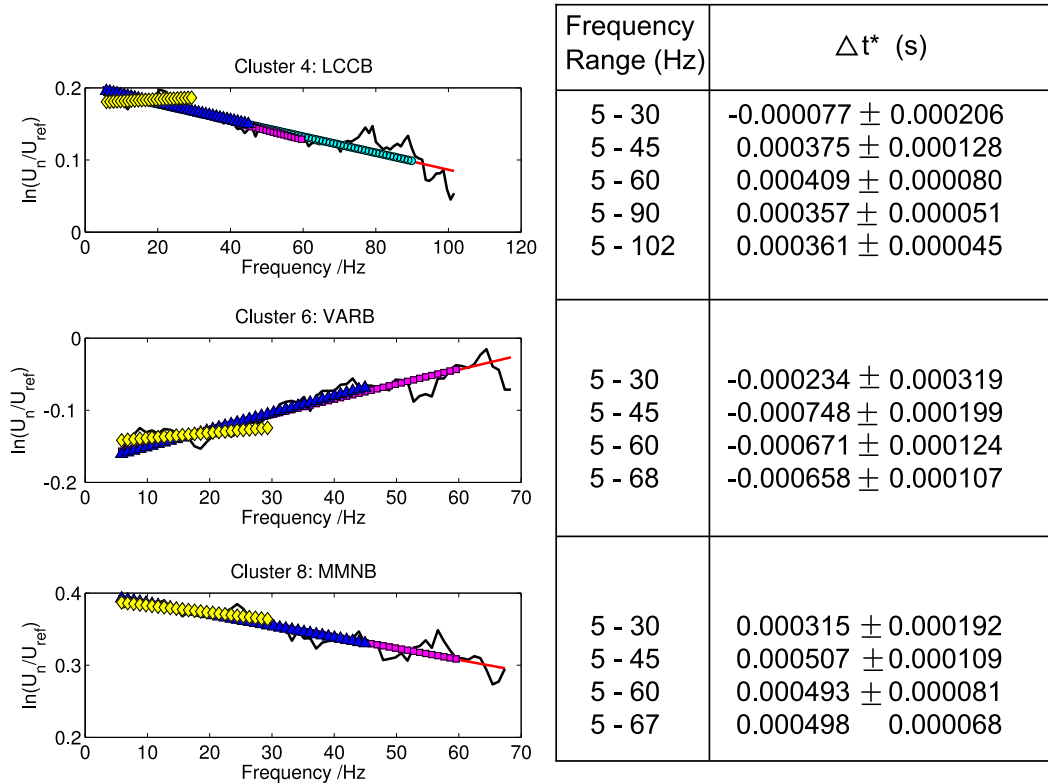
Figure 7.9: Spectral ratios and Δt^* values as calculated over frequency ranges of 5-30 Hz (yellow), 5-45 Hz (dark blue), 5-60 Hz(pink), 5-90 Hz(light blue), and a frequency range determined by the SNR (red) are shown. The examples shown are from the same events as those shown in figure 7.6.
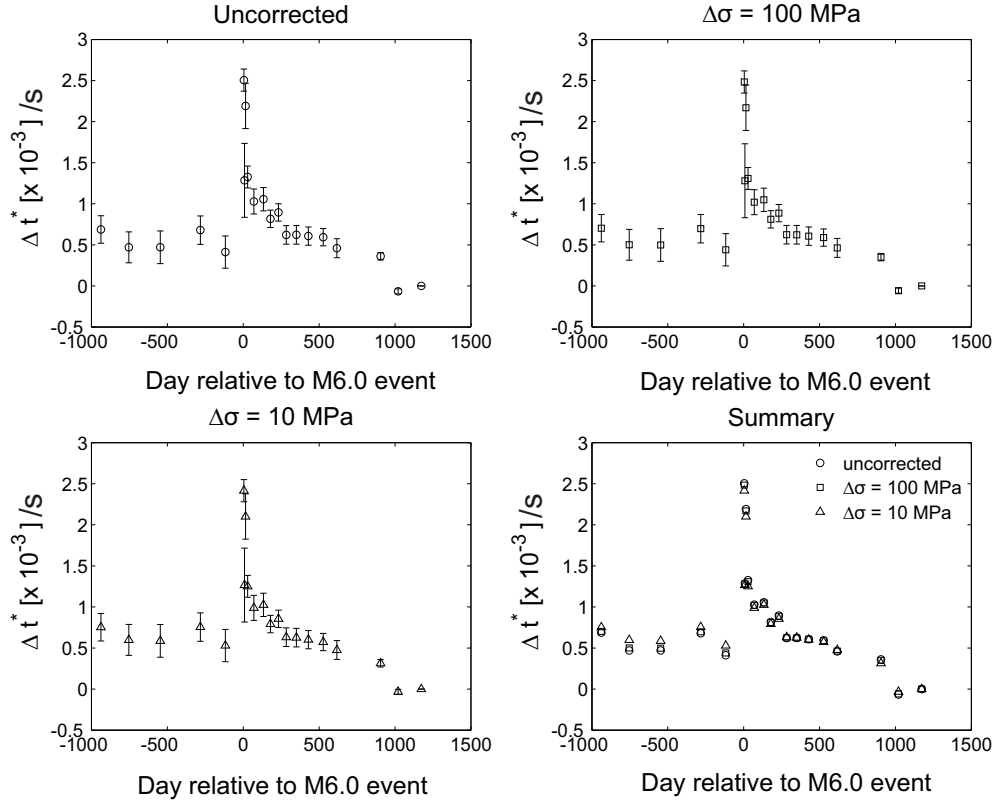
Figure 7.10: The spectral ratios method assumes constant corner frequency between events. However, corner frequency is believed to scale as in equation 7.10. As each cluster of events includes a range of event magnitudes and moments, these differences are taken into account by calculating expected differences using synthetic Brune spectra. Top left shows the original, uncorrected trend of the data, including error bars. Top right shows the data after it has been corrected for magnitude variations assuming a stress drop of 100 MPa (1 kbar). Bottom left shows the data after it has been corrected for magnitude variations assuming a stress drop of 10 MPa (0.1 kbar). Bottom right shows the original, uncorrected data along with corrections assuming stress drops of 100 MPa and 10 MPa. Error bars have been omitted for clarity in this final plot.
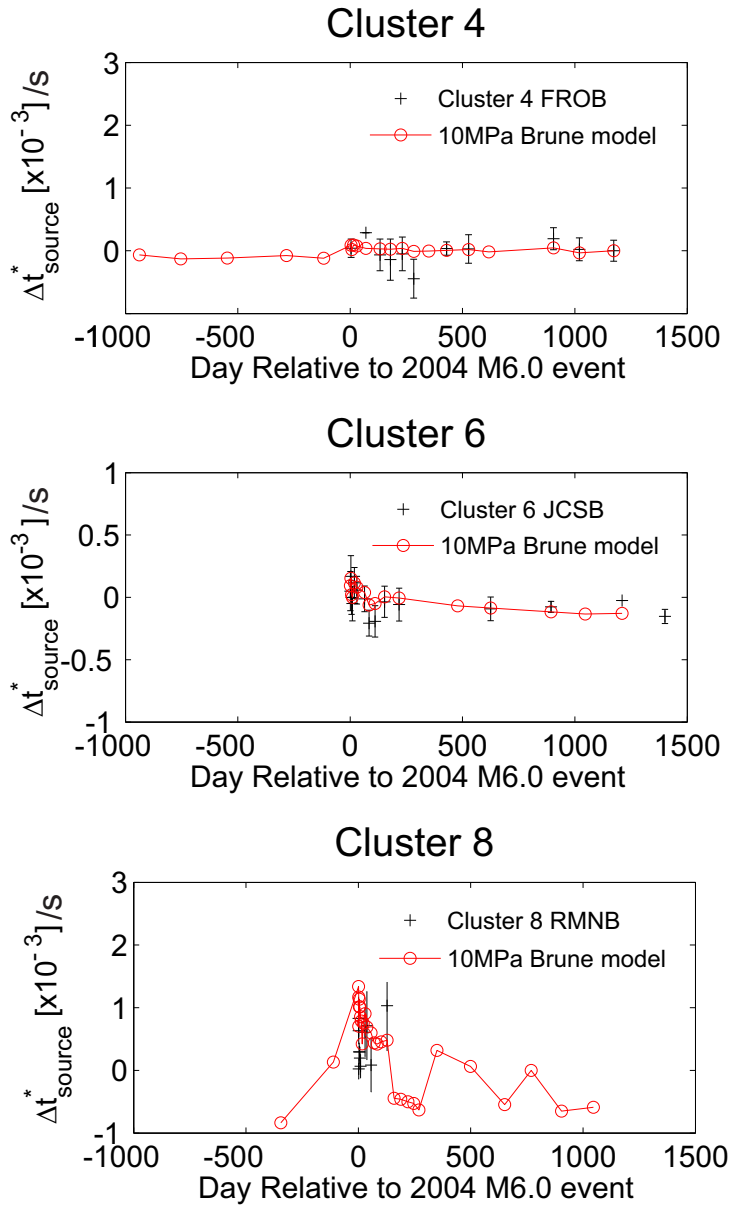
Figure 7.11: Source contributions to the Δt^* signal estimated using a Brune source model with a 10 MPa stress drop are shown in red. The maximum likely source contribution for individual clusters is estimated from the signal at the station that has recorded the least variation in t^* (the reference station). This is shown in black. Note that not all events are recorded at each reference station. Graphs are to the same scale as those in figure 7.7 for easy comparison. The two methods agree well in their estimates of source contribution for these data.

111
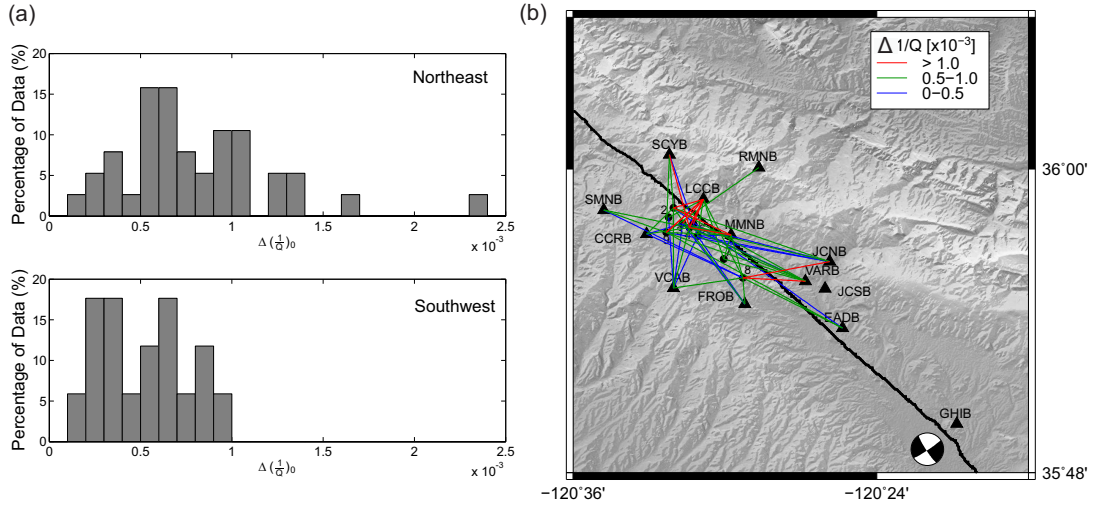
Figure 7.12: (a) Histograms of $(\Delta\frac{1}{Q})_0$ values to the northeast and southwest of the fault after corrections have been applied for postseismic velocity changes and inter-cluster magnitude variations (assuming a stress drop of 10 MPa). (b) Map of raypaths, with colors corresponding to the values of $\Delta(\frac{1}{Q})_0$ as indicated in the key. The focal mechanism represents the 2004 M6.0 Parkfield earthquake. The location of the fault trace is also shown (*Jennings*, 1992). It is observed that the largest values of $(\Delta\frac{1}{Q})_0$ are all recorded to the northeast of the fault.

conditions are met for repeating clusters of similar earthquakes. From analysing each of the individual graphs of $ln(\frac{U_1}{U_2})$ against frequency, it is observed that they are generally well-approximated by a straight line (e.g. see figure 7.6). This implies that the assumption that events within a cluster have the same corner frequency is reasonable. However, the magnitudes within a cluster are believed to vary (e.g. see table 7.1).

A change in magnitude M_p corresponds to a change in moment by:

$$log(M_0) = 1.5M_p + 9.1, \tag{7.7}$$

where moment is in Nm.

Assuming a Brune source model (*Brune*, 1970):

$$\Delta\sigma = \frac{7M_0}{16r^3} \tag{7.8}$$

where $\Delta\sigma$ is the stress drop and r is the radius of rupture, and

$$r = \frac{2.34V_p}{2\pi f_c} \tag{7.9}$$

where V_p is the P wave velocity and f_c is the corner frequency. Therefore, it is seen that the P-wave corner frequency is expected to scale with moment as:

$$f_c = [\frac{0.118\Delta\sigma V_p^3}{M_0}]^{1/3}. \tag{7.10}$$

Variation of moment within a cluster may therefore cause a variation of corner frequency f_c. An attempt is made to quantify how much this change in moment might

affect the measured changes in t^*. Given the range of magnitudes within each cluster, subsequent variations in corner frequency are calculated. Determined moment and corner frequency for each event within each cluster are then used to calculate spectral ratios of synthetic Brune spectra, assuming no changes in along-path attenuation. Values obtained from this synthetic test correspond to changes in t^* caused solely by magnitude variations within a cluster. This is then used as a correction factor against our original Δt^* values. From equation 10 it can be seen that the corner frequency used in determining the Brune spectra requires information on stress drop. Some data suggest that stress drops of repeating clusters within the Parkfield area may be unusually high (*Nadeau and Johnson*, 1998). The effects of constant stress drops of 10 MPa (0.1 kilobar) and 100 MPa (1 kilobar) are investigated here. It is found that taking these magnitude variations into account generally causes the observed peak in Δt^* to be reduced (see figure 7.10). This effect is greater at smaller stress drops, and for larger magnitude events. For a signal corrected for a stress drop of 10 MPa, using the 850 ms time window, the amplitude of the average observed Δt^* peak is reduced by less than 20% and the postseismic trend remains similar.

Chun et al. (2004, 2010) have previously corrected for magnitude variations in an alternative manner. For each cluster studied, these authors search for a reference raypath along which they believe that no temporal changes in attenuation occur. A correction factor to account for any source differences is calculated from variations in t^* along this path. This information is used to correct Δt^* measurements from other raypaths originating at the same cluster. We were unable to utilise this technique for every cluster as it was not always possible to find suitable reference raypaths where every event needed was well recorded at a reference station. However, we are able to compare the corrections that we have applied to those from the method of *Chun et al.* (2004) for some clusters for which we found adequate reference stations (figure 7.11). The corrections required by each method agree well (figure 7.11). This adds further confidence that source effects on Δt^* are removed.

Having corrected the signal for velocity changes and small magnitude variations within clusters, and tested the influence of different lengths of time window, these remaining changes in t^* values appear robust and can be interpreted as changes in attenuation of the material after the 2004 M6.0 event. Values of $\Delta \frac{1}{Q}$ are calculated from Δt^*, assuming an average velocity of 4 km/s for the eight shallow clusters. For the deeper cluster (cluster 9), a whole-path average velocity of 4.75 km/s is used. These are the average P-wave velocities to depths of 5 km and 10 km from the velocity model of *Thurber et al.* (2006).

Table 7.3: Summary of results. For each raypath, the logarithmic decay and the amplitude of the attenuation anomaly are given. The logarithmic decay is the gradient of $\Delta\frac{1}{Q}$ against $log(t)$ where t is the time in days after the earthquake. The quoted errors are the 68% confidence in the gradient from a least squares linear fit. $(\Delta\frac{1}{Q})_0$ values are determined by calculating the maximum departure from a background attenuation level. Corrections have been applied for postseismic velocity changes and inter-cluster magnitude variations assuming a stress drop of 10 MPa. The errors quoted are 99% confidence levels.

Cluster	Station	decay	error	$(\Delta\frac{1}{Q})_0$	error	Cluster	Station	decay	error	$(\Delta\frac{1}{Q})_0$	error
1	CCRB	0.000183	0.000107	0.000852	0.000121	6	FROB	0.000088	0.000029	0.000383	0.000150
1	EADB	0.000017	0.000059	0.000249	0.000129	6	JCNB	0.000113	0.000039	0.000313	0.000102
1	FROB	0.000077	0.000069	0.000544	0.000153	6	LCCB	0.000276	0.000049	0.000682	0.000317
1	JCNB	0.000090	0.000056	0.000532	0.000101	6	MMNB	0.000085	0.000033	0.000366	0.000219
1	LCCB	0.000355	0.000139	0.001226	0.000169	6	SCYB	0.000029	0.000026	0.000359	0.000276
1	MMNB	0.000156	0.000126	0.001017	0.000131	6	VARB	0.000165	0.000020	0.000505	0.000092
1	SCYB	0.000084	0.000064	0.000544	0.000312	6	VCAB	0.000062	0.000016	0.000257	0.000099
1	VARB	0.000142	0.000071	0.000611	0.000083	7	LCCB	0.000054	0.000112	0.000986	0.000311
1	VCAB	0.000040	0.000078	0.000696	0.000104	7	MMNB	0.000089	0.000127	0.000793	0.000225
2	LCCB	0.000532	0.000069	0.000917	0.000282	7	VARB	0.000064	0.000053	0.000572	0.000195
2	VCAB	0.000043	0.000027	0.000117	0.000066	8	CCRB	0.000213	0.000047	0.000494	0.000151
3	CCRB	0.000054	0.000023	0.000276	0.000118	8	EADB	0.000356	0.000048	0.000583	0.000181
3	FROB	0.000046	0.000025	0.000335	0.000225	8	FROB	0.000223	0.000082	0.000713	0.000279
3	JCNB	0.000024	0.000039	0.000139	0.000119	8	JCNB	0.000283	0.000058	0.001063	0.000205
3	LCCB	0.000376	0.000039	0.001258	0.000202	8	LCCB	0.000200	0.000017	0.000524	0.000155
3	MMNB	0.000186	0.000033	0.000691	0.000125	8	MMNB	0.000146	0.000057	0.000930	0.000194
3	VARB	0.000097	0.000018	0.000284	0.000212	8	SMNB	0.000147	0.000072	0.000398	0.000199
3	VCAB	0.000063	0.000020	0.000296	0.000094	8	VARB	0.000306	0.000063	0.001331	0.000247
4	CCRB	0.000363	0.000067	0.000995	0.000073	8	VCAB	0.000181	0.000061	0.000900	0.000157
4	JCNB	0.000174	0.000049	0.000617	0.000116	9	EADB	0.000259	0.000419	0.000666	0.000151
4	LCCB	0.000934	0.000083	0.002314	0.000198	9	JCNB	0.000135	0.000244	0.000437	0.000169
4	MMNB	0.000464	0.000087	0.001351	0.000179	9	LCCB	0.000694	0.000257	0.001003	0.000166
4	SCYB	0.000431	0.000096	0.001609	0.000702	9	MMNB	0.000679	0.000495	0.000832	0.000306
4	SMNB	0.000198	0.000041	0.000660	0.000180	9	RMNB	0.000319	0.000496	0.000865	0.000347
4	VARB	0.000269	0.000085	0.000932	0.000155	9	SCYB	0.000846	0.000508	0.000728	0.000146
4	VCAB	0.000204	0.000042	0.000659	0.000123	9	SMNB	0.000569	0.000601	0.000541	0.000142
5	LCCB	0.000314	0.000138	0.001083	0.000343	9	VARB	0.000224	0.000316	0.000633	0.000144
5	MMNB	0.000024	0.000123	0.000743	0.000368						

7.4.2 Amplitude of Perturbation

The value of the attenuation anomaly just after the earthquake, $(\Delta\frac{1}{Q})_0$, was investigated. For each raypath, the background $\Delta\frac{1}{Q}$, was determined from an average of 3 data points occurring at a time after the 2004 M6.0 earthquake, when the postseismic perturbation had diminished. The $(\Delta\frac{1}{Q})_0$ was then determined as the maximum departure from this background level. The error in the $(\Delta\frac{1}{Q})_0$ value was calculated by combining errors from the background level and the maximum departure. Investigating the spatial variability in the attenuation signal allows determination of the areas in which the greatest changes in attenuation occurred. This might correspond to the area of greatest damage in the 2004 M6.0 earthquake, or to areas where the greatest saturation changes occurred. The spatial distribution of the variability in the amplitude of perturbation was investigated by comparing signals from different raypaths. The depth dependence of the amplitude of the perturbation was investigated by comparing the signal from the one deep (10 km depth) cluster of earthquakes with the other more shallow (3−6 km depth) clusters.

7.4.3 Decay Rate

The decay rate informs us on how quickly any earthquake-induced changes return to their pre-earthquake level. Postseismic trends are often described by logarithmic (e.g. *Schaff and Beroza* (2004)), exponential (e.g. *Peltzer et al.* (1998)) or power law decays (e.g. *Baisch and Bokelmann* (2001)). Each of these models was considered in describing the decay of the observed postseismic attenuation signal. The data could adequately be represented by any of these models within error. However, from the fit to the data, we prefer a logarithmic decay. The decay rate was calculated from the gradient of the least squares fit of $\Delta\frac{1}{Q}$ against $log(t)$, with t as time in days after the earthquake. The data points were weighted by the inverse of the magnitude of their error bars and the reference data point was excluded. Errorbars for the decay rate were calculated from the 68% confidence intervals of the least squares fit. Calculated values are given in table 7.3.

7.5 Discussion

A range of coseismic and postseismic signals have been observed at the time of the 2004 M6.0 Parkfield earthquake, including changes in seismic velocities (*Brenguier et al.*, 2008b; *Li et al.*, 2006, 2007; *Rubinstein and Beroza*, 2005) and signals in GPS and InSAR data (*Freed*, 2007; *Johanson et al.*, 2006; *Johnson et al.*, 2006). Changes in seismic attenuation at this time have previously been noted by *Chun et al.* (2010) and *Allmann and Shearer* (2007). In this study, a number of clusters of repeating earthquakes have been used in an attempt to resolve better the amplitude, decay and
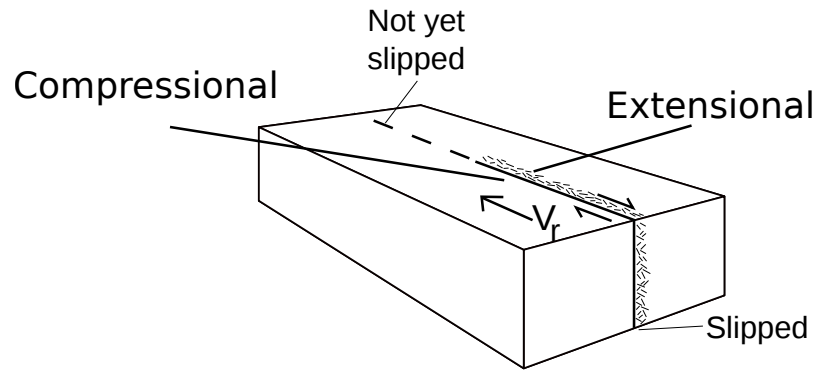
Figure 7.13: A schematic image of a right-lateral strike-slip fault is shown. The direction of rupture is indicated by the arrow labelled V_r. Along the fault plane the solid line indicates the area which has slipped and the dashed line, the area which has not yet slipped. Stresses behind the rupture tip are labelled. Greater damage is indicated in the extensional area behind the rupture tip.
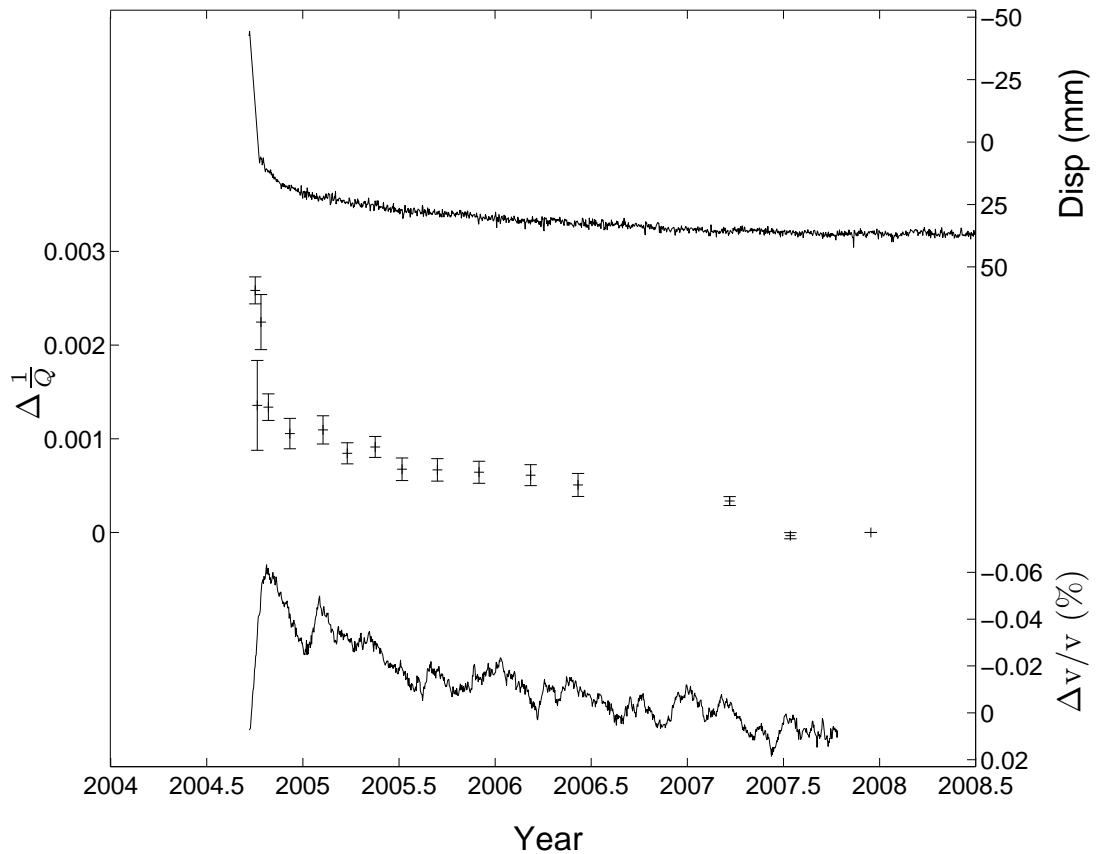
Figure 7.14: Signals in different datasets at the time of the 2004 M6.0 Parkfield earthquake. At the top, continuous GPS displacement time-series from station HOGS is plotted (http://earthquake.usgs.gov/monitoring/gps/CentralCalifornia/hogs/). Below this, the temporal change in $\Delta(\frac{1}{Q})$ determined from this study is shown (for cluster 4 at station LCCB). At the bottom, the postseismic signal in ambient seismic noise from *Brenguier et al.* (2008b) is shown.

116

location of the observed change in attenuation. Through calculating spectral ratios from clusters of repeating microearthquakes, a temporal change in t^* is found to occur at the time of the 2004 M6.0 earthquake in Parkfield. A sharp increase in t^* is observed immediately after the earthquake and this perturbation subsequently decays with time. After sensitivity tests for effects of source changes and previously reported velocity changes, it is inferred that the changes in t^* are predominantly caused by changes in attenuation of the fault zone materials i.e. a coseismic increase in attenuation and postseismic decay of this perturbation.

Commonly accepted causes of attenuation include microcracks and presence of fluids. Pore fluids are observed experimentally to have a very strong effect on attenuation in rocks (e.g. *Winkler and Nur* (1982); *Toksöz et al.* (1979)). For P waves, it is found that the highest values of attenuation are at partial saturation, with lower values for fully saturated and dry samples (*Winkler and Nur*, 1982). The connection between attenuation and fractures is inferred from the increase in Q with confining pressure, presumably due to crack closure (e.g. *Toksöz et al.* (1979)).

Fault zones are known to be areas of high seismic attenuation due to the large amount of fracturing and high fluid content. Changes in P wave attenuation within a fault zone have also been observed following the 1989 M7.0 Loma Prieta earthquake (*Chun et al.*, 2004). A large amplitude increase is seen within the first 3 weeks of the mainshock, followed by a gradual recovery to pre-shock levels in the following months (*Chun et al.*, 2004). These changes were interpreted to be caused by localised coseismic and postseismic changes in fluid saturation along the fault. At shallow depths the subsurface is fluid-saturated both inside and outside of the fault zone. Coseismically, there is redistribution of fluids, causing temporary partial fluid conditions but, postseismically these fluids re-equilibrate to fluid-saturated conditions over time. Possible explanations for changes in attenuation following the 1989 M7.0 Loma Prieta and 2004 M6.0 Parkfield earthquakes include an increase in fracture density due to strong shallow ground motion and/or a decrease in fluid saturation in the fault zone. Previously reported changes in seismic velocities have indicated that increased fracture damage occurs at the time of the 2004 M6.0 earthquake (*Rubinstein and Beroza*, 2005; *Li et al.*, 2006, 2007). This mechanism is expected to contribute to the observed changes in attenuation occurring over the same period of time. Fluid-flow expected to occur at the time of the earthquake may also contribute significantly to the signal. These possible mechanisms may also be linked, with an increase in fracture density causing an increase in pore volume and permeability, in turn allowing fluid flow and saturation changes in the area (*Rojstaczer et al.*, 1995). It seems unlikely that all clusters, located at different parts of the rupture plane would show similar time behaviour if the observations were strongly influenced by effects other than path effects e.g. source variations.

7.5.1 Amplitude of signal

Calculated values for coseismic changes in attenuation, $(\Delta\frac{1}{Q})_0$, along each raypath, are given in table 7.3 and are of the order of 1.0×10^{-3}. Previous studies of time-averaged attenuation in the Parkfield area report a P-wave Quality factor, Q_p of approximately 100-200, with lower values of 10-80 within the fault zone itself (*Abercrombie*, 2000; *Bennington et al.*, 2008). Given these time-averaged Q_p values, simple calculations suggest that an increase in $(\Delta\frac{1}{Q})_0$ of 1.0×10^{-3} corresponds to a decrease in Q_p of the order of 10%.

From spectral empirical Green's functions, *Allmann and Shearer* (2007) identified the areas of the largest attenuation changes to be near and between the 2004 M6.0 and 1966 M6.0 hypocentres. We compare signals from different raypaths in order to add to the resolution of the spatial variation in attenuation changes. The largest amplitude signals were observed from short raypaths, suggesting that the changes were concentrated laterally close to the fault (figure 7.12). This suggests that the coseismic crack damage and/or saturation changes at the time of the 2004 M6.0 earthquake were concentrated close to the fault, as might be expected.

It is also observed that the largest perturbations in the attenuation signal at this time are recorded on the northeast side of the fault (see figure 7.12). Possible explanations for this include lithological control, asymmetric damage, initial asymmetric fluid content or poroelastic flow. Abrupt changes in lithology are seen across the fault at Parkfield, with the more attenuative rocks to the northeast. If the rocks to the northeast of the fault are generally more easily fractured, this would allow larger coseismic changes in attenuation to the northeast. Furthermore, for northwest propagation during right lateral slip, the area immediately behind the rupture tip on the northeast side of the fault is expected to experience higher differential stresses that will promote rock failure, and in some cases, tensional stresses might develop (*Rice et al.*, 2005). As rocks are weaker in tension than compression, more damage might be expected here (see figure 7.13). This would allow another possible explanation for larger changes in attenuation to the northeast. Northeast of the fault is also an area where fluids are believed to be concentrated (e.g. *Unsworth and Bedrosian* (2004); *Eberhart-Philips and Michael* (1993); *Becken et al.* (2008)). Therefore, a greater change in saturation might be expected here. Poroelastic flow caused by the earthquake might also contribute to this asymmetry. Pore pressure increase is expected in the crust where compressional strain changes have occurred (e.g. *Jonsson et al.* (2003)). Conversely, where extensional strain changes have occurred, pore pressure decrease is expected. Hence, to the northeast, a decrease in saturation levels due to poroelastic dilatancy would be expected, which in turn would give an increase in attenuation. To the southwest, an increase in saturation levels would be expected, which would give a decrease in attenuation. As the polarity of the observed changes is positive on both sides of the fault,

this cannot be the first order effect. However, it might act as a second order effect, altering the observed amplitudes of the attenuation changes, so larger changes are seen to the northeast compared to the southwest. Any, or all of these explanations, may contribute to the larger amplitude signal being recorded to the northeast of the fault.

The depth extent of the coseismic attenuation signal is also considered. The HRSN stations are deployed in boreholes at depths of 60-350 m. The earthquake clusters that have been used are mainly at 3−5 km in depth, apart from cluster 9, at just over 10 km depth. This is therefore the depth range that the seismic waves are sampling. It was found that the amplitudes of the perturbations from the deep cluster were similar to those from shallow clusters. This suggests that the signal from the deep cluster is mainly affected by changes that are occurring in a depth range also sampled by the shallow clusters. As the data from the deepest cluster implies a similar change in whole-path attenuation, the main damage from the 2004 M6.0 earthquake can be constrained to depths shallower than about 5 km.

The areas of greatest attenuation change identified by *Allmann and Shearer* (2007), near the Middle Mountain asperity and between the hypocentres of the 1966 and 2004 earthquakes, are observed in this study also to undergo significant attenuation change. *Li et al.* (2006, 2007) report that velocity variations occur close to the fault, and to depths of less than 7 km. Results from this study suggest that attenuation changes may be limited to a similar depth range.

Li et al. (2006) report the area of velocity decrease after the 2004 M6.0 Parkfield earthquake to be centred to the southwest of the mapped surface fault trace, rather than the northeast, as observed for attenuation measurements in this study. *Li et al.* (2006) use a short across-fault surface array which may be more sensitive to local effects than the HRSN borehole seismometers, which give us coverage of a much larger area. Furthermore, the result of *Li et al.* (2006) may be sensitive to the steep dip of the fault to the southwest, which explains the offset of the seismicity from the mapped surface fault trace (*Hole et al.*, 2001). If the waves decouple from the low velocity zone at depth, then their signal may represent the location at which this occurs. More work is needed to determine the origin of this signal and its relationship to the signal observed in the attenuation study presented here.

Chun et al. (2010) observe a larger than expected precursory t* at one station to the southwest of the fault trace. They suggest that this may be due to greater damage to the southwest as proposed by *Li et al.* (2006). The 2003 San Simeon earthquake may have had an influence on the precursory signal observed by *Chun et al.* (2010). Although the distance between the two areas is quite large (65km), the San Simeon earthquake has clearly been shown to have had a measurable effect on seismic velocity measurements in the Parkfield area (*Brenguier et al.*, 2008b).

The studies of *Li et al.* (2006) and *Chun et al.* (2010) both use surface stations in

their analysis. These studies may therefore be more sensitive to near surface propagation changes occurring in the upper 100 m (e.g. *Rubinstein and Beroza* (2005)) due to ground shaking from the 2004 M6.0 Parkfield earthquake and changes in the near surface due to seasonality and hydrologic effects such as rainfall (e.g. *Karageorgi et al.* (1992, 1997)). It is also worth noting that *Chun et al.* (2010), using surface rather than borehole stations, observe postseismic changes in attenuation associated with the 2004 M6.0 Parkfield earthquake, with a time lag occurring before the observed peak attenuation value. Attenuation is observed to be at a maximum at partial saturation (e.g. *Winkler and Nur* (1982)). *Chun et al.* (2010) interpret their observation as an initial coseismic decrease in saturation to a level below that where maximum attenuation is observed. As the saturation postseismically increases to pre-earthquake values, attenuation must first increase until it reaches this peak and then will decrease. Such a time-lag before reaching peak attenuation is not observed in this study. This difference might be explained by either a larger change in saturation at depths shallower than HRSN stations (<300 m) or a change in the dominant attenuation mechanism, from fluids at very shallow depths to crack damage at depths greater than the HRSN stations.

7.5.2   Decay Rates

The postseismic attenuation signals were fitted with logarithmic decay rates. A logarithmic decay is consistent with healing relationships determined from laboratory experiments (*Dieterich*, 1972; *Beeler et al.*, 1994), and with field observations of postseismic changes in velocity (*Schaff and Beroza*, 2004) and shear wave splitting (*Hiramatsu et al.*, 2005). Such a trend is predicted by empirical models of afterslip (e.g. *Feigl and Thatcher* (2006)).

The attenuation perturbation decays to background levels over approximately 2 years. This is similar to other postseismic observations in Parkfield (figure 7.14) e.g. decays in GPS data (*Freed*, 2007) and in velocity perturbations from ambient seismic noise (*Brenguier et al.*, 2008b). The postseismic decay in the first few days after the 2004 M6.0 earthquake appears much slower in the ambient noise velocity data compared to the attenuation results (see figure 7.14). The 30-day stacks required by the ambient seismic noise processing may have caused the initial sharp peak to be averaged out and therefore any initial fast decay to be removed. However, the longer-term decays in the two datasets agree well.

Considering postseismic signals following a variety of different earthquakes, many of the observed perturbations decay over 2-5 years. Coseismic and postseismic velocity changes have also been observed at the time of the 1999 M7.1 Hector Mine earthquake (*Li et al.*, 2003) and the 1992 M7.5 Landers earthquake (*Li et al.*, 1998b; *Li and Vidale*, 2001). Postseismic signals in GPS data (e.g. *Savage and Svarc* (1997)) and

InSAR data (e.g. *Peltzer et al.* (1998)) have also been observed following major earthquakes. Changes in the shear wave splitting delay time after the 1997 M5.7 Tokai, Japan earthquake have been reported (*Hiramatsu et al.*, 2005) and *Baisch and Bokelmann* (2001) observe changes in coherencies between multiplet events immediately after the 1989 Loma Prieta earthquake, which gradually recover over time. These observations have variously been interpreted in terms of increased cracking, afterslip and poroelastic rebound due to pore-fluid flow. The perturbations in attenuation observed in this study decay over a similar time period to these other postseismic observations. The observations of attenuation changes in Parkfield suggest that it takes approximately 2 years for crack closure and fluid re-equlibriation to have completed after the 2004 M6.0 earthquake.

7.6 Conclusions

A temporal change in attenuation associated with the 2004 M6.0 Parkfield earthquake is observed. An increase in attenuation, $\frac{1}{Q}$ of the order of 1×10^{-3} is observed immediately after the earthquake, and this perturbation then decays over approximately 2 years. The postseismic trend is tested for influences of inter-cluster magnitude variations, length of time window used, and previously-reported velocity changes. Inter-cluster magnitude variations and time window length are found to affect the amplitude of the perturbation, but not the nature of the postseimic trend. Inter-cluster magnitude variations have a smaller effect for clusters of earthquakes with smaller magnitudes and larger stress drops. The greatest coseismic changes in attenuation are found to occur close to the fault and are recorded to the northeast of the fault trace. Analysis suggests that changes are limited to depths of less than about 5 km. A logarithmic decay is found to fit the trend of the postseismic data well. This agrees with healing relationships determined from laboratory experiments (*Dieterich*, 1972; *Beeler et al.*, 1994). The perturbation in attenuation is found to decay in a similar way to postseismic decays from GPS data and ambient seismic noise velocities following the 2004 Parkfield M6.0 earthquake. Changes in attenuation at the time of the 2004 M6.0 Parkfield earthquake imply coseismic cracking and/or fluid redistribution that recover over approximately 2 years.

Part III

Conclusions

Chapter 8

Conclusions and Further Work

8.1 Summary and Conclusions

Fault zone properties at depth are often determined from seismic properties. An understanding of the influences on seismic properties is therefore required for successful interpretations to be made. Determination of the structural, mechanical and hydrological properties of fault zones is an important step towards understanding earthquake processes.

Fault zones are heavily fractured areas that are often fluid-rich. In this thesis the influences of cracking and fluid content on seismic properties are described. Research presented was concentrated on two regions: the Carboneras fault zone region of SE Spain and the Parkfield area of the San Andreas Fault. The Carboneras fault has been suggested to provide an analogue for the structure of the Parkfield area at depth, based on comparison of field observations from the Carboneras region and seismic observations at Parkfield.

Laboratory measurements of velocities through fault gouge and fault zone rocks from the Carboneras fault are presented. The influences of fracture damage and local geological fabric on velocities are investigated. Strong velocity anisotropy is observed in the Carboneras mica schist, allowing shear wave splitting to be recorded in the laboratory. Significant differences are observed in the velocities measured parallel and perpendicular to the foliation at confining pressures of up to at least 80 MPa (equivalent to approximately 3 km depth). The velocities measured perpendicular to the foliation are of the order of 30% less than those measured parallel to the foliation. Velocity changes due to variations in crack damage in cyclic loading experiments are less than 5% of the original rock velocity. Significant anisotropy is therefore expected in seismological experiments of the Carboneras fault zone. Strong anisotropy (2-15%) has also been observed in the Parkfield area through various seismological studies (*Daley and McEvilly*, 1990; *Lewis and Gerstoft*, 2012; *Liu et al.*, 1997; *Zhang et al.*, 2007; *Ozacar and Zandt*, 2009). Anisotropy in this region has been inferred to be caused by aligned microcracks and the presence of serpentinite (*Zhang et al.*, 2007; *Liu et al.*,

1997). Therefore, in both the Carboneras fault zone area and the Parkfield area of the San Andreas fault, the local geological fabric contributes to significant, measurable shear-wave splitting.

Laboratory measurements of fault zone rock and gouge from the Carboneras area show gouge velocities to be less than those of the mica-schist rock through which the gouge cuts. A greater difference in velocity is measured between the fast and slow directions in the rock samples than between the fault gouge and the slower rock samples. This has important consequences in terms of seismically imaging the fault zone. The effects of the measured velocity anisotropy need to be considered for specific source-receiver geometries and the local geological fabric in the locations of seismic experiments. The measured velocities in the gouge are reduced by 40-50% relative to the faster rock directions and 10-20% relative to the slower rock direction. Similarly, at Parkfield observations show a 150 m wide low-velocity zone in which shear velocities are reduced by 10-40% from rock wall velocities, with the greatest changes at shallow depths (e.g. *Lees and Malin* (1990); *Michelini and McEvilly* (1991); *Eberhart-Philips and Michael* (1993); *Thurber et al.* (1997, 2003); *Roecker et al.* (2004); *Li et al.* (2004, 2006)).

Surface wave tomography and ambient noise analysis of the Carboneras fault zone region are presented. Faults in this area are resolved as low velocity features at depth. Low velocities can result from fracturing of rock. The strong anisotropy observed in laboratory experiments may have implications for this region as the anisotropic rock is widely exposed across the Carboneras area. Shear-wave splitting observations in the region are therefore discussed in terms of regional seismic imaging.

As changes in fracturing and fluid distribution occur at the time of an earthquake, temporal changes in seismic properties are also considered. A study of temporal changes in seismic attenuation at the time of the 2004 M6.0 Parkfield earthquake is presented. Seismic attenuation can give indications of fracture damage and healing. Spectral ratios between earthquakes within repeating clusters are calculated. A sharp increase in attenuation is observed immediately after the earthquake, which then decays over the next 2 years. The postseismic decay is fit by a logarithmic function. The timescale of the decay is found to be similar to that in GPS data and ambient seismic noise velocities following the 2004 M6.0 Parkfield earthquake. The amplitude of the attenuation change corresponds to a decrease of approximately 10% in Q_p at the time of the earthquake. The greatest changes are recorded to the northeast of the fault trace, consistent with preferential damage in the extensional quadrant behind a north-westerly propagating rupture tip. Our analysis suggests that significant changes in seismic attenuation and hence fracture dilatancy during co-seismic rupture are limited to depths of less than about 5 km.

8.2 Further Work

The research presented opens up new avenues for further work. The strong effect of local geological fabric on imaging of the Carboneras fault causes us to consider other faults where this may be an important issue. In the instance that much about the properties of fault zones at depth is determined from seismic techniques, knowledge and understanding of issues such as this may be crucial for successful interpretations to be made.

This work also highlights the possibility of highly anisotropic crust. Observations of large amounts of shear-wave splitting are often interpreted in terms of mantle anisotropy. However, the highly anisotropic crustal rocks considered in the laboratory experiments suggest that there may, in some cases, be a significant crustal component. Shear-wave splitting measurements from regional crustal earthquakes can help to determine if this is a factor. The shear wave splitting dataset of *Buontempo and Wuestefeld* (2013) in SE Spain, is informative but measurements remain relatively sparse, as discussed in Chapter 5.

There are still many uncertainties regarding temporal changes in a fault zone at the time of an earthquake, and throughout an earthquake cycle. Seismic properties are often used as a tool to investigate such changes. With many observations of clusters of repeating earthquakes in fault zone and subduction zone settings, such clusters may prove invaluable in determining temporal changes associated with earthquake rupture. Determining temporal changes in Q_S would complement measurements of changes in Q_P presented in Chapter 7 and aid in interpretation. A full set of V_P, V_S, V_P/V_S, Q_P, Q_S and Q_P/Q_S, determined from a single set of clusters, would potentially provide useful information. Directly comparing measurements from borehole seismometers with surface seismometers may also be informative. This is possible at Parkfield, where the PASO TRES surface network overlaps with the HRSN borehole network. The PASO TRES network was deployed just after the 2004 M6.0 earthquake (in October 2004), so could not determine coseismic changes related to this earthquake, but could determine postseismic relaxation of a signal. A more ideal set-up would involve co-located surface and borehole seismometers.

As an increase in fracturing will cause an increase in permeability and subsequent changes in fluid content, further laboratory experiments could help to develop a better understanding of how to interpret changes in a seismic signal in terms of one or both of these two influences. Also, as laboratory measurements are often carried out at ultrasonic frequencies, further work on frequencies closer to the seismic frequency range may be informative.

Bibliography

Abercrombie, R. (2000), Crustal attenuation and site effects at Parkfield, California, *JGR*, *105*(B3), 6277–6286, doi:10.1029/1999JB900425.

Adams, D., and R. Abercrombie (1998), Seismic attenuation above 10 Hz in southern California from coda waves recorded in the Cajon Pass borehole, *JGR*, *103*, 24,257–24,270.

Adams, L., and E. Williamson (1923), The compressibility of minerals and rocks at high pressures, *J. Franklin Inst.*, *195*, 475–529.

Aki, K., and P. Richards (1980), *Quantitative Seismology*, 932 pp., W.H. Freeman, New York.

Aldaya, F., F. Alvarez, J. Galindo-Zaldívar, F. González Lodeiro, A. Jabaloy, and F. Navarro Vila (1991), The Malaguide-Alpujárride contact (Betic Cordilleras, Spain): a brittle extensional detachment, *Comtes Rendus de l'Académie des Sciences Serie II*, *313*, 1447–1453.

Allerton, S., L. Lonergan, J. Platt, E. Platzman, and E. McClelland (1993), Palaeomagnetic rotations in the eastern Betic Cordillera, southern Spain, *EPSL*, *119*, 225–241.

Allmann, B. P., and P. M. Shearer (2007), Spatial and temporal stress drop variations in small earthquakes near Parkfield, California, *JGR*, *112*(B04305), doi:10.1029/2006JB004395.

Anders, M., and D. Wiltschko (1994), Microfracturing, paleostress and the growth of faults, *JSG*, *16*(6), 795–815, doi:10.1016/0191-8141(94)90146-5.

Angevine, C., D. Turcotte, and M. Furnish (1982), Pressure solution lithification as a mechanism for the stick-slip behaviour of faults, *Tectonics*, *1*, 151–160.

Antolik, M., R. Nadeau, R. Aster, and T. McEvilly (1996), Differential analysis of coda Q using similar microearthquakes in seismic gaps. Part 2: Application to seismograms recorded by the Parkfield High Resolution Seismic Network, *BSSA*, *86*(3), 890–910.

Argus, D., G. R.G., S. DeMets, and S. Stein (1989), Closure of the African-Eurasian-North America plate motion circuit and tectonics of the Gloria fault, *JGR*, *94*, 5585–5602.

Aster, R., and P. Shearer (1991), High-frequency borehole seismograms recorded in the San Jacinto fault zone, Southern California, Part 2. Attenuation and site effects, *BSSA*, *88*, 1081–1100.

Aster, R., and P. Shearer (1992), Initial shear wave particle motions and stress constraints at the Anza seismic network, *GJI*, *108*, 740–748.

Aster, R., G. Slad, J. Henton, and M. Antolik (1996), Differential analysis of coda Q using similar microearthquakes in seismic gaps. Part 1: Techniques and application to seismograms recorded in the Anza seismic gap, *BSSA*, *86*(3), 868–889.

Audet, P. (2010), Temporal variations in crustal scattering structure near Parkfield, California, using receiver functions, *BSSA*, *100*(3), 1356–1362, doi: 10.1785/0120090299.

Azema, J. (1977), Étude géologique des zones externes des Cordillères Bétiques aux confins des provinces d'Alicante et de Murcie (Espagne), *PhD thesis*.

Baisch, S., and G. Bokelmann (2001), Seismic waveform attributes before and after the Loma Prieta earthquake: Scattering change near the earthquake and temporal recovery, *JGR*, *106*(B8), 16,323–16,337, doi:10.1029/2001JB000151.

Bakun, W., and A. Lindh (1985), The Parkfield, California, earthquake prediction experiment, *Science*, *229*(4714), 619–624, doi:10.1126/science.229.4714.619.

Bakun, W., B. Aagaard, B. Dost, W. Ellsworth, J. Hardebeck, R. Harris, C. Ji, M. Johnston, J. Langbein, J. Lienkaemper, A. Michael, J. Murray, R. Nadeau, P. Reasenberg, M. Reichle, E. Roeloffs, A. Shakal, R. Simpson, and F. Waldhauser (2005), Implications for prediction and hazard assessment from the 2004 Parkfield earthquake, *Nature*, *437*, 969–974, doi:10.1038/nature04067.

Banda, E., and J. Ansorge (1980), Crustal structure under the central and eastern part of the Betic Cordillera, *Geophys.J.R.Astron.Soc.*, *63*, 515–532.

Banks, C., and J. Warburton (1991), Mid-crustal detachment in the Betic system of southeast Spain, *Tectonophysics*, *191*, 275–289.

Becken, M., O. Ritter, S. Park, P. Bedrosian, U. Weckmann, and M. Weber (2008), A deep crustal fluid channel into the San Andreas Fault system near Parkfield, California, *GJI*, *173*, 718–732, doi:10.1111/j.1365-246X.2008.03754.

Beeler, N., T. Tullis, and J. Weeks (1994), The roles of time and displacement in the evolution effect of rock friction, *GRL*, *21*(18), 1987–1990.

Bell, J., and T. Katzer (1987), Surficial geology, hydrology and late Quaternary tectonics of the IXL canyon area, Nevada, *Nevada Bureau of Mines and Geology Bulletin*, *102*, 52.

Bell, J., F. Amelung, and G. King (1997), Preliminary late Quaternary slip history of the Carboneras fault, south-eastern Spain, *Journal of Geodynamics*, *24*, 51–66.

Bellon, H. (1981), Chronologie radiométrique (K-Ar) des manifestations magmatiques autour de la Méditerranée occidentale entre 33 et 1 Ma, *Sedimentary Basins of Mediterranean Margins*, pp. 341–360.

Ben-Zion, Y. (1998), Properties of seismic fault zone waves and their utility for imaging low-velocity structures, *JGR*, *103*, 12,567–12,585.

Ben-Zion, Y., S. Katz, and P. Leary (1992), Joint inversion of fault zone head waves and direct P arrivals for crustal structure near major faults, *JGR*, *97*, 1943–1951.

Bennington, N., C. Thurber, and S. Roecker (2008), Three-dimensional seismic attenuation structure around the SAFOD site, Parkfield, California, *BSSA*, *98*(6), 2934–2947, doi:10.1785/0120080175.

Bensen, G., M. Ritzwoller, M. Barmin, A. Levshin, F. Lin, M. Moschetti, N. Shapiro, and Y. Yang (2007), Processing seismic ambient noise data to obtain reliable broadband surface wave dispersion measurements, *GJI*, *169*, 1239–1260.

Biot, M. (1956a), Theory of propagation of elastic waves in a fluid-saturated porous solid: 1. Low frequency range, *J. acoust. Soc. Am.*, *28*, 168–191.

Biot, M. (1956b), Theory of propagation of elastic waves in a fluid-saturated porous solid: 2. High frequency range, *J. acoust. Soc. Am.*, *28*, 168–191.

Biot, M. (1962a), Mechanics of deformation and acoustic propagation in porous media, *J. Appl. Phys.*, *33*, 1482–1498.

Biot, M. (1962b), Generalized theory of acoustic propagation in porous dissipative media, *J. acoust. Soc. Am.*, *34*, 1254–1264.

Birch, F. (1960), The velocity of compressional waves in rocks to 10 kilobars 1, *JGR*, *65*, 1083–1102.

Birch, F. (1961), The velocity of compressional waves in rocks to 10 kilobars 2, *JGR*, *66*, 2199–2224.

Birch, F., and D. Bancroft (1938), The effect of pressure on the rigidity of rocks, *J. of Geology*, *46*, 59–87, 113–141.

Björnsson, G., O. Flovenz, K. Saemundsson, and E. Einarsson (2001), Pressure changes in Icelandic geothermal reservoirs associated with two large earthquakes in June 2000, *Proc. 26th Workshop on Geothermal Reservoir Engineering*, *SGP-TR-168*, 327–334.

Blake, O. (2011), Seismic transport properties of fractured rock, *Ph.D. thesis*.

Blakeslee, S., P. Malin, and M. Alvarez (1989), Fault-zone attenuation of high-frequency seismic waves, *GRL*, *16*(11), 1321–1324.

Blanpied, M., D. Lockner, and J. Byerlee (1992), An earthquake mechanism based on rapid sealing of faults, *Nature*, *359*, 574–576.

Boatwright, J. (1978), Detailed spectral analysis of two small New York state earthquakes, *BSSA*, *68*(4), 1117–1131.

Boettcher, M., and C. Marone (2004), Effects of normal stress variation on the strength and stability of creeping faults, *JGR*, *109*(B03406).

Boorsma, L. (1992), Syn-tectonic sedimentation in a Neogene strike-slip basin containing a stacked Gilbert-type delta (S.E. Spain), *Sedimentary Geology*, *81*, 105–123.

Booth-Rea, G., J. Azañon, J. Martinez-Martinez, O. Vidal, and V. Garcia-Duenas (2003), Análisis estructural y evolución tectonometamórfica del basamento de las cuencas Neógenas de Vera y Huercal-Overa, Béticas Orientales, *Revista de la Sociedad Geológica de España*, *16*, 193–211.

Booth-Rea, G., J. Azanon, A. Azor, and V. Garcia-Duenas (2004), Influence of strike-slip fault segmentation on drainage evolution and topography. A case study: the Palomares Fault Zone (southeastern Betics, Spain), *Journ. of Structural Geology*, *26*, 1615–1632, doi:10.1916/j.jsg.2004.01.007.

Bousquet, J. (1979), Quaternary strike-slip faults in southeastern Spain, *Tectonophysics*, *54*, 277–286.

Bousquet, J., and C. Montenat (1974), Présence de déchrochments Nord-Est plioquaternaires dans les Cordillères bétiques orientales (Espagne): Extension et signification, *Comptes Rendus de l'Académie des Sciences, Paris*, *278*, 2617–2620.

Bradley, J., and A. Fort (1966), Internal friction in rocks, *Handbook of Physical Constants*, pp. 175–193.

Brandt, H. (1955), A study of the speed of sound in porous granular media, *Trans. Am. Soc. Engrs.*, *22*, 479–486.

Brenguier, F., N. Shapiro, M. Campillo, V. Ferrazzini, Z. Duputel, O. Coutant, and A. Nercessian (2008a), Towards forecasting volcanic eruptions using seismic noise, *Nature Geoscience*, *1*, 126–130.

Brenguier, F., M. Campilo, C. Hadziioannou, N. Shapiro, R. Nadeau, and E. Larose (2008b), Postseismic relaxation along the San Andreas fault at Parkfield from continuous seismological observations, *Science*, *321*, 1478–1481, doi: 10.1126/science.1160943.

Briggs, R. (1991), Effects of Loma Prieta earthquake on surface waters in Waddell Valley, *Water Resources Bulletin, American Water Resources Association*, *27*(6), 991–999.

Briggs, R., and H. Troxell (1955), Effects of the Arvin-Tehachapi earthquake on spring and stream flow, *Oakeshott, G.B.*, *171*, 81–97.

Brune, J. (1970), Tectonic stress and the spectra of seismic shear waves from earthquakes, *JGR*, *75*(26), 4997–5009.

Brune, J. (1971), Correction to "Tectonic stress and the spectra of seismic shear waves from earthquakes", *JGR*, *76*(20), 5002.

Buforn, E. (2008), Seismotectonics of Azores-Tunisia, *The 1755 Lisbon earthquake: revisited*, pp. 397–410.

Buforn, E., A. Udías, J. Mezcua, and R. Madariaga (1991), A deep earthquake under south Spain, 8 March 1990, *BSSA*, *81*, 1403–1407.

Buforn, E., C. Sanz de Galdeano, and A. Udías (1995), Seismotectonics of the Ibero-Maghrebian region, *Tectonophysics*, *248*, 247–261.

Buforn, E., P. Coca, A. Udías, and C. Lasa (1997), Source mechanism of intermediate and deep earthquakes in southern Spain, *J. Seismol.*, *1*, 113–130.

Buforn, E., M. Bezzeghoud, A. Udías, and C. Pro (2004), Seismic sources of the Iberia-African plate boundary and their tectonic implications, *Pure Appl. Geophys.*, *161*, 623–646.

Buforn, E., C. Pro, S. Cesca, A. Udias, and C. del Fresno (2011), The 2010 Granada, Spain, deep earthquake, *BSSA*, *101*, 2418–2430.

Buontempo, L., and A. Wuestefeld (2013), Complex fault structure interactions of crustal shear zones revealed by seismic anisotropy: an example in the eastern Betic Cordillera (Spain), *Terra Nova*, *25*, 57–64.

Buontempo, L., G. Bokelmann, G. Barruol, and J. Morales (2008), Seismic anisotropy beneath southern Iberia from SKS splitting, *EPSL*, *273*, 237–250.

Caine, J., J. Evans, and C. Forster (1996), Fault zone architecture and permeability structure, *Geology*, *24*(11), 1025–1028.

Calvert, A., E. Sandvol, D. Seber, M. Barazangi, V. Francisco, A. Gerardo, and J. Nacer (2000), Propagation of regional seismic phases (Lg and Sn) and Pn velocity structure along the Africa-Iberia plate boundary zone: Tectonic implications, *GJI*, *142*, 384–408.

Campillo, M., and A. Paul (2003), Long-range correlations in the diffuse seismic coda, *Science*, *299*(547–549).

Carrillo Rosua, F., S. Morales Ruano, and P. Fenoll Hach-Alí (2000), The three generations of gold in the Palai-Islica epithermal deposit, southeastern Spain, *The Canadian Mineralogist*, *40*, 1465–1481.

Chamoille, A., O. Fabbri, J. Mudry, Y. Guglielmi, and C. Bertrand (2005), Post-seismic permeability change in a shallow fractured aquifer following a M_L 5.1 earthquake (Fourbanne karst aquifer, Jura outermost thrust unit, eastern France), *GRL*, *32*(L18406).

Chester, F., and J. Logan (1986), Implications for mechanical properties of brittle faults from observations of the Punchbowl fault zone, California, *Pure and Applied Geophysics*, *124*(1-2), 79–106, doi:10.1007/BF00875720.

Christensen, N. (1984), Pore pressure and oceanic crustal seismic structure, *Geophys. J.R.astr.Soc*, *79*, 411–423.

Chun, K.-Y., G. Henderson, and J. Liu (2004), Temporal changes in P wave attenuation in the Loma Prieta rupture zone, *JGR*, *109*(B02317), 15, doi:10.1029/2003JB002498.

Chun, K.-Y., Q.-Y. Yuan, and G. Henderson (2010), Precursory rise of P-wave attenuation before the 2004 Parkfield earthquake, *BSSA*, *100*(2), 509–521, doi:10.1785/0120090104.

Chung, W., and H. Kanamori (1976), Source and tectonic implications of the Spanish deep-focus earthquake of 24 March 1954, *Phys. Earth Planet. Int.*, *13*, 85–96.

Claesson, L., A. Skelton, C. Graham, and C.-M. Mörth (2007), The timescale and mechanisms of fault sealing and water-rock interaction after an earthquake, *Geofluids*, *7*, 427–440.

Cochran, E., Y. Li, and J. Vidale (2006), Anisotropy in the shallow crust observed around the San Andreas Fault before and after the 2004 M6.0 Parkfield earthquake, *BSSA*, *96*(4B), S364–S375, doi:10.1785/0120050804.

Cochran, E., Y.-G. Li, P. Shearer, S. Barbot, Y. Fialko, and J. Vidale (2009), Seismic and geodetic evidence for extensive, long-lived fault damage zones, *Geology*, *37*(4), 315–318, doi:10.1130/G25306A.1.

Cochran, J., E.S. amd Vidale (2003), Near-fault anisotropy following the Hector Mine earthquake, *JGR*, *108*(B9,2436), doi:10.1029/2002JB002352.

Comas, M., V. Garcia-Duenas, and M. Jurado (1992), Neogene tectonic evolution of the alboran sea from MCS data, *Geo-Marine Letters*, *12*, 157–164.

Cowie, P. (1998), A healing-reloading feedback control on the growth rate of seismogenic faults, *Journal of Structural Geology*, *20*(8), 1075–1087.

Crampin, S. (1978), Seismic-wave propagation through a cracked solid: polarizationn as a possible dilatancy diagnostic, *Geophys.J.R.astr.Soc*, *53*, 467–496.

Crampin, S. (1981), A review of wave motion in anisotropic and cracked elastic media, *Wave Motion*, *3*, 341–391.

Crampin, S. (1984a), An introduction of wave propagation on anisotropic media, *Geophys.J.R.astr.Soc*, *76*, 17–28.

Crampin, S. (1984b), Effective anisotropic elastic constants for wave propagation through cracked solids, *Geophys.J.R.astr.Soc*, *76*, 135–145.

Daley, T., and T. McEvilly (1990), Shear-wave anisotropy in the Parkfield Varian well VSP, *BSSA*, *80*, 857–869.

de Larouzière, F., J. Bolze, P. Bordet, J. Hernandez, C. Montenat, and P. Ott d'Estevou (1988), The Betic segment of the lithospheric Trans-Alboran shear zone during the late Miocene, *Tectonophysics*, *288*, 137–152.

deMets, C., R. Gordon, D. Argus, and S. Stein (1990), Current plate motions, *GJI*, *101*, 425–478.

deMets, C., R. Gordon, D. Argus, and S. Stein (1994), Effect of recent revisions to the geomagnetic reversal time scale on estimates of current plate motions, *GRL*, *21*, 2191–2194.

Dewey, J., M. Helman, E. Turco, D. Hutton, and S. Knott (1989), Alpine tectonics, *Geological Society of London Special Publications*, *45*(265–283).

Dieterich, J. (1972), Time-dependent friction in rocks, *JGR*, *77*(20), 3690–3697.

Dodge, D., and G. Beroza (1997), Source array analysis of coda waves near the 1989 Loma Prieta, California mainshock: Implications for the mechanism of coseismic velocity changes, *JGR*, *102*(B11), 24,437–24,458.

Duputel, Z., V. Ferrazzini, F. Brenguier, and N. Shapiro (2009), Real time monitoring of relative velocity changes using ambient seismic noise at the Piton de la Fournaise volcano (La Réunion) from January 2006 to June 2007, *Journal of Volcanology and Geothermal Research*, *184*, 164–173.

Durand, S., J. Montagner, P. Roux, F. Brenguier, R. Nadeau, and Y. Ricard (2011), Passive monitoring of anisotropy change associated with the Parkfield 2004 earthquake, *GRL*, *38*(L13303), doi:10.1029/2011GL047875.

Dwiewonski, A., S. Bloch, and M. Landisman (1969), A technique for analysis of transient seismic signals, *BSSA*, *59*(427–444).

Dwiewonski, A., J. Mills, and S. Bloch (1972), Residual dispersion measurement - a new method of surface-wave analysis, *BSSA*, *62*(129–139).

Eberhart-Philips, D., and A. Michael (1993), Three-dimensional velocity structure, seismicity and fault structure in the Parkfield Region, Central California, *JGR*, *98*(B9), 15,737–15,757.

Egeler, C. (1963), On the tectonics of the eastern Betic Cordilleras (SE Spain), *Geol. Rundsch.*, *52*, 260–269.

Egeler, C., and O. Simon (1969), Orogenic evolution of the Betic Zone (Betic Cordilleras, Spain), with emphasis on the nappe structures, *Geol. Mijnbouw*, *48*(296–305).

Elkhoury, J., E. Brodsky, and D. Agnew (2006), Seismic waves increase permeability, *Nature*, *44*(29).

Evans, R. (1984), Anisotropy: a pervasive feature of fault zones?, *Geophys. J.R.astr.Soc.*, *76*, 157–163.

Faulkner, D. (1997), The role of clay-bearing fault gouges in controlling fluid pressures in fault zones: implications for fault mechanics, *Ph.D. thesis*, p. 279.

Faulkner, D., A. Lewis, and E. Rutter (2003), On the internal structure and mechanics of large strike-slip fault zones: field observations of the Carboneras fault in southeastern spain, *Tectonophysics*, *367*, 235–251.

Faulkner, D., T. Mitchell, D. Healy, and M. Heap (2006), Slip on 'weak' faults by the rotation of regional stress in the fracture damage zone, *Nature*, *444*, 922–925, doi:10.1038/nature05353.

Faulkner, D., T. Mitchell, E. Rutter, and J. Cembrano (2008), On the structure and mechanical properties of large strike-slip faults, *Geological Society London, Special Publications*, *299*, 139–150.

Faulkner, D., T. Mitchell, J. Behnsen, T. Hirose, and T. Shimamoto (2011), Stuck in the mud? Earthquake nucleation and propagation through accretionary forearcs, *GRL*, *38*(L18303), doi:10.1029/2011GL048552.

Favre, P., G. Stampfli, and W. Wildi (1991), Jurassic sedimentary record and tectonic evolution of the northwestern corner of Africa, *Palaeogeogr. Palaeoclimatol. Palaeoecol.*, *87*, 53–73.

Feigl, K., and W. Thatcher (2006), Geodetic observations of post-seismic transients in the context of the earthquake deformation cycle, *C.R. Geoscience*, *338*, 1012–1028, doi:10.1016/j.crte.2006.06.006.

Fialko, Y. (2004), Evidence of fluid-filled upper crust from observations of postseismic deformation due to the 1992 M_w 7.3 Landers earthquake, *JGR*, *109*(B08401), doi:10.1029/2004JB002985.

Fielding, E., P. Lundgren, R. Burgmann, and G. Funning (2009), Shallow fault-zone dilatancy recovery after the 2003 Bam earthquake in Iran, *Nature*, *458*, 64–68, doi:10.1038/nature07817.

Foxford, K., I. Garden, J. Walsh, J. Watterson, S. Guscott, S. Burley, and J. Lewis (1998), Structure and content of the Moab fault zone, Utah, USA, and its implication for fault seal prediction, *Faults, Fault Sealing and Fluid Flow in Hydrocarbon Reservoirs*, *147*, 87–103.

Freed, A. (2007), Afterslip (and only afterslip) following the 2004 Parkfield, California, earthquake, *GRL*, *34*(L06312), doi:10.1029/2006GL029155.

Frizon de Lamotte, D. (1987), Un exemple de collage synmétamorphe: la déformation Miocène des Temsamane (Rif externe, Maroc), *Bull. Geol. Soc. Fr.*, *3*, 337–344.

Galindo-Zaldivar, J., A. Gil, M. Borque, F. Gonzalez-Lodeiro, A. Jabaloy, C. Marin-Lechado, P. Ruano, and C. Sanz de Galdeano (2003), Active faulting in the internal zones of the central Betic Cordilleras (SE Spain), *Journal of Geodynamics*, *36*, 239–250.

Garbin, H., and L. Knopoff (1975), Elastic moduli of a medium with liquid-filled cracks, *Quart. Appl. Math.*, *32*, 301–303.

García-Dueñas, V., J. Martinez, M. Orozco, and J. Soto (1988), Plis-nappes, cisaillements syn-à post-metamorphiques et cisaillements ductiles-fragiles en distension dans les Nevado-Filábres (Cordillères Bétiques, Espagne), *Acad. Sci. Ser. I*, *307*, 1889–1395.

García-Dueñas, V., J. Balanyá, and J. Martínez-Martínez (1992), Miocene extensional detachment in the outcropping basement of the Northern Alboran basin (Betics) and their tectonic implications, *Geo-Marine Letters*, *12*, 88–95.

Gardner, G., M. Wyllie, and D. Droschak (1964), Effects of pressure and fluid saturation on the attenuation of elastic waves in sands, *J. Petr. Tech.*, *16*, 189–198.

Gianconia, F., G. Booth-Rea, J. Martínez-Martínez, J. Azañón, M. Pérez-Peña, J. Perez-Romero, and I. Villegas (2012), Geomorphic evidence of active tectonics in the the Sierra Alhamilla (Eastern Betics, SE Spain), *Geomorphology*, *145-146*(90–106), doi:10.1016/j.geomorph.2011.12.043.

Gordon, R., and L. Davis (1968), Velocity and attenuation of seismic waves in imperfectly elastic rock, *JGR*, *73*, 3917–3935.

Got, J., and J. Poupinet, G. amd Frechet (1990), Changes in source and site effects compared to coda Q^{-1} temporal variations using microearthquake doublets in California, *Pure Appl. Geophys.*, *134*(2), 195–228.

Got, J.-L., and J. Frechet (1993), Origins of amplitude variations in seismic doublets: source or attenuation process?, *GJI*, *114*, 325–340.

Gràcia, E., R. Pallàs, J. Soto, M. Comas, X. Moreno, E. Masana, P. Santanach, S. Diez, M. García, and J. Dañobeitia (2006), Active faulting offshore SE Spain (Alboran Sea): Implication for earthquake hazard assessment in the Southern Iberian margin, *EPSL*, *241*, 734–749.

GRG (1996), Influence by the Hyogoken-Nanbu earthquake to the groundwater including hotspring water, *Groundwater Research Group, Great Earthquakes, Geologists' Roles in Time of Disaster*, pp. 133–147.

Grimison, N., and W. Chen (1986), The Azores-Gibraltar plate boundary: focal mechanisms, depths of earthquakes, and their tectonic implications, *JGR*, *91*, 2029–2047.

Gutscher, M. (2012), Subduction beneath Gibraltar? recent studies provide answers., *EOS*, *93*, 133–134.

Haimon, B. (1978), Effect of cyclic loading on rock, *ASTM STP 654*, pp. 228–243.

Hatzfeld, D. (1978), Etude sismotectonique de la zone de collision Ibero-Maghrebine, *Ph.D. Thesis*.

Hernández, J., and H. Bellon (1985), Chronologie K-Ar du volcanisme Miocène du Rif oreintal (Maroc): Implications tectoniques et magmatologiques, *Revues de Géologie dynamique et de Géographie Physique*, *26*, 85–94.

Hernández, J., F. de Larouzière, J. Bolze, and P. Bordet (1987), Le magmatisme Néogène Bético-Rifian et le couloir de décrochement trans-Alborán, *Le Bulletin de la Société géologique de France*, *3*, 257–267.

Hickman, S., and B. Evans (1992), Growth of grain contacts in halite by solution-transfer: implications for diagenesis, lithification and strength recovery, *Fault Mechanics and Transport Properties of Rocks, International Geophysics*, *51*, 253–280.

Hiramatsu, Y., H. Honma, A. Saiga, M. Furumoto, and T. Ooida (2005), Seismological evidence on characteristic time of crack healing in the shallow crust, *GRL*, *32*(L09304), 4, doi:10.1029/2005GL022657.

Hodgson, J., and J. Cock (1956), Direction of faulting in the deep focus Spanish earthquake of March 29, 1954, *Tellus*, *8*, 321–328.

Hole, J., R. Catchings, K. St. Clair, M. Rymer, D. Okaya, and B. Carney (2001), Steep-dip seismic imaging of the shallow San Andreas fault near Parkfield, *Science*, *294*(5546), 1513–1515, doi:10.1126/science.1065100.

Hudson, J. (1981), Wave speeds and attenuation of elastic waves in material containing cracks, *Geophysical Journal of the Royal Astronomical Society*, *64*, 133–150.

Huibregtse, P., H. Alebeek, M. Zaal, and C. Biermann (1998), Paleostress analysis of the northern Nijar and southern Vera basins: constraints for the Neogene displacement history of major strike-slip faults in the Betic Cordilleras, SE Spain, *Tectonophysics*, *300*, 79–101.

I.G.M.E. (1975), El hidrogeologia del Campo de Nijar, *Instituto Geológico y Minero de España*.

IGN (2001), Catálogo sísmico nacional hasta el 2001, *Instituto Geografico Nacional*.

Ikuta, R., and K. Yamaoka (2004), Temporal variation in the shear wave anisotropy detected using the accurately controlled rountinely operated signal system (ACROSS), *JGR*, *109*, B09,305.

Jabaloy, A., J. Galindo-Zaldívar, and F. González-Lodeiro (1993), The Alpujárride-Nevado-Filábride extensional shear zone, Betic Cordillera, SE Spain, *Journ. Structural Geology*, *15*, 555–569.

Jennings, C. (1992), Preliminary fault activity map of California, *California Division of mines and Geology, Open-file report*, *92*(03).

Johanson, I., E. A., Fielding, F. Rolandone, and R. Burgmann. (2006), Coseismic and postseismic slip of the 2004 Parkfield earthquake from space-geodetic data, *BSSA*, *96*(4B), S269–S282, doi:10.1785/0120050818.

Johnson, K., R. Burgmann, and K. Larson (2006), Frictional properties on the San Andreas fault near Parkfield, California, inferred from models of afterslip following the 2004 earthquake, *BSSA*, *96*(4B), S321–S338, doi:10.1785/0120050808.

Johnston, D., M. Toksöz, and A. Timur (1979), Attenuation of seismic waves in dry and saturated rocks: II. mechanisms, *Geophyics*, *44*(4), 691–711.

Jonk, R., and C. Biermann (2002), Deformation in Neogene sediments of the Sorbas and Vera basins (SE Spain): constraints on simple-shear deformation and rigid body rotation along major strike-slip faults, *Journ. Struct. Geol*, *24*(963–977).

Jonsson, S., P. Segall, R. Pedersen, and G. Bjornsson (2003), Post-earthquake ground movements correlated to pore-pressure transients, *Nature*, *424*, 179–183, doi: 10.1038/nature01776.

Karageorgi, E., R. Clymer, and T. McEvilly (1992), Seismological studies at Parkfield ii: Search for temporal variations in wave propagation using Vibroseis, *BSSA*, *82*(3), 1388–1415.

Karageorgi, E., T. McEvilly, and R. Clymer (1997), Seismological studies at Parkfield iv: Variations in controlled source waveform parameters and their correlation with seismicity, 1987 to 1995, *BSSA*, *87*(1), 39–49.

Keller, J., S. Hall, C. Dart, and K. McClay (1995), The geometry and evolution of a transpressional strike-slip system: the Carboneras fault, SE Spain, *Journ. Geol. Soc. London*, *152*, 339–351.

Kelly, C., A. Rietbrock, D. Faulkner, and R. Nadeau (2013), Temporal changes in attenuation associated with the 2004 M6.0 Parkfield earthquake, *JGR*, *118*, 1–16.

Kern, H. (1978), The effect of high temperature and high confining pressure on compressional wave velocities in quartz-bearing and quartz-free igneous and metamorphic rocks, *Tectonophysics*, *44*, 185–203.

Kern, H. (1990), Laboratory seismic measurements: an aid in the interpretation of seismic field data, *Terra Nova*, *2*, 617–628.

Kern, H., B. Liu, and T. Popp (1997), Relationship between anisotropy of P and S wave velocities and anisotropy of attenuation in serpentinite and amphibolite, *JGR*, *102*, 3051–3065.

Khalatbari, A., D. Vo-Thanh, and J. Poirier (1991), Effect of fluid viscosity and saturation on the ultrasonic velocities in a fontainebleau sandstone, *GRL*, *18*(5), 885–888.

King, G., R. Stein, and J. Lin (1994), Static stress changes and the triggering of earthquakes, *BSSA*, *84*, 935–953.

Kiratzi, A., and C. Papazachos (1995), Active crustal deformation from the Azores triple junction to the Middle East, *Tectonophysics*, *243*, 1–24.

Kitamura, K., M. Masuda, M. Takahashi, and O. Nishizawa (2006), The influence of pore fluids on seismic wave velocities under high temperature and high pressure conditions: Development of a new technique with gas apparatus at AIST, Japan, *Earth Planets Space*, *58*, 1515–1518.

Kitamura, K., M. Takahashi, K. Mizoguchi, M. K., H. Ito, and S. Song (2010), Effects of pressure on pore characteristics and permeability of porous rocks as estimated from seismic wave velocities in cores from TCDP hole-A, *GJI*, *182*, 1148–1160.

Knopoff, and MacDonald (1958), Attenuation of small amplitude stress waves in solids, *Rev. Mod. Phys.*, *30*, 1178–1192.

Kozur, H., W. Kampschuur, C. Mulder-Blanken, and O. Simon (1974), Contribution to the Triassic ostracode faunas of the Betic zone (southern Spain), *Scripta Geol.*, *23*, 1–56.

Le Blanc, D., and P. Olivier (1984), Role of strike-slip faults in the Betic-Rifian orogeny, *Tectonophysics*, *101*, 345–355.

Lees, J., and G. Lindley (1994), Three-dimensional attenuation tomography at Loma Prieta: Inversion of t* for Q, *JGR*, *99*(B4), 6843–6863, doi:10.1029/93JB03460.

Lees, J., and P. Malin (1990), Tomographic images of P-wave velocity variation at Parkfield, California, *JGR*, *95*, 21,793–21,804.

Lewis, M., and P. Gerstoft (2012), Shear wave anisotropy from cross-correlation of seismic noise in the Parkfield pilot hole, *GJI*, *188*, 626–630.

Li, Y., and P. Leary (1990), Fault zone trapped seismic waves, *BSSA*, *80*(5), 1245–1271.

Li, Y., and J. Vidale (1996), Low-velocity fault-zone guided waves: Numerical investigations of trapping efficiency, *BSSA*, *86*(2), 371–378.

Li, Y., P. Leary, K. Aki, and P. Malin (1990), Seismic trapped modes in the Oroville and San Andreas fault zones, *Science*, *249*, 763–766.

Li, Y., K. Aki, D. Adams, and A. Hasemi (1994), Seismic guided waves trapped in the fault zone of the Landers California, earthquake of 1992, *JGR*, *99*(B6), 11,705–11,722.

Li, Y., K. Aki, and F. Vernon (1997a), San Jacinto fault zone guided waves: A discrimination for recently active fault strands near Anza, California, *JGR*, *102*(B6), 11,689–11,701.

Li, Y., K. Aki, J. Vidale, and M. Alvarez (1998a), A delineation of the Nojima fault ruptured in the M7.2 Kobe, Japan earthquake of 1995 using fault-zone trapped waves, *JGR*, *103*, 7247–7263.

Li, Y., J. Vidale, and E. Cochran (2004), Low-velocity damaged structure of the San Andreas Fault at Parkfield from fault zone trapped waves, *GRL*, *31*(L12S06).

Li, Y.-G., and J. Vidale (2001), Healing of the shallow fault zone from 1994-1998 after the 1992 M7.5 Landers, California, earthquake, *GRL*, *28*(15), 2999–3002, doi: 10.1029/2001GLO12922.

Li, Y.-G., W. Ellsworth, C. Thurber, P. Malin, and K. Aki (1997b), Fault-zone guided waves from explosions in the San Andreas fault at Parkfield and Cienega Valley, California, *BSSA*, *87*, 210–221.

Li, Y.-G., J. Vidale, K. Aki, F. Xu, and T. Burdette (1998b), Evidence of shallow fault zone strengthening after the 1992 M7.5 Landers, California, earthquake, *Science*, *279*(5348), 217–219, doi:10.1126/science.279.5348.217.

Li, Y.-G., J. Vidale, S. Day, O. D.D., and E. Cochran (2003), Postseismic fault healing on the rupture zone of the 1999 M7.1 Hector Mine, California, earthquake, *BSSA*, *93*(2), 854–869, doi:10.1785/0120020131.

Li, Y.-G., P. Chen, E. Cochran, J. Vidale, and T. Burdette (2006), Seismic evidence for rock damage and healing on the San Andreas fault associated with the 2004 M6.0 Parkfield earthquake, *BSSA*, *96*(4B), S349–S363, doi:10.1785/0120050803.

Li, Y.-G., P. Chen, E. Cochran, and J. Vidale (2007), Seismic velocity variations on the San Andreas fault caused by the 2004 M6 Parkfield earthquake and their implications, *Earth Planets Space*, *59*, 21–31.

Lin, F.-C., M. Moschetti, and M. Ritzwoller (2008), Surface wave tomography of the western United States from ambient seismic noise: Rayleigh and Love wave phase velocity maps, *GJI*, *173*(1), 281–298, doi:10.1111/j1365-246X.2008.03720.x.

Liu, Y., S. Crampin, and I. Main (1997), Shear-wave anisotropy: Spatial and temporal variations in time delays at Parkfield, central California, *GJI*, *130*, 771–785.

Liu, Y., T. Teng, and Y. Ben-Zion (2004), Systematic analysis of shear wave splitting in the aftershock zone of the 1999 Chi-Chi, Taiwan, earthquake: shallow crustal anisotropy and lack of precursory variations, *BSSA*, *94*, 2330–2347.

Liu, Y., T. Teng, and Y. Ben-Zion (2005), Near-surface seismic anisotropy, attenuation and dispersion in the aftershock region of the 1999 Chi-Chi earthquake, *GJI*, *160*, 695–706.

Lobkis, I., and R. Weaver (2001), On the emergence of the Green's function in the correlations of a diffuse field, *J. Acoust. Soc. Am.*, *110*, 3011–3017.

Lonergan, L., and M. Mange-Rajetsky (1994), Evidence for internal zone unroofing from foreland basin sediments, Betic Cordillera, SE Spain, *J. Geol. Soc. London*, *151*, 515–529.

Lonergan, L., and J. Platt (1995), The Malaguide-Alpujarride boundary: a major extensional contact in the Internal Zone of the eastern Betic Cordillera, southeastern Spain, *Journal of Structural Geology*, *17*, 1655–1671.

Lopez, C., C. Casado, S. Sanz de Galdeano, J. Molina Palacioc, and H. Romero (2001), The structure of the Alboran Sea: an interpretation from seismological and geological data, *Tectonophysics*, *338*, 79–95.

Mackie, R., D. Livelybrooks, T. Madden, and J. Larsen (1997), A magnetotelluric investigation of the San Andreas Fault at Carrizo Plain California, *GRL*, *24*, 1847–1850.

Makel, G., and H. Rondeel (1979), Differences in stratigraphy and metamorphism between superposed Malaguide and Alpujarride units in the Espuña area (Betic Cordilleras, SE Spain, *Estud. Geol.*, *35*, 109–117.

Marin-Lechado, C., J. Galindo-Zaldívar, L. Rodríguez-Fernandez, I. Serrano, and A. Pedrera (2005), Active faults, seismicity and stresses in an internal boundary of a tectonic arc (Campo de Dalías and Níjar, southeastern Betic Cordilleras, Spain, *Tectonophysics*, *396*, 81–96.

Marone, C. (1998), The effect of loading rate on static friction and the rate of fault healing during the earthquake cycle, *Nature*, *391*, 69–72.

Martin-Lechado, C., J. Galindo-Zaldivar, L. Rodriguez-Fernandez, and A. Pedrera (2006), Mountain front development by folding and crustal thickening in the Internal zone of the Betic Cordillera - Alboran Sea boundary, *Pure Appl. Geophys.*, *164*, 1–21.

Martinez-Diaz, J. (2002), Stress field variation related to fault interaction in a reverse oblique-slip fault: the Alhama de Murcia fault, Betic Cordillera, Spain, *Tectonophysics*, *356*, 291–305.

Martínez-Martínez, J., and J. Azañon (1997), Mode of extensional tectonics in the Southeastern Betics, (SE Spain): implications for the tectonic evolution of the Peri-Albóran orogenic system, *Tectonics*, *16*, 205–225.

Martínez-Martínez, J., J. Soto, and J. Balanyá (1995), Large-scale structures in the Nevado-Filabride complex and crustal seismic fabrics of the deep seismic reflection profile ESCI-Béticas2, *Revista de la Sociedad Geológica de España*, *8*, 477–489.

Martinez Solares, J., and J. Mezcua (2002), Catálogo sísmico de la Península Ibérica (880 a.c.-1900), *Monigrafía 18*, p. 253.

Masana, E., J. Martínez-Díaz, J. Hernández-Enrile, and P. Santanach (2004), The Alhama de Murcia fault (SE Spain), a seismogenic fault in a diffuse plate boundary: seismotectonic implications for the Ibero-Magrebian region, *JGR*, *109*, 1–17.

Massonnet, D., W. Thatcher, and H. Vadon (1996), Detection of postseismic fault-zone collapse following the Landers earthquake, *Nature*, *382*, 612–616.

Mauffret, A., A. Maldonado, and A. Campillo (1992), Tectonic framework of the eastern Alboran and Western Algerian basins, western Mediterranean, *Geo Mar. Lett.*, *12*, 104–110.

Mavko, G. (1979), Frictional attenuation: an inherent amplitude dependence, *JGR*, *84*, 4769–4775.

Mavko, G., and A. Nur (1975), Melt squirt in the asthenosphere, *JGR*, *80*, 1444–1448.

Mavko, G., and A. Nur (1979), Wave attenuation in partially saturated rocks, *Geophysics*, *44*, 161–178.

McClusky, S., R. Reilinger, S. Mahmoud, D. Ben Sari, and A. Tealeb (2003), GPS constraints on Africa (Nubia) and Arabia plate motions, *GJI*, *155*, 126–138.

Meijninger, B. (2006), Late orogenic extension and strike-slip deformation in the Neogene of Southeastern Spain, *Ph.D. Thesis, Utrecht University, Utrecht*.

Meijninger, B., and R. Vissers (2006), Miocene extensional basin development in the Betic Cordillera, SE Spain revealed through analysis of the Alhama de Murcia and Crevillente faults, *Basin Research*, *18*(547–571).

Michael, A., and D. Eberhart-Philips (1991), Relations among fault behaviour, subsurface geology and three dimensional velocity models, *Science*, *253*, 651–654.

Michelini, A., and T. McEvilly (1991), Seismological studies at Parkfield: I. Simultaneous inversion for velocity structure and hypocentres using B-splines parameterization, *BSSA*, *81*, 524–552.

Miller, M. (1996), Ductility in fault gouge from a normal fault system, Death Valley California: a mechanism for fault zone strengthening and relevance for palaeoseismicity, *Geology*, *24*, 603–606.

Minato, S., T. Takeshi, O. Shiro, and T. Matsuoka (2012), Monitoring seismic velocity change caused by the 2011 Tohoku-oki earthquake using ambient noise records, *GRL*, *39*(L09309), doi:10.1029/2012GL051405.

Mitchell, T., and D. Faulkner (2009), The nature and origin of off-fault damage surrounding strike-slip fault zones with a wide range of displacements: A field study from the Atacama fault system, northern Chile, *JSG*, *31*, 802–816, doi: 10.1016/j.jsg.2009.05.002.

Montenat, C., P. Ott d'Estevou, and P. Masse (1987), Tectonic-sedimentary characters of the Betic Neogene basins evolving in a crustal transcurrent shear zone (SE Spain), *Bulletin des Centre de Recherches Exploration-Production Elf-Aquitaine*, *11*, 1–22.

Montenat, C., J. Rodríguez-Fernández, P. Ott d'Estevou, and C. Sanz de Galdeano (1990), Geodynamic evolution of the Betic Neogene intramontane basins (S and SE Spain), *Iberian Neogene Basins*, *2*, 6–59.

Moos, D., and M. Zoback (1983), In situ studies of velocity in fractured crystalline rocks, *JGR*, *88*, 2345–2358.

Morales Ruano, S., F. Carrillo Rosúa, P. Hach-ali, F. de la Fuente Chacon, and E. Contreras Lopez (2000), Epithermal Cu-Au mineralization in the Palai-Islica deposit, Almeria, southeastern Spain: fluid-inclusion evidence for mixing of fluids as a guide to gold mineralization, *The Canadian Mineralogist*, *38*, 553–565.

Morgan, J. (2004), Particle dynamics simulations of rate- and state-dependent frictional sliding of granular gouge, *Pure Appl. Geophys.*, *161*, 1877–1891.

Munson, C., C. Thurber, Y. Li, and P. Okubo (1995), Crustal shear wave anisotropy in southern Hawaii: spatial and temporal analysis, *JGR*, *100*(B10), 20,367–20,377.

Murphy, W. (1982), Effects of microstructure and pore fluids on the acoustic properties of granular sedimentary materials, *Ph.D. thesis, Stanford University*.

Nadeau, R., and D. Dolenc (2005), Nonvolcanic tremors deep beneath the San Andreas fault, *Science*, *307*(5708), 389, doi:10.1126/science.1107142.

Nadeau, R., and A. Guilhem (2009), Nonvolcanic tremor evolution and the San Simeon and Parkfield, California, earthquakes, *Science*, *325*, 191–193, doi: 10.1126/science.1174155.

Nadeau, R., and L. Johnson (1998), Seismological studies at Parkfield VI: Moment release rates and estimates of source parameters for small repeating earthquakes, *BSSA*, *88*(3), 790–814.

Nadeau, R., M. Antolik, P. Johnson, W. Foxall, and T. McEvilly (1994), Seismological studies at Parkfield III: Microearthquake clusters in the study of fault-zone dynamics, *BSSA*, *84*(2), 247–263.

Nadeau, R., W. Foxall, and T. McEvilly (1995), Clustering and periodic recurrence of microearthquakes on the San Andreas fault at Parkfield, California, *BSSA*, *267*(5197), 503–507, doi:10.1126/science.267.5197.503.

Nakahara, H. (2006), A systematic study of theoretical relations between spatial correlation and Green's functions in one-, two-, and three-dimensional random scalar wavefields, *GJI*, *167*, 1097–1105.

Nicolson, H., A. Curtis, B. Baptie, and E. Galetti (2012), Seismic interferometry and ambient noise tomography in the British Isles, *Proceedings of the Geologists' Association*, *123*(1), 74–86.

Nur, A. (1971), Viscous phase in rocks and the low-velocity zone, *JGR*, *76*(5), 1270–1277.

Nur, A. (1972), Dilatancy, pore fluids and premonitory variations of t_s/t_p travel times, *BSSA*, *62*(5), 1217–1222.

Nur, A. (1974), Matsushiro, Japan, earthquake swarm: Confirmation of the dilatancy-fluid diffusion model, *Geology*, *2*, 217–221.

Nur, A., and J. Booker (1972), Aftershocks caused by pore fluid flow?, *Science*, *175*(4024), 885–887, doi:10.1126/science.175.4024.885.

Nur, A., and G. Simmons (1969), The effect of saturation on velocity in low porosity rocks, *EPSL*, *7*, 183–193.

O'Connell, R., and B. Budiansky (1974), Seismic velocities in dry and saturated cracked solids, *JGR*, *79*(35), 5412–5426.

O'Connell, R., and B. Budiansky (1977), Viscoelastic properties of fluid-saturated cracked solids, *JGR*, *82*, 5719–5736.

O'Doherty, and Anstay (1971), Reflections on amplitudes, *Geophys. Prosp.*, *19*, 430–458.

Olsen, M., C. Scholz, and A. Leger (1998), Healing and sealing of a simulated fault gouge under hydrothermal conditions for fault healing, *JGR*, *103*, 7421–7430.

Oshima, H., T. Tokunaga, K. Miyajima, K. Tanaka, and H. Ishibashi (1996), Ground-water fluctuations caused by the earthquake, *Journal of the Japan Society of Engineering Geology*, *37*, 351–358.

Ott d'Estevou, P., and C. Montenat (1985), Evolution structurale de la zone Betique Orientale (Espagne) du Tortonian à l'Holocène, *C.R. Acad. Sci. Paris 300 II*, *8*, 363–368.

Ott d'Estevou, P., C. Montenat, and J. Alvado (1990), Le Bassins Néogènes du Domaine Bétique Oriental (Espagne), *Documents et Travaux du Institut Géologique Albert-de-Lapparent 12-13, Paris*, pp. 165–187.

Ozacar, A., and G. Zandt (2009), Crustal structure and seismic anisotropy near the San Andreas Fault at Parkfield, California, *GJI*, *178*, 1098–1104.

Park, J. (1987), Multitaper spectral analysis of high-frequency seismograms, *JGR*, *92*(B12), 12,675–12,684.

Peacock, S., S. Crampin, D. Booth, and J. Fletcher (1988), Shear wave splitting in the Anza seismic gap, Southern California: Temporal variations as possible precursors, *JGR*, *93*(B4), 3339–3356.

Pedrera, A., C. Marin-Lechado, J. Galindo-Zaldivar, L. Rodriguez-Fernandez, and A. Ruiz-Constan (2006), Fault and fold interaction during the development of the Neogene-Quaternary Almeria-Nijar basin (SE Betic Cordilleras), *Geological Society Special Publications, Tectonics of the Western Mediterranean and North Africa*(262), 217–230.

Pedrera, A., J. Galindo-Zaldivar, C. Sanz de Galdeano, and A. Lopez-Garrido (2007), Fold and fault interactions during the development of an elongated narrow basin: the Almanzora Neogene-Quaternary corridor (SE Betic Cordillera, Spain), *Tectonics*, *26*(TC6002).

Pedrera, A., F. Mancilla, A. Ruiz-Constan, J. Galindo-Zaldivar, J. Morales, J. Arzate, C. Marin-Lechado, P. Ruano, L. Buotempo, F. Anahnah, and D. Stich (2010), Crustal-scale transcurrent fault development in a weak-layered crust from an integrated geophysical research: Carboneras Fault zone, eastern Betic Cordillera, Spain, *Geochem., Geophys. Geosyst.*, *11*(Q12005).

Peltzer, G., P. Rosen, and F. Rogez (1998), Poroelastic rebound along the Landers 1992 earthquake surface rupture, *JGR*, *103*(B12), 30,131–30,145, doi:10.1029/98JB02302.

Peng, Z., and Y. Ben-Zion (2004), Systematic analysis of crustal anisotropy along the Karadere-Duzce branch of the North Anatolian Fault, *GJI*, *159*, 253–274.

Peng, Z., Y. Ben-Zion, A. Michael, and L. Zhu (2003), Quantitative analysis of seismic fault zone waves in the rupture zone of the 1992 Landers, California, earthquake: evidence for a shallow trapping structure, *GJI*, *155*, 1021–1041.

Peselnick, L., and I. Zietz (1959), Internal friction of fine grained limestones at ultrasonic frequencies, *Geophysics*, *24*, 285–296.

Platt, J., and R. Vissers (1989), Extensional collapse of thickened continental lithosphere: A working hypothesis for the Alboran Sea and the Gibraltar Arc, *Geology*, *17*(540–543).

Platt, J., and M. Whitehouse (1999), Early Miocene high-temperature metamorphism and rapid exhumation in the Betic Cordillera (Spain): evidence from U-Pb zircon ages, *EPSL*, *171*(591–605).

Platt, J., B. Van der Eeckhout, E. Janzen, G. Konert, O. Simon, and R. Weijermars (1983), The structure and tectonic evolution of the Aguilon fold-nappe, Sierra Alhamilla, Betic Cordilleras, SE Spain, *J. Struct. Geol.*, *5*, 519–538.

Platzman, E., J. Platt, and P. Olivier (1993), Palaeomagnetic rotations and fault kinematics in the Rif Arc of Morocco, *J. Geol. Soc. London*, *8*, 707–718.

Pondrelli, A. (1999), Patterns of seismic deformation in the Western Mediterranean, *Annali de Geofisica*, *42*, 57–70.

Rice, J., C. Sammis, and R. Parsons (2005), Off-fault secondary failure induced by a dynamic slip pulse, *BSSA*, *95*(1), 109–134, doi:10.1785/0120030166.

Rietbrock, A. (2001), P wave attenuation structure in the fault area of the 1995 Kobe earthquake, *JGR*, *106*(B3), 4141–4154, doi:10.1029/2000JB900234.

Robin, P.-Y. (1973), Note on effective pressure, *JGR*, *78*, 2434–2437.

Rodríguez-Fernández, J., and C. Sanz de Galdeano (2006), Late orogenic intramontane basin development: The Granada basin, Betics, (Southern Spain), *Basin Research*, *18*(85–102).

Rodríguez-Fernández, J., J. Fernández, A. Lopez-Garrido, and C. Sanz de Galdeano (1984), The central sector of the Betic Cordilleras, a realm situated between the Atlantic and Mediterranean domains during the Upper Miocene, *Ann. Geol. Pays. Hellen.*, *32*, 97–103.

Rodríguez-Fernández, J., A. Azor, and J. Azañon (2012), The Betic intramontane basins (SE Spain): stratigraphy, subsidence and tectonic history, *Tectonics of Sedimentary Basins: Recent Advances*.

Roecker, S., C. Thurber, and D. McPhee (2004), Joint inversion of gravity and arrival time data from Parkfield: new constraints on structure and hypocenter locations near the SAFOD drill site, *GRL*, *31*, 1–4.

Roeloffs, E. (1996), Poroelastic techniques in the study of earthquake-related hydrologic phenomena, *Advances in Geophysics*, pp. 135–195.

Rojstaczer, S., and S. Wolf (1992), Permeability changes associated with large earthquakes: An example from Loma Prieta, California, *Geology*, *20*, 211–214.

Rojstaczer, S., S. Wolf, and R. Michel (1995), Permeability enhancement in the shallow crust as a cause of earthquake-induced hydrological changes, *Nature*, *373*, 237–239, doi:10.1038/373237a0.

Roux, P., K. Sabra, W. Kuperman, and A. Roux (2005), Ambient noise cross correlations in free space: theoretical approach, *J. Acoust. Soc. Am.*, *117*, 79–84.

Rubinstein, J., and G. Beroza (2004), Evidence for widespread nonlinear strong ground motion in the Mw 6.9 Loma Prieta earthquake, *BSSA*, *94*(5), 1595–1608.

Rubinstein, J., and G. Beroza (2005), Depth constraints on nonlinear strong ground motion from the 2004 Parkfield earthquake, *GRL*, *32*(L14313,5), doi: 10.1029/2005GLO23189.

Rutter, E., R. Maddock, S. Hall, and S. White (1986), Comparative microstructures of natural and experimentally produced clay-bearing fault gouges, *Pure and Appl. Geophys.*, *124*, 3–30.

Rutter, E., D. Faulkner, and R. Burgess (2012), Structure and geological history of the Carboneras Fault Zone, SE Spain: Part of a stretching transform fault system, *Jour. Structural Geology*, *45*, 68–86.

Rymer, M., J. Tinsley III, J. Treiman, J. Arrowsmith, K. Clahan, A. Rosinski, W. Bryant, H. Snyder, G. Fuis, N. Toke, and G. Bawden (2006), Surface fault slip associated with the 2004 Parkfield, California, earthquake, *BSSA*, *96*(4B), S11–S27.

Sabra, K., P. Gerstoft, W. Roux, P. amd Kuperman, and M. Fehler (2005a), Extracting time-domain Green's function estimates from ambient seismic noise, *GRL*, *32*(3), doi: 1–5.

Sabra, K., P. Gerstoft, P. Roux, W. Kuperman, and M. Fehler (2005b), Surface wave tomography from microseismc in Southern California, *GRL*, *32*(L14311).

Saito, M. (1988), Disper80: a subroutine package for the calculation of seismic normal-mode solutions, *Seismological Algorithms: Computational Methods and Computer Programs*, pp. 293–319.

Sanz de Galdeano, C. (1989), Las fallas de desgarre del borde Sur de la cuenca de Sorbas Tabernas (norte de Sierra Alhamilla, Almería, Cordilleras Béticas, *Boletín Geológico y Minero*, *101*(73–85).

Sanz de Galdeano, C., and E. Buforn (2005), From strike-slip to reverse reactivation: the Crevillente fault system and seismicity in the Bulla-Mula area (Betic Cordillera, SE Spain, *Geologica Acta*, *3*, 241–250.

Sanz de Galdeano, C., and J. Vera (1992), Stratigraphic record and palaeogeographical context of the Neogene basins in the Betic Cordillera, Spain, *Basin Research*, *4*, 21–36.

Sato, H., and M. Fehler (1998), Seismic wave propagation in the heterogeneous earth, *Springer-Verlag, Berlin and New York*.

Sato, T., R. Sakai, K. Furaya, and T. Kodama (2000), Coseismic spring flow changes associated with the 1995 Kobe earthquake, *GRL*, *27*(8), 1219–1222.

Savage, J. (1969), Comment on "Velocity and Attenuation of seismic waves in imperfectly elastic rock by R.B. Gordon and L.A. Davis, *JGR*, *74*, 726–728.

Savage, J., and J. Svarc (1997), Postseismic deformation associated with the 1992 $M_w = 7.3$ Landers earthquake, southern California, *JGR*, *102*(B4), 7565–7577, doi: 10.1029/97JB00210.

Savage, M., X. Shih, R. Meyer, and R. Aster (1989), Shear wave anisotropy of active tectonic regions via automated S-wave polarization analysis, *Tectonophysics*, *165*, 279–292.

Savage, M., W. Peppin, and U. Vetter (1990), Shear wave anisotropy and stress direction in and near Long Valley caldera, California, *JGR*, *95*, 11,165–11,117.

147

Schaff, D., and G. Beroza (2004), Coseismic and postseismic velocity changes measured by repeating earthquakes, *JGR*, *109*(B10302), doi:10.1029/2004JB003011.

Scotney, P., R. Burgess, and E. Rutter (2000), Ar-Ar dating of the Cabo de Gata volcanic series and displacements on the Carboneras fault, S.E. Spain, *Journ. of the Geological Society*, *157*, 1003–1008.

Serrano, F. (1990a), Presencia de Serravalliense marino en la Cuenca de Níjar (Cordillera Bética, España), *Geoaceta*, *7*, 95–97.

Serrano, F. (1990b), El Mioceno Medio en el área de Níjar (Almería, España), *Revista de la Sociedad Geológica de España*, *3*, 65–77.

Serrano, F., and J. Gonzales Donoso (1989), Cronoestratigrafia de la sucesion volcano-sedimentaria del area de Carboneras (Sierra de Gata, Almeria), *Reviews Geological Society Espana*, *2*(143–151).

Serrano, I., T. Hearn, J. Morales, and F. Torcal (2005), Seismic anisotropy and velocity structure beneath the southern half of the Iberian Peninsula, *Phys. Earth Planet. Inter.*, *150*(4), 317–330.

Shapiro, N., and M. Campillo (2004), Emergence of broadband Rayleigh waves from correlations of the ambient seismic noise, *GRL*, *31*(7).

Shapiro, N., M. Campillo, L. Stehly, and M. Ritzwoller (2005), High-resolution surface wave tomography from ambient seismic noise, *Science*, *307*(1615).

Skempton, A. (1961), Effective stress in soils, concrete and rocks, *Pore Pressure and Suction in Soils*, p. 1.

Sleep, N. (2009), Depth of rock damage from strong seismic ground motions near the 2004 Parkfield mainshock, *BSSA*, *99*(5), 3067–3076, doi:10.1785/0120090065.

Sleep, N., E. Richardson, and C. Marone (2000), Physics of friction and strain rate localization in synthetic fault gouge, *JGR*, *105*, 25,875–25,890.

Snieder, R. (2004), Extracting the Green's function from the correlation of coda waves: a derivation based on stationary phase, *Phys. Rev. E*, *69*(046610).

Soediono, H. (1971), Geological investigations in the Chirivel area, provence of Almeria, SE Spain, *Thesis*, p. 143.

Spencer, J. (1979), Bulk and shear attenuation in Berea sandstone: The effects of pore fluids, *JGR*, *84*, 7521–7523.

Stapel, G., R. Moeys, and C. Biermann (1996), Neogene evolution of the Sorbas basin (SE Spain) determined by paleostress analysis, *Tectonophysics*, *255*(291–305).

Stehly, L., M. Campillo, and N. Shapiro (2006), A study of the seismic noise from its long range correlation properties, *JGR*, *111*(B10306).

Stich, D., C. Ammon, and J. Morales (2003), Moment tensor solutions for small and moderate earthquakes in the Ibero-Maghreb region, *JGR*, *108*, 2148.

Stierman, D. (1984), Geophysical and geological evidence for fracturing, water circulation and chemical alteration in granitic rocks adjacent to major strike-slip faults, *JGR*, *89*, 5849–4857.

Stierman, D., and R. Kovach (1979), An in situ velocity study: The Stone Canyon well, *JGR*, *84*, 672–678.

Tadokoro, K., M. Ando, and Y. Umeda (1999), S-wave splitting in the aftershock region of the 1995 Hyogo-ken Nanbu earthquake, *JGR*, *104*, 981–991.

Taira, T., P. Silver, F. Niu, and R. Nadeau (2008), Detecting seismogenic stress evolution and constraining fault zone rheology in the San Andreas Fault following the 2004 Parkfield earthquake, *JGR*, *113*(B03303), doi:10.1029/2007JB005151.

Tarantola, A., and B. Valette (1982), Generalized nonlinear inverse problems solved using the least squares criterion, *Rev. geophys. Space Phys.*, *20*(2), 219–232.

Thomsen, L. (1995), Elastic anisotropy due to aligned cracks in porous rock, *Geophys. Prospect.*, *43*, 805–829.

Thurber, C., S. Roecker, W. Ellsworth, Y. Chen, W. Lutter, and R. Sessions (1997), Two-dimensional seismic image of the San Andreas fault in the Northern Gabilan Range, central California: evidence for fluids in the fault zone, *GRL*, *24*, 1591–1594.

Thurber, C., S. Roecker, K. Roberts, M. Gold, L. Powell, and K. Rittger (2003), Earthquake location and three-dimensional fault zone structure along the creeping section of the San Andreas fault near Parkfield, California: preparingg for SAFOD, *GRL*, *30*, 1112–1115.

Thurber, C., H. Zhang, F. Waldhauser, J. Hardebeck, A. Michael, and D. Eberhart-Philips (2006), Three-dimensional compressional wavespeed model, earthquake relocations, and focal mechanisms for the Parkfield, California, region, *BSSA*, *96*(4B), S38–S49, doi:10.1785/0120050825.

Toksöz, M., D. Johnston, and A. Timur (1979), Attenuation of seismic waves in dry and saturated rocks: 1. Laboratory measurements, *Geophysics*, *44*(4), 681–690, doi: 10.1190/1.1440969.

Tokunaga, T. (1999), Modeling of earthquake-induced hydrological changes and possible permeability enhancement due to the 17 January 1995 Kobe earthquake, Japan, *Journal of Hydrology*, *23*, 221–229.

Torne, M., and E. Banda (1992), Crustal thinning from the Betic Cordillera to the Alboran Sea, *Geo. Mar. Lett.*, *12*, 76–81.

Torres-Roldán, R. (1979), The tectonic subdivision of the Betic Zone (Betic Cordilleras, Southern Spain): its significance and one possible geotectonic scenario for the westernmost Alpine belt, *Am. J. Sci.*, *279*, 19–51.

Turner, R., R. Nadeau, and R. Burgmann (2011), Aseismic slip, repeating earthquakes and fault interaction in the Loma Prieta aftershock zone, *AGU Fall Meeting Abstracts*, pp. S23B–2269.

Udías, A., and A. López Arroyo (1972), Plate tectonics and the Azores-Gibraltar region, *Nature*, *237*, 67–79.

Udías, A., A. López Arroyo, and J. Mezcua (1976), Seismotectonics of the Azores-Alboran region, *Tectonophysics*, *31*, 259–289.

Unsworth, M., and P. Bedrosian (2004), Electrical resistivity structure at the SAFOD site from magnetotelluric exploration, *GRL*, *31*(L12S05), doi: 10.1029/2003GL019405.

Unsworth, M., G. Egbert, and J. Booker (1999), High-resolution electromagnetic imaging of the San Andreas Fault in Central California, *JGR*, *104*, 1131–1150.

Uwe, M., T. Krautworst, and C. Brachert (2003), Sedimentary facies during early stages of flooding in an extensional basin: the Brèche Rouge de Carboneras (Late Miocene, Almeria, S.E. Spain), *International Journal of Earth Sciences (Geol. Rundsch.)*, *92*(610–623).

van Meijninger, B., and R. Vissers (2006), Miocene extensional basin development in the Betic Cordilleras, SE Spain revealed through analysis of the Alhama de Murcia and Crevillente faults, *Basin Research*, *18*, 547–571.

Vermilye, J., and C. Scholz (1998), The process zone: A microstructural view of fault growth, *JGR*, *103*(B6), 12,223–12,237.

Vidale, J., and Y.-G. Li (2003), Damage to the shallow Landers fault from the nearby Hector Mine earthquake, *Nature*, *421*, 524–526.

Vidale, J., W. Ellsworth, A. Cole, and C. Marone (1994), Rupture variation with recurrence interval in eighteen cycles of a small earthquake, *Nature*, *368*, 624–626.

Vissers, R. (1981), A structural study of the central Sierra de los Filabres (Betic zone, SE Spain) with emphasis on deformational processes and their relation to the Alpine metamorphism, *Ph.D. thesis*, p. 154.

Vissers, R. (2012), Extension in a convergent tectonic setting: a lithospheric view on the Alboran system of SW Europe, *Geologica Belgica*, *15*, 53–72.

Völk, H. (1967), Zur geologie und stratigraphe des neogenbeckens von Vera, Södust-Spanien, *PhD thesis, Universiteit van Amsterdam*.

Waller, R. (1966), Effects of the March 1964 Alaska earthquake on the hydrology of south-central Alaska, *U.S. Geological Survey Professional Paper*, *544-B*, 28.

Walsh, J. (1966), Seismic wave attenuation in rock due to friction, *JGR*, *71*, 2591–2599.

Walsh, J. (1969), New analysis of attenuation in partially melted rock, *JGR*, *74*, 4333–4337.

Wang, C., W. Lin, and F. Wu (1978), The constitution of the San Andreas fault zone at depth, *GRL*, *5*(9), 741–744.

Wang, C., F. Rui, Y. Zhengsheng, and S. Xingjue (1986), Gravity anomaly and density structure of the San Andreas fault zone, *Pure Appl. Geophys.*, *124*, 127–140.

Wapenaar, K. (2004), Retrieving the elastodynamic Green's function of an arbitrary homogeneous medium by cross correlation, *Physical Review E.*, *69*(046610).

Watts, A., J. Platt, and P. Buhl (1993), Tectonic evolution of the Alboran Sea basin, *Basin Research*, *5*, 153–177.

Weaver, R., and O. Lobkis (2001), Ultrasonics without a source: Thermal fluctuation correlations at MHz frequencies, *Physical Review Letters*, *87*, 134,301–1–134,301–4.

Weijermars, R., T. Roep, B. Van den Eeckhout, G. Postma, and K. Kleverlaan (1985), Uplift history of a Betic fold nappe inferred from Neogene-Quaternary sedimentation and tectonics (in the Sierra Alhamilla and Almeria, Sorbas and Tabernas Basins of the Betic Cordilleras, SE Spain), *Geologie en Mijnbouw*, *64*, 397–411.

Westra, G. (1969), Petrogenesis of a composite metamorphic facies series in an intricate fault zone in the southeastern Sierra Cabrera, S.E. Spain, *PhD thesis, Universiteit van Amsterdam*.

White, J. (1975), Computed seismic speeds and attenuation in rocks with partial gas saturation, *Geophysics*, *40*, 224–232.

Whitehead, R. (1985), Hydrologic changes following the Idaho Borah Peak earthquake, *Workshop XXVIII on the Borah Peak, Idaho earthquake*, pp. 556–572.

Wibberley, C., and T. Shimamoto (2003), Internal structure and permeability of major strike-slip fault zones: the Median Tectonic Line in Mie Prefecture, Southwest Japan, *JSG*, *25*(1), 59–78, doi:10.1016/S0191-8141(02)00014-7.

Wildi, W. (1983), La Chaîne Tello-Rifaine (Algérie, Maroc, Tunisie): structure, stratigraphie et évolution du Trias au Miocene, *Rev. Geol. Dyn. Geogr. Phys.*, *24*.

Wilson, J., J. Chester, and F. Chester (2003), Microfracture analysis of fault growth and wear processes, Punchbowl Fault, San Andreas system, California, *JSG*, *25*(11), 1855–1873, doi:10.1016/S0191-8141(03)00036-1.

Winkler, K., and A. Nur (1979), Pore fluids and seismic attenuation in rocks, *GRL*, *6*(1), 1–4, doi:10.1029/GL006i001p00001.

Winkler, K., and A. Nur (1982), Seismic attenuation: Effects of pore fluids and frictional sliding, *Geophysics*, *47*(1), 1–15, doi:10.1190/1.1441276.

Wyllie, M., A. Gregory, and G. Gardner (1956), Elastic wave velocities in heterogeneous and porous media, *Geophysics*, *27*, 41–70.

Wyss, M., C. Sammis, R. Nadeau, and S. Wiemer (2004), Fractal dimension and b-value on creeping and locked patches of the San Andreas Fault near Parkfield, California, *BSSA*, *94*(2), 410–421, doi:10.1785/0120030054.

Xu, S., and M. King (1990), Attenuation of elastic waves in a cracked solid, *GJI*, *101*, 169–180.

Yamakawa, N. (1962), Scattering and attenuation of elastic waves, *Geophysical Magazine (Tokyo)*, *31*, 63–103.

Yang, Y., and M. Ritzwoller (2008a), Characteristics of ambient seismic noise as a source for surface wave tomography, *Geochem. Geophys. Geosyst.*, *9*, doi:10.1029/2007GC001814.

Yang, Y., and M. Ritzwoller (2008b), Teleseismic surface wave tomography in the western US using the Transportable Array component of USArray, *GRL*, *35*(L04308).

Yao, H., R. Van Der Hilst, and M. de Hoop (2006), Surface-wave array tomography in SE Tibet from ambient seismic noise and two-station analysis - I. Phase velocity maps, *GJI*, *166*, 732–744.

Yao, H., C. Beghein, and R. Van Der Hilst (2008), Surface-wave array tomography in SE Tibet from ambient seismic noise and two-station analysis - II. Crustal and upper-mantle structure, *GJI*, *173*, 205–219.

Yao, H., X. Campan, M. de Hoop, and R. Van Der Hilst (2009), Estimation of surface-wave Green's function from correlations of direct waves, coda waves, and ambient noise in SE Tibet, *Phys. Earth Planet. Inter.*, doi:10.1016/j.pepi.2009.07.002.

Zeck, H. (1996), Betic-Rif orogeny: subduction of Mesozoic Tethys lithosphere under eastward drifting Iberia, slab detachment before 22 Ma, and subsequent uplift and extensional tectonics, *Tectonophysics*, *254*, 1–16.

Zeck, H., P. Monie, M. Villa, and B. Hansen (1992), Very high rates of cooling and uplift in the Alpine belt of the Betic Cordilleras, southern Spain, *Geology*, *20*, 78–82.

Zhang, and Ulrych (2002), Estimation of quality factors from CMP records, *Geophysics*, *67(5)*, 1542–1547.

Zhang, H., Y. Liu, C. Thurber, and S. Roecker (2007), Three-dimensional shear-wave splitting tomography in the Parkfield, California region, *GRL*, *34*(L24308).